Numerical Simulation of Fluid-Structure Interaction during the Expansion Phase in Sodium Cooled Fast Reactors

Zur Erlangung des akademischen Grades eines DOKTORS DER INGENIEURWISSENSCHAFTEN (Dr.-Ing.)

von der KIT-Fakultät für Maschinenbau des Karlsruher Instituts für Technologie (KIT) angenommene

DISSERTATION

von

M.Sc. Maximilian Hartig

Tag der mündlichen Prüfung: 04.11.2019

Hauptreferent: Prof. Dr.-Ing Thomas Schulenberg

Korreferent: Prof. Dr.-Ing Xu Cheng

Abstract

In case of a severe malfunction, Sodium cooled Fast Reactors (SFRs) can experience partial disintegration of the reactor core. The changed composition of fissile material after such a Hypothetical Core Disruptive Accident (HCDA), can lead to a prompt critical configuration. The resulting power excursion vaporizes part of the core and the arising steam pressure expels molten fuel from the core region into the coolant pool, provoking a vapor explosion. During this expansion phase, the coolant vapor bubble accelerates a sodium slug, which impacts the reactor lid and challenges the integrity of the vessel.

The development process of an SFR includes studies of such extremely unlikely events with dedicated severe accident codes. Goal of those analysis are to determine the susceptibility of a new rector design to the development of a HCDA and to estimate the severity of the potentially resulting accident. Fluid transients, energy release rate, and structural deformation interact strongly during the expansion phase of a HCDA. Current severe accident codes like SIMMER, used to analyze the expansion phase of SFRs, neglect the Fluid-Structure Interaction (FSI) between coolant slug and vessel wall, assuming a rigid geometry. Dedicated FSI codes like EUROPLEXUS on the other hand, used as well in the context of expansion phases in SFRs, employ simplistic models for the energy release rate. Codes that describe all three aspects of the problem mechanistically were unavailable until now.

This work describes the extension of SIMMER-III with an FSI model, offering the possibility to mechanistically model interaction between energy release rate, fluid transient and structure dynamics in the context of HCDAs in SFRs. The FSI extension relies on a second order Finite Element Model (FEM) to determine the structural feedback and uses a multilinear hardening model to describe elasto-plastic material behavior. The FEM code handles 3D and 2D- axisymmetric geometries. Structural- and fluid-dynamic modules of the extended SIMMER-III code are loosely coupled and I employ a Volume-Of-Fluid (VOF) approach to represent the vessel wall's radial displacement on SIMMER's structured grid. Through the use of the numerical library PETSc, developed by the Argonne National Laboratory, different nonlinear solvers, time-stepping routines, and preconditioners are available.

This work includes the verification of models for both the structural module and the coupled FSI code. It compares the results of the standalone structural FEM analysis with the analytic solutions for bending beam problems, deflecting cylinder and tensile tests for the elasto-plastic material model. For the coupled code, comparing numerical results for a sodium-hammer problem with a two-equation model serves as verification case. Results from both, standalone and coupled code, are in good agreement with analytic solutions. The results from an experimental study of a modelled expansion phase in a cylindrical, water-filled test vessel, conducted in 2008 by Nakamura et al., serves as the validation case for the extended SIMMER code. Pressurized gas, entering the test vessel from below, models the vapor explosion in this setup and accelerates a water slug upwards. Experiments were carried out with both a rigid, thick-walled vessel, and a flexible, thin-walled vessel which experienced plastic deformation at slug impact. Numerical and

experimental results of pressure history at selected points and deformation of the vessel wall are in good agreement as well.

An analysis of the expansion phase in a generic medium-sized SFR investigates the usefulness of the newly developed code, and compares the results obtained with extended, FSI-coupled and original, uncoupled code respectively. Basis for the analysis are three cases, each starting with the idealized condition of a molten core with a uniform temperature. Only the most intense of the three cases, assuming an unrealistically high initial fuel temperature, provokes a significant plastic deformation of the vessel. The resulting deformation surpasses the limits for the infinitesimal strain structural model and provokes an early termination of the analysis.

This work shows how an existing severe accident code, relying on a 2D structured grid, can be extended to account for radial deflection of the vessel wall during the expansion phase of a HCDA. Successfully run validation- and use-cases prove the reliability of the concept. The analysis of the expansion phase in a realistic SFR design demonstrates the usefulness of the extended code in real-world severe accident analysis. A comparison of results from analysis with flexible and rigid vessel respectively, shows an impact of the vessel deflection on the mechanical work release.

Abstract (Deutsch)

Im Falle einer schweren Störung können natriumgekühlte, schnelle Reaktoren (*Sodium Cooled Fast Reactors*, (SFR)s) eine teilweise Zerstörung des Reaktorkerns erfahren. Die veränderte Zusammensetzung von spaltbarem Material nach einem solchen *Hypothetical Core Disruptive Accident* (HCDA) kann zu einer prompt kritischen Konfiguration führen. Die resultierende Leistungsexkursion verdampft einen Teil des Kerns und der sich bildende Dampfdruck treibt geschmolzenen Brennstoff aus dem Kernbereich in das Kühlmittelbecken, was dort zu einer Dampfexplosion führt. Während dieser Expansionsphase beschleunigt die Kühlmitteldampfblase einen Natriumpfropfen, der auf den Reaktordeckel auftrifft und die Integrität des Reaktorbehälters herausfordert.

Der Entwicklungsprozess eines SFR umfasst Studien zu solchen extrem unwahrscheinlichen Ereignissen mit speziell hierfür entwickelten *Severe Accident Codes*. Ziel dieser Analysen ist es, die Anfälligkeit eines neuen Rektorenkonzepts für die Entstehung eines HCDA zu bestimmen und die Schwere des potenziell daraus resultierenden Unfalls abzuschätzen. Fluidtransienten, Energiefreisetzungsrate und strukturelle Verformung interagieren während der Expansionsphase eines HCDA. Aktuelle Severe Accident Codes wie SIMMER, die zur Analyse der Expansionsphase von SFRs verwendet werden, vernachlässigen die Fluid-Struktur-Interaction (FSI) zwischen Kühlmittelpfropfen und Behälterwand unter Annahme einer starren Geometrie. Spezielle FSI-Codes wie EUROPLEXUS hingegen, die auch im Rahmen von Analysen zu Expansionsphasen in SFRs verwendet werden, greifen auf vereinfachte Modelle für die Energiefreisetzungsrate zurück. Codes, die alle drei Aspekte des Problems mechanistisch beschreiben, waren bisher nicht verfügbar.

Diese Arbeit beschreibt die Erweiterung von SIMMER-III um ein FSI-Modell, das die Möglichkeit bietet, die Wechselwirkung zwischen Energiefreisetzungsrate, Flüssigkeitstransienten und Strukturdynamik im Kontext von HCDAs in SFRs mechanistisch zu modellieren. Die FSI-Erweiterung stützt sich auf ein Finite-Element-Modell (FEM) zweiter Ordnung, um die strukturelle Rückkopplung zu bestimmen, und verwendet ein multilineares Härtungsmodell zur Beschreibung des elastoplastischen Materialverhaltens. Der FEM-Code arbeitet sowohl mit 3D-, als auch 2D-axisymmetrischen Geometrien. Strukturelles und fluiddynamisches Modul des erweiterten SIMMER-III-Codes sind miteinander lose gekoppelt. Ein Volume-Of-Fluid (VOF)-Ansatz beschreibt die radiale Verschiebung der Behälterwand auf dem strukturierten SIMMER-Rechengitter. Mithilfe der vom Argonne National Laboratory entwickelten numerischen Bibliothek PETSc kann auf verschiedene nichtlineare Löser, Zeitschrittroutinen und Preconditioner zurückgegriffen werden.

Diese Arbeit umfasst die Verifizierung von Modellen sowohl für das Strukturmodul als auch für den gekoppelten FSI-Code. Es vergleicht die Ergebnisse der eigenständigen strukturellen FEM-Analyse mit den analytischen Lösungen für Biegebalkenprobleme, Biegezylinder- und Zugversuche für das elastoplastische Materialmodell. Für den gekoppelten Code dient der Vergleich numerischer Ergebnisse für ein Natriumhammerproblem mit einem Zwei-Gleichungsmodell als Verifizierungsfall. Die Ergebnisse sowohl von eigenständigem als auch von gekoppeltem Code stimmen mit den analytischen Lösungen überein. Die Resultate einer 2008 von Nakamura

et al. durchgeführten experimentellen Untersuchung einer modellierten Expansionsphase in einem zylindrischen, wassergefüllten Testbehälter dienen als Validierungsfall für den erweiterten SIMMER-Code. Unter Druck stehendes Gas, das von unten in den Testbehälter eintritt, simuliert die Dampfexplosion in diesem Versuchsaufbau und beschleunigt einen Wasserpfropfen nach oben. Experimente wurden sowohl mit einem starren, dickwandigen Behälter als auch mit einem flexiblen, dünnwandigen Behälter durchgeführt. Bei Letzterem trat eine plastische Verformung nach Aufprall des Pfropfens auf. Die numerischen Ergebnisse des Druckverlaufs an ausgewählten Punkten und die Verformung der Behälterwandwand stimmen ebenfalls gut mit den experimentellen Ergebnissen überein.

Eine Analyse der Expansion Phase in einem generischen mittelgroßen SFR untersucht den Nutzen des neu entwickelten Codes und vergleicht die Ergebnisse des erweiterten, FSI-gekoppeltem mit dem ursprünglichem, nicht gekoppelten Code. Grundlage für die Analyse sind drei Fälle, jeweils ausgehend vom idealisierten Zustand nach einer Kernschmelze mit einheitlicher Temperatur der Schmelze. Nur der intensivste der drei Fälle, bei dem eine unrealistisch hohe anfängliche Brennstofftemperatur angenommen wird, führt zu einer signifikanten plastischen Verformung der Behälterwand. Die resultierende Verformung überschreitet die Grenzen des Strukturmodells für infinitesimale Dehnungen und führt zu einem vorzeitigen Abbruch der Analyse.

Diese Arbeit zeigt, wie ein bestehender Severe Accident Code, der sich auf ein strukturiertes 2D-Rechengitter stützt, erweitert werden kann, um die radiale Verformung der Behälterwand während der Expansionsphase eines HCDA zu berücksichtigen. Erfolgreich durchgeführte Validierungs- und Anwendungsfälle belegen die Zuverlässigkeit des Konzepts. Die Analyse der Expansionsphase in einem realistischen SFR-Entwurf zeigt den Nutzen des erweiterten Codes bei der Analyse schwerer Unfälle in der Praxis. Ein Vergleich der Ergebnisse der Analyse mit einem flexiblen bzw. einem starren Gefäß zeigt einen Einfluss der Behälterdeformation auf die freigesetzte mechanische Energie.

Contents

List of Figures

List of Tables

Acronyms

ADS Accelerator Driven Systems.

ALE Arbitrary Lagrangian-Eulerian.

ANL Argonne National Laboratory.

ASTRID Advanced Sodium Technological Reactor for Industrial Demonstration.

BC Boundary Condition.

CDA Core Disruptive Accident.

CEA Commisariat à l'Energie Atomique et aux Energies Alternatives.

CFR-600 China Fast Reactor 600.

CG Cover Gas.

EBR-I Experimental Breeder Reactor I.

EOS Equations Of State.

EP Expansion Phase.

FBR Fast Breeder Reactor.

FCI Fuel-Coolant Interaction.

FE Finite Element.

FEM Finite Element Method.

FSI Fluid Structure Interaction.

FZK ForschungsZentrum Karlsruhe.

GIF Generation IV International Forum.

GMRES Generalized Mean RESidual.

HCDA Hypothetical Core Disruptive Accident.

IB Immersed Boundary.

IRSN Institut de Radioprotection et de Sûreté Nucléaire.

JAEA Japan Atomic Energy Agency.

JNC Japan Nuclear Cycle Development Institute.

JRC Joint Research Centre.

JSFR Japan Sodium-cooled Fast Reactor.

KIT Karlsruhe Institute of Technology.

LANL Los Alamos National Laboratory.

LOFA Loss Of Flow Accident.

LWR Light Water Reactor.

MPI Message Passing Interface.

MSR Molten Salt Reactors.

OECD Organisation for Economic Co-operation and Development.

PETSc Portable, Extensible Toolkit for Scientific Computing.

PFBR Prototype Fast Breeder Reactor.

PGSFR Prototype Gen IV Sodium Fast Reactor.

PRD Phenomenological Relationship Diagram.

PWR Pressurized Water Reactor.

SAS Safety Analyses System code.

SFR Sodium cooled Fast Reactor.

SFRs Sodium cooled Fast Reactors.

TOP Transient OverPower.

TPP ThermoPhysical Properties.

UIS Upper Internal Structures.

ULOF Unprotected Loss Of Flow.

VOF Volume Of Fluid.

Nomenclature

Operators and Functions

δ_{ij}	Kronecker delta function of i and j
∇	Differential operator
$t\vec{r}()$	Trace of a matrix
$H(x)$	Heavyside function of x

Subscripts

ep	Elasto-plastic
GL	Terms existing at interface between gas and averaged liquid velocity
HT	Heat transfer
M	Energy component
m	Density component
MF	Melting / freezing
N	Nuclear heating
q	Momentum component
qq'	Terms existing at interface between velocity fields q and q'
qS	Terms existing at interface between velocity field q and solid
VC	Vaporization / condensation

Variables

α	Volume fraction
α_{nf}	Non-flow area volume fraction
$\boldsymbol{N}$	Unit normal tensor to the yield surface
$\boldsymbol{\epsilon}^p$	Plastic strain tensor
$\boldsymbol{\epsilon}$	Cauchy strain tensor

$\boldsymbol{\sigma}$	Cauchy stress tensor
$\boldsymbol{D}$	Dampening matrix
$\boldsymbol{E}$	Total lagrange strain tensor
$\boldsymbol{F}$	Deformation gradient
$\boldsymbol{J}$	Consistent tangent stiffness
$\boldsymbol{M}$	Mass matrix
$\boldsymbol{P}$	First Piola-Kirchhoff stress tensor
$\boldsymbol{S}$	Second Piola-Kirchhoff stress tensor
$\boldsymbol{s}$	Deviatoric stress tensor
$\ddot{x}$	Second time derivative of the position
η	Factor in the linesearch method
Γ	Phase change rate per unit area
γ	Plastic consistency parameter
$\hat{\epsilon}_p$	Equivalent plastic strain
λ	Lamé's first parameter
$\mathbf{1}$	Second order unit tensor
$\mathbf{A}$	Stiffness matrix
μ	Bulk modulus
ν	Poisson ratio
Ω	Computational domain
ρ	Density
σ_y	Current yield stress
σ_{vM}	Von Mises stress
σ_{y0}	Initial yield stress
$\underline{\boldsymbol{B}}$	Strain-displacement relation tensor
$\underline{\underline{\boldsymbol{C}}}$	Fourth order constitutive tensor
$\underline{\underline{\boldsymbol{D}}}_{alg}$	Algorithmic tangent stiffness

$\underline{\underline{\boldsymbol{I}}}$	Fourth order identity tensor
$\underline{\underline{\boldsymbol{I}}}_{dev}$	Fourth order deviatoric identity tensor
$\vec{\Phi}$	Vector valued test function
$\vec{\Psi}$	Vector valued trial function
$\vec{a}$	Acceleration vector
$\vec{f_b}$	Body force vector
$\vec{g}$	Gravitational acceleration vector
$\vec{n}$	Unit normal vector
$\vec{P}$	Volumetric external force vector
$\vec{t}$	Traction vector
$\vec{u}$	Displacement vector
$\vec{v}$	Velocity vector
$\vec{X}$	Undeformed position vector
$\vec{x}$	Deformed position vector
$\widetilde{\alpha}_f$	Parameter of generalized alpha method
$\widetilde{\alpha}_m$	Parameter of generalized alpha method
$\widetilde{\beta}$	Parameter of generalized alpha method
$\widetilde{\gamma}$	Parameter of generalized alpha method
a	Binary-contact area per unit volume
b	Width
$C_{1..4}$	Integration cnonstants
C_{ep}	Elasto-plastic tangent stiffness
D	Flexural rigidity
E	Young's modulus
e	Specific energy
E_{kin}	Kinetic energy
h	Heat transfer coefficient

H_0^1	Sobolev space containing at least once continuously differentiable compact functions
h_{cell}	Cell height
I_y	Geometric moment of inertia
J	Jacobian of the deformation gradient tensor
K	Factor describing the momentum exchange between two components
K_{iso}	Isotropic hardening parameter
l	Length
M_B	Bending moment
p	Pressure
p_i	Internal pressure
Q	Source term
q_0	Constant line load
R	Mean radius
s	Wall thickness
T	Temperature
t	Time
v_0	Initial velocity
V_{cell}	Cell volume
V_{nf}	Non-flow volume
VM	Virtual mass force
W_{bubble}	Bubble work potential
W_{compr}	Compression work
W_{mech}	Mechanical energy

1 Introduction

In 1951, the Fast Breeder Reactor (FBR) Experimental Breeder Reactor I (EBR-I) was the first ever nuclear reactor to generate electricity harnessing nuclear power, marking the beginning of peaceful utilization of nuclear energy. While never a commercial success, FBRs were among the earliest reactor designs to sucessfully operate in a research environment. In contrast to the currently prevalent Light Water Reactor (LWR)s, where water as a moderator slows down the neutrons to a *thermal* spectrum, FBRs operate with a fast neutron spectrum. This entails some interesting advantages over LWRs with their slower (thermal) neutron spectrum.

First, a fast neutron spectrum allows for a reactor design which *breeds* more fissile material from ^{238}U than it consumes during operation. The *conversion factor*, which describes the amount of fissile material generated per amount consumed, can exceed one in FBRs [Sal05] while it lies around 0.6 for current LWRs [UOK$^+$07]. The higher conversion ratio increases the degree of utilization of uranium significantly. At a the rate of consumption as of 2016, the Organisation for Economic Co-operation and Development (OECD) expects global uranium ressources to last for another 130 years while projecting an increase in global demand of 15% to 45% by 2035 [NI18]. Fast reactor technology can greatly extend the availability period of uranium ressources.

Second, recycling and transmutation of minor actinides can reduce the radiotoxicity period for nuclear waste to 500 years compared to 100'000 years in an open cycle scenario [GPD$^+$03]. Fast reactors are particularly well suited for this task [Sal05], performing twice as well as Pressurized Water Reactor (PWR)s [GPD$^+$03]. By both using available uranium ressources more efficiently and more effectively transmuting minor actinides during recycling, FBRs produce less nuclear waste with lower radiotoxicity compared to LWRs of the same size.

Despite the technology offering benefits over current commercial reactors and promising prototypes, fast reactors come with their own set of challenges. Two important characteristics of FBRs related to reactor control and safety are their inherently positive void coefficient and the lower rate of delayed neutrons compared to thermal spectrum rectors. Both make design and operation of FBRs more challenging compared to LWRs. Since water serves as a moderator, slowing down neutrons to a thermal spectrum, fast spectrum reactors must rely on other coolants. For metal cooled, and sodium cooled fast reactors in particular, the handling of coolant is another aspect that is technically more challenging than in LWRs. Major issues at both Superphénix in France and MONJU in Japan were related to coolant leakage.

Nevertheless, the benefits from FBRs lead to a continued interest in the concept. Since much of the technology required to building and operating Sodium cooled Fast Reactors (SFRs) is readily available and has proven reliable in the past, they are an interesting candidate for future commercial application. SFRs are part of the Generation IV International Forum (GIF)'s list of *Generation IV* reactor technologies for potential commercial use from 2030 on. As such, development of SFRs continues in France with Advanced Sodium Technological Reactor for Industrial Demonstration (ASTRID), in Japan with Japan Sodium-cooled Fast Reactor (JSFR), as well as in Russia (BN-800, BN-1200), China (China Fast Reactor 600 (CFR-600)), India (Prototype Fast Breeder Reactor (PFBR)) and Korea (Prototype Gen IV Sodium Fast Reactor

(PGSFR)) [ADH+14]. A crucial part of the development process is the safety analysis of new designs and the constant improvement of reactor and plant safety.

Numerical analysis has been a valuable instrument in judging the safety of nuclear reactor designs for decades [FRS+76] [TB84] [BL90] [YFT+03]. For fast neutron type reactors with their notoriously positive void coefficients, those analysis are key in detecting and correcting design flaws early on in the design process. Over the years, countless contributions have improved the reliability of numerical predictions. Primarily enabled through the advances in computational capacity, numerical models became more accurate and complex at the same time.

State of the art reactor safety codes include a complex array of physics models to accurately depict the actual mechanics of processes describing the behavior of a nuclear reactor. Those *mechanistic codes* model the release and conversion of nuclear energy, transient fluid behavior and phase changes of structural material, fuel, and coolant inside the reactor.

1.1 Hypothetical Severe Accidents

Nuclear reactors can develop instabilities that lead to uncontrolled release of energy. Anomalies occurring during operation or introduced from outside can lead to a destabilization of the nuclear chain reaction. In extreme scenarios, such perturbations can circumvent inherent safety mechanisms and cause permanent damage to the system, surrounding structures or larger areas when penetrating into the environment. To ensure that such a scenario is extremely unlikely, it is common practice to test a new reactor design against a set of failure scenarios.

One of the more severe and most relevant scenarios in the context of reactor safety analysis is the Unprotected Loss Of Flow (ULOF). It assumes a simultaneous failure of all control mechanisms[1] for the nuclear chain reaction and stop of coolant circulation through the core. A local blockage in a core region or simultaneous failure of all coolant pumps can compromise coolant circulation. Local overheating or failure of even one component should trigger an immediate, controlled, and safe shutdown of the reactor. An array of redundant mechanisms ensures execution of the shutdown signal even after partial system failure. The simultaneous failure of all safety mechanisms is a highly unlikely event. These scenarios are commonly known as *hypothetical* severe accident scenarios due to their highly unlikely incidence.

Local overheating, as result of a malfunction or external perturbation, can cause (partial) disintegration of the reactor core. The next section presents the evolution and different stages of such a *core disruptive accident*.

1.1.1 Core Disruptive Accidents

Failure to remove the heat generated inside the reactor can damage the reactor core. These Core Disruptive Accident (CDA), or, Hypothetical Core Disruptive Accident (HCDA) scenarios play an important role in reactor safety analysis. Depending on reactor configuration and initial conditions, such an accident can either lead to a stable and coolable, or prompt critical reactor configuration as discussed in the following.

Depending on whether the reactor shuts down in time or not, we distinguish between a *protected* (shutdown achieved) or an *unprotected* (continued nuclear chain reaction) scenario. In a protected

[1] Control- and shutdown rods as well as liquid neutron poison injection.

scenario, decay heat is responsible for the heat generation inside the core. In the unprotected case, the heat generation stems from the continued nuclear chain reaction and is up to two orders of magnitude bigger than in the protected case [TB84].

The initiative event for a protected CDA is typically a Loss Of Flow Accident (LOFA) where a lack of coolant circulation through the reactor core leads to insufficient heat removal. Unprotected CDAs can result from either a LOFA or an uncontrolled reactivity increase leading to the overheating of the core. Those Transient OverPower (TOP) accidents are sometimes the result of a preceding LOFA voiding part of the core. The power production during a TOP accident can reach up to 40'000 nominal power.

In some cases, the reactor returns to a stable state after the initial perturbation. In other cases, a perturbation my lead to a violent disassembly of the entire system. To better describe an accident scenario, there is a commonly used nomenclature to characterize each step in the progression of the accident. The following sections describe the different phases and commonly used nomenclature in the evolution of a HCDA.

1.1.2 Initiation Phase

The initial perturbation occurs during the so-called *initiation phase*. Whether the system can overcome the departure from stationary operation depends on momentary configuration of the reactor, as well as the extent and nature of the disruption.

The system balances out small perturbations and either returns to normal operation or shuts down in an orderly fashion. This requires the use of control and shutdown mechanisms. After shutdown, the cooling system removes the nuclear decay heat and the reactor reaches a stable configuration. If control-, shutdown-, or heat removal mechanisms fail, the accident progresses.

Failure to contain the initial perturbation can lead to local overheating. Either due to a lack of heat removal (LOFA) or as the result of a small power excursion (TOP). If the temperature is high enough, coolant evaporates and voids the core. The result is a less efficient cooling of the core and, in an unprotected accident, a reactivity increase. If the temperature surpasses the melting point of cladding material or fuel, this changes the reactor geometry and initiates the transition phase.

1.1.3 Transition Phase

The overheating during the initiation phase has a chance of locally disintegrating the reactor core. This changes the reactor geometry and the allocation of fissile material in the core region. The change in geometry leads to a changed behavior of the entire reactor with respec to to coolant circulation and reactivity.

Again, there is the possibility that the reactor reaches a stable state after incurring little to no damage. In case the fissile material is sufficiently dispersed, the reactor becomes subcritical and the nuclear power generation comes to a halt even if the shutdown mechanisms fail. Although the reactor core has sustained some internal damage at this point, sustained heat removal is still possible and the containment would still be intact.

Should the change in geometry lead to supercritical, or prompt supercritical configuration, pressure and temperature in the core region rise abruptly. This *recriticality* results in the expulsion of molten fuel and steel from the core region and triggers the expansion phase.

1.1.4 Expansion Phase

A power excursion as the result of a recriticality releases up to 40'000 times the nominal power. Even though the excursion is not of long duration and quickly stopped through the Doppler effect, the amount of energy released is immense.

The released energy instantaneously vaporizes and melts part of the fuel and rod claddings. When this highly energetic mixture then comes in contact with the surrounding coolant, the ensuing thermal interaction creates a rapidly expanding, high pressure vapor bubble. The mechanisms is known as Fuel-Coolant Interaction (FCI) or alternatively as vapor explosion [Buc74] and described in more detail below in section 1.1.4.

Fuel-Coolant Interaction

The thermal interaction between hot corium [2] and surrounding liquid coolant is a complex mechanism that requires careful modeling. The phenomenon occurs in a similar manner whenever a hot liquid comes in contact with a cooler liquid having a lower evaporation temperature. But it is of particular interest in the context of severe accidents in nuclear reactors.

Vapor explosions form in several steps, while the process can come to a sudden halt at every stage in case the conditions for a further progression are not met [ANH02]. Figure 1.1 gives an overview of the FCI sequence leading to the formation of a highly energized vapor bubble.

At first, hot corium droplets come in contact with the low temperature coolant. This leads to film boiling and a coolant vapor bubble forms around the corium droplets, separating liquid coolant and corium. In case the coolant temperature is close to the saturation temperature, the initial vapor film forming around the fuel droplet stabilizes. Since the vapor cushion does not re-collapse in that case, the lack of further dispersion prevents the occurrence of a vapor explosion. [ANH02]

If the temperature of surrounding coolant is sufficiently lower than the saturation temperature, the heat transfer between coolant vapor and liquid coolant causes the vapor bubble to re-collapse. This phenomenon is also known as a *Taylor instability*. The ensuing impact of coolant breaks up the corium droplet and disperses them. The process then starts again, now with a larger total surface. In case of water/steel vapor explosions,the surface area increases by a factor of 10^3 [Buc74]. This produces a large, high energy coolant vapor bubble inside the core region. The rapid expansion of this bubble translates into mechanical energy that causes a violent disassembly of the core structure. This violent core disassembly and rapid further expansion of the vapor bubble can also compromise the integrity of the reactor vessel.

Pressure and size of the vapor bubble strongly depend on factors like quantity and temperature of the ejected liquid fuel, temperature and pressure of the surrounding coolant and initial mixture of fuel droplets with the coolant [IATT92].

[2] The mixture of molten fuel and cladding material is commonly referred to as *corium*.

As a multi-phase, multi-component code, SIMMER-III is capable to analyze the premixing phase and ensuing vapor bubble formation and expansion during an FCI scenario [MKTB99].

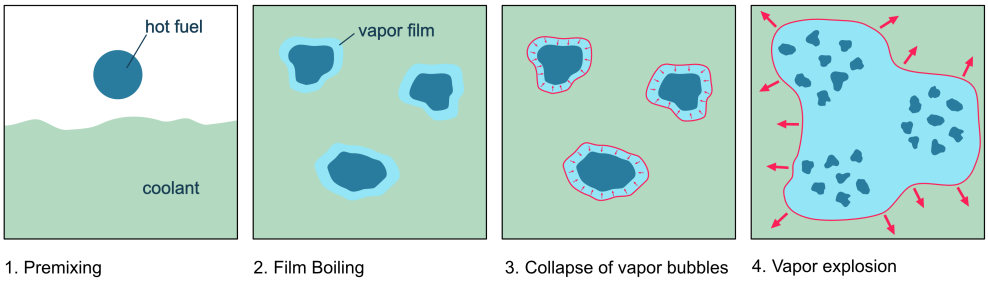

Figure 1.1: Vapor explosion caused by constant film boiling and re-collapse of vapor bubbles dispersing hot corium into the coolant and producing a large, violently expanding vapor bubble.

The vapor bubble resulting from the FCI accelerates a coolant slug upwards where it hits the reactor vessel lid after compressing the cover gas cushion. The resulting impact causes a deformation of the reactor vessel and challenges its integrity.

Structural Response

The violent expansion of the high pressure vapor bubble in the core region puts strains on the internal structures and the reactor vessel wall. The mechanical energy contained inside the bubble can permanently deform the structures and challenge the integrity of the vessel.

The structural response can influence the evolution of the expansion phase in several ways. First, deformation or disintegration of internal structures can influence the flow path of coolant through the reactor. This is important during the expansion phase itself but even more so during post-accident heat removal.

Second, during the initial (partial) meltdown of the core, a fuel crust can form around the core region. Effectively sealing off the core region from the surrounding coolant. This enclosure acts as a sort of containment for the vapor expansion if it stays intact during the expansion phase. SIMMER-III currently lacks a model for mechanical breakup of this fuel crust. This leads to nonphysical predictions regarding the accident progression if not manually corrected by the user.

Third, the plastic deformation of internal structures absorbs mechanical energy from the vapor bubble. The reduced energy of the bubble leads to a less violent outcome of the expansion phase and the resulting impact of coolant on the vessel lid.

Fourth, the deformation of the reactor vessel wall itself changes the internal volume and with it the internal pressure. This too can lead to a different progression of the accident since pressure perturbations are favorable to the formation of vapor explosions[IATT92]. Also, the question of structural integrity of the reactor vessel arises. The load on the vessel wall stands in direct relation to the structural response of the vessel itself. An outward deflection decreases internal

pressure. And plastic deformation can even permanently absorb part of the kinetic energy from coolant slug impacts.

The disintegration and redistribution of fissile material within the core also plays a role. But this effect is secondary during the expansion phase and becomes important when investigating the possibility of recriticalities. Movement of solid fuel rod pieces changes the distribution of fissile material and can lead to a different but critical configuration.

The current version of SIMMER-III is limited in its capabilities to account for structural response during a hypothetical severe accident. Conducting a coupled structural analysis however is important because it can change the course (mechanical breakup of crust) and outcome (structural integrity) of the expansion phase.

1.2 Motivation and Scope of this Work

1.2.1 Motivation

A HCDA scenario in a nuclear reactor involves three relevant physical domains. The first domain concerns the energy release rate which depends on neutronic effects, as well as material temperatures and densities. The conversion from nuclear to mechanical energy involve the partial meltdown of the core and interaction between liquid fuel and coolant. Section 1.1.4 goes more into detail on FCI.

The second domain refers to the fluid transients of coolant, and molten fuel and steel. Fluid dynamics are responsible for convective heat transfer, conversion between work potential and kinetic energy of fluids, and dissipative effects. They have an important impact on local temperatures, pressures, and densities. Which, in turn, influence the energy release rate.

The third domain is the structural domain. Structural dynamics change the reactor geometry and influence flow paths, total volume, and can dissipate energy if plastic deformation occurs. Through this, it has an impact on the fluid transient and indirectly influences the energy release rate.

Dedicated models and analytic instruments relying on numerical methods are available for all three domains. Commercial, proprietary, and open source implementations exist both for the structural-, and the fluid dynamic domain. Codes for the analysis of nuclear energy release and FCI are less common as the relevance of those phenomena outside the area of reactor physics is negligible.

Less codes and models exist for the coupling of two of those domains. The treatment of Fluid Structure Interaction (FSI) problems is relevant in several industries. The availability of respective models and codes reflects this circumstance. Codes that account for interaction between energy release rate and fluid transients have a much narrower area of application. Those *mechanistic severe accident codes* are mainly applied to analyze HCDAs in nuclear reactors. SIMMER-III is an instance of such a mechanistic severe accident code and used for HCDA analysis by the Japan Atomic Energy Agency (JAEA) and the Commisariat à l'Energie Atomique et aux Energies Alternatives (CEA).

During a HCDA, all three effects play an important role and interact with one another: energy release rate, structural dynamics, and fluid transient. An instrument for the mechanistic

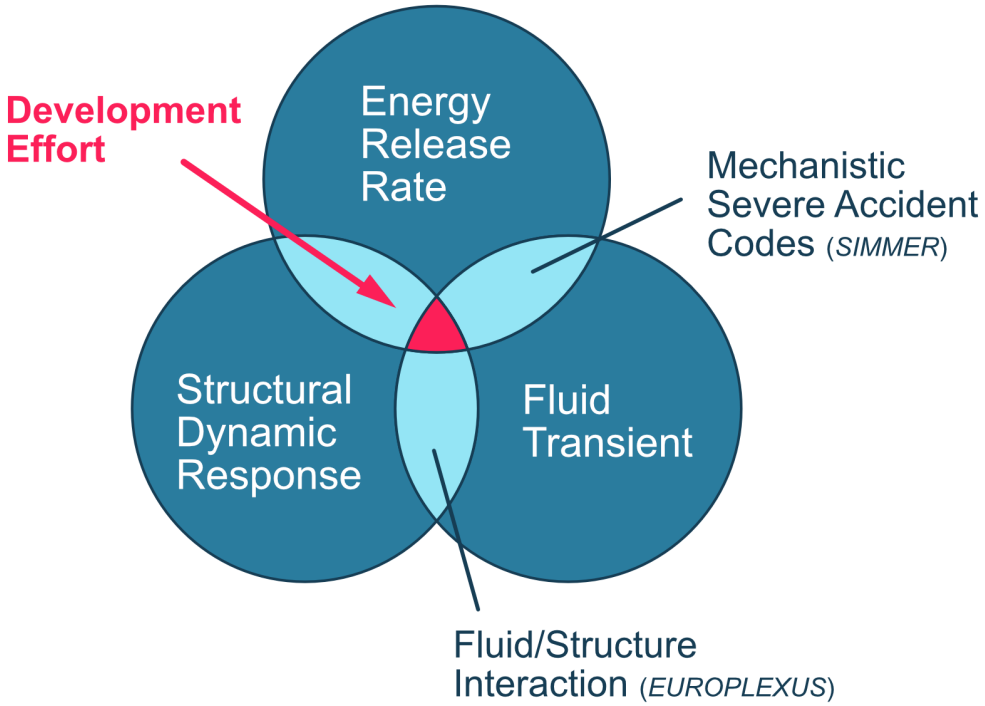

Figure 1.2: Important physics domains for the analysis of hypothetical core disruptive accidents with examples of currently available codes to illustrate the present development effort.

treatment of all three effects simultaneously was unavailable to date. This work aims to extend SIMMER-III to incorporate the structural dynamic response in HCDA analysis.

Direct interaction between energy release rate and structural dynamics can occur in the form of thermal deflection of unevenly heated fuel rods. This effect is not considered in the scope of this work.

1.2.2 Scope

The current capabilities of the mechanistic severe accident code SIMMER are limited in the sense that it does not account for structural dynamic response during the accident evolution. The goal of this work is to prove the feasibility of extending the existing SIMMER code base by a structural model. And then, to investigate the impact of structural response on the results of a CDA analysis.

The effort breaks down into five parts. First, the conception of a model to represent structural feedback in the existing code base. This includes implementing moving boundaries and a changing domain geometry on SIMMER's regular, fixed grid.

Second, the development of a structural dynamics analysis tool that integrates seamlessly with SIMMER. The structural code should handle dynamic problems and nonlinear (elasto-plastic)

material behavior. Without increasing the numerical effort to a point where a coupled analysis becomes uneconomic. To account for other phenomena and nonlinearities in the future, an extendable solution is preferable, facilitating prospective development efforts.

After implementation of structural analysis and coupling mechanism, the extended code needs to prove its consistency with the physical model. The standard verification procedure is to compare the numerical results to a set of analytic reference solutions.

Subsequently to confirming the correct formulation of the numerical models, the validation process follows. Application to a more demanding problem with available experimental results establishes the suitability of the coupled code to the desired family of problems.

In a last step, the newly developed code needs to demonstrate its effectiveness in a production environment. New and old version of the code analyze a selection of reference problems. A comparison of results establishes the benefits and limitations of the new model.

In this chapter, I proposed the introduction of a structural dynamics model in the mechanistic severe accident code SIMMER to improve the quality of severe accident analysis. A quick presentation of severe accident evolution gave an insight into why structural dynamics play an important role in core disruptive accidents, and underlined the importance of accounting for energy release rate, fluid transients and structural dynamics simultaneously. Last, I discussed the scope of this work and gave a short summary of the general approach to the problem. The following chapter will go into detail on the state of the art in severe accident, fluid-structure interaction, and structural analysis to illustrate in more detail how the present development effort fits in compared to previous achievements.

2 State of the Art

The analysis of severe accidents in nuclear reactors requires the simultaneous consideration of the energy release rate, as well as fluid transient and structural dynamic effects. Dedicated numerical models exist for all three physical domains and are continuously improved. Models for coupling two regimes to account for interactions between the domains are also available. Due to the complexity of coupled problems, experimental studies are a helpful tool to improve understanding and validate numerical models.

This chapter presents state of the art numerical models and recent development efforts as well as relevant experimental studies. It also illustrates the need for a numerical tool to simultaneously consider all three domains for an improved description of hypothetical severe accidents in sodium cooled fast reactors.

2.1 Severe Accident Codes

Significant departure from normal operation of a nuclear reactor can provoke a severe accident. The sequence of events leading to such an accident often includes the failure of control and shutdown mechanisms. This leads to the progression of an initial malfunction and a potential (partial) disintegration of the reactor core culminating in an uncontrolled release of nuclear power and the disassembly of core and vessel.

Estimating the probability and severity of such hypothetical severe accidents requires a detailed understanding of the reactor behavior when operating outside the design parameters. Numerical models for the analysis of severe accident scenarios exist since the dawn of nuclear power generation and see continuous improvement. Since different phenomena dominate the distinct stages of a severe accident, as presented in section 1.1.1, the use of dedicated codes for particular stages is common practice.

In the following, I will present two approaches to modeling transient reactor behavior. They produce the two most relevant codes in the context of severe accident analysis in Liquid Metal cooled Fast Breeder Reactors (LMFBR). SAS and SIMMER concentrate on initiation and transition / expansion phase respectively.

2.1.1 SAS Code Family

As described in section 1.1.1, a severe departure from normal operation in a nuclear reactor can lead to a partial disintegration of the reactor core in the so-called initiation phase. During the 1960's, the Argonne National Laboratory (ANL) began the development of the Safety Analyses System code (SAS) to numerically analyze the initiation phase of a hypothetical core disruptive accident in a sodium cooled fast neutron reactor[BF17] [TPWW10].

Since then, the code has seen continuous improvements. A consortium of JAEA, Karlsruhe Institute of Technology (KIT), CEA and Institut de Radioprotection et de Sûreté Nucléaire (IRSN) now maintain and advance the development of SAS-SFR, the current, Sodium Fast Reactor version of the SAS code [LAB+14] [TPWW10].

Since version SAS3A, the code mechanistically treats the melting and subsequent reallocation of fuel and cladding material [BF17]. Version SAS4A saw an improvement of those models along with the introduction of fuel element deformation and disruption models.

SAS-SFR divides the core geometry into subchannels, each containing a number of assemblies, to perform transient analysis of design base and beyond design base accident scenarios. The code assumes identical behavior for all assemblies inside a subchannel, and a one-dimensional flow inside the assemblies.

Once the assembly wall disintegrates, flow conditions in the reactor core region become multi-dimensional. The fundamental assumption of a one-dimensional flow regime mentioned above is then no longer valid. This event marks the end of a SAS-SFR analysis.

The SAS code family has a modular structure and the user can chose an adequate module setup to analyze different reactor types. Models for oxide- and metallic fuels are available. As well as models for multi-phase flow regimes and melting/freezing processes inside each assembly. The current version can model the behavior of the entire plant. In the analysis of passive safety feedback, the whole-plant dynamics model is key [BF17].

SAS4A and SAS-SFR are the worldwide standard for the analysis of initiation phases in Sodium cooled Fast Reactor (SFR) HCDA [BF17]. They allow the analysis of vertical material allocation after initial disintegration of single fuel pins under the consideration of multi-phase flow regimes and whole-plant dynamic behavior. After liquid fuel breaches the canwalls lateral fuel reallocation becomes important, the analysis with SAS terminates. The current reactor configuration at this moment serve as initial conditions for a subsequent analysis with SIMMER which the following sections describes in more detail.

2.1.2 SIMMER

After disassembly of fuel pins and canwalls, reallocation of fissile material in a nuclear reactor can, once again, lead to a (prompt) critical configuration. The SIMMER code family [MRS+03] [MRSW05] allows to analyze the risk of such recriticalities occurring in sodium cooled fast reactors. SIMMER-III [KTMS92][TKY+05] is the 2-D, and SIMMER-IV [YFT+03] [YTF09] the 3-D version of the Eulerian, multi-phase, multi-component fluid dynamics code coupled with space-, time-, and energy-dependent neutron transport models.

The Los Alamos National Laboratory (LANL) initially developed SIMMER after identifying the need for a tool to continue analysis of HCDAs after the assumptions for the SAS code family no longer held [BHRB76]. A consortium of Japan Nuclear Cycle Development Institute (JNC), CEA, and ForschungsZentrum Karlsruhe (FZK) then took over the development of SIMMER in 1989 [CMR02].

The resulting SIMMER III and IV are current state of the art codes for analyzing hypothetical severe accidents in fast neutron reactors[TPWW10]. Both codes pick up the analysis in the transition phase after an initiating event has compromised the steady state operation of the reactor and lateral movement of liquid fuel sets in.

Originally developed for the analysis of HCDAs in sodium cooled fast reactors, the versatility of SIMMER allows for analysis of other reactor types. Constant development of new models[MRSW05] allows to apply the code for the analysis of reactor types with different coolants and varying neutron spectra. Including reactors with transmutation capabilities [MRSW05], Accelerator Driven Systems (ADS) with lead-bismuth or lead cooling [MRK+01], gas cooled fast reactors [CMR02], Molten Salt Reactors (MSR) [WRM06], and supercritical water fast reactors [MMLM03].

The SIMMER codes consist of three fundamental modules treating fluid transients, structural heat transfer and breakup, and neutron flux transients respectively. The section below discusses the three modules in more detail. Figure 2.1 gives an overview of the framework for the SIMMER code family [MRS+03].

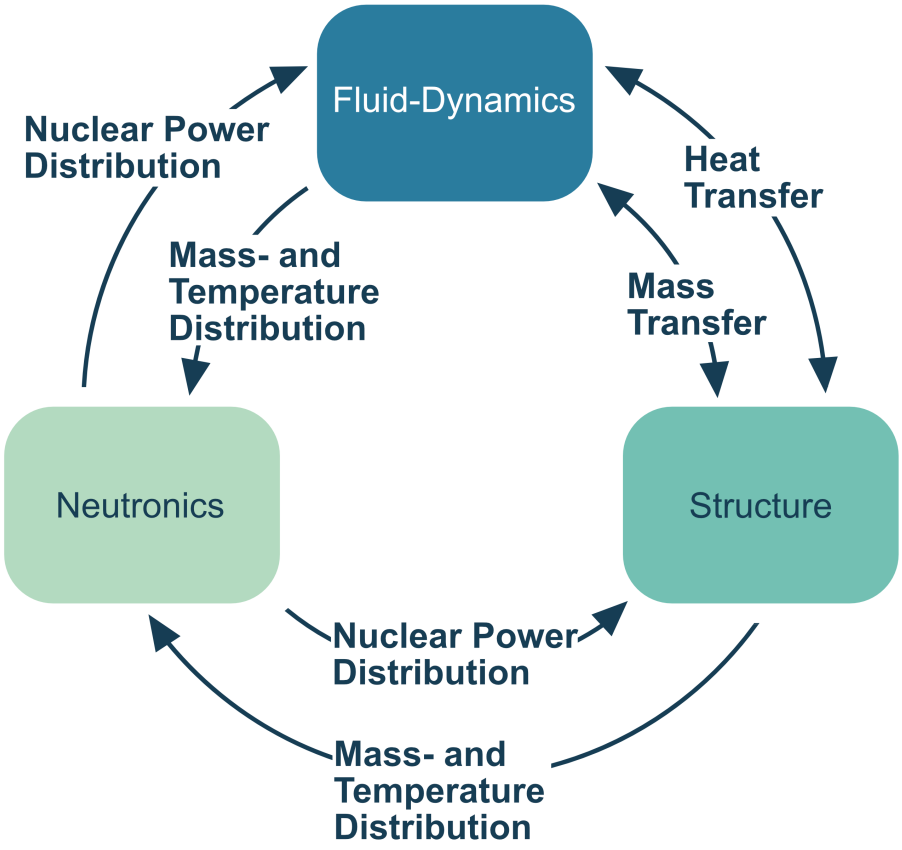

Figure 2.1: Code structure of the SIMMER-III and SIMMER-IV code family.

SIMMER Fluid Dynamics Model

In HCDAs, melting of fuel and cladding as well as vaporization of coolant lead to multiple components and phases interacting with one another and with the surrounding structure.

SIMMER uses up to six velocity fields to accurately model the fluids and their respective behavior during the accident evolution. Each component is associated with a velocity field. Multiple components can share the same velocity field. Within each field, SIMMER solves the fundamental equations for the conservation of mass, momentum and energy. Section 3.1 elaborates on the model and equations.

To close the fundamental equations, and to account for vaporization and condensation effects, SIMMER relies on an analytical Equations Of State (EOS) model[MF98][MKTB99]. It relates current pressure, density and temperature in each component through polynomial functions. For the modeling of heat and mass transfer, the change of ThermoPhysical Properties (TPP) plays an important role. The TPP model used by SIMMER is also analytical [MTKF99].

In multiphase cells, SIMMER treats intra-cell heat and mass transfer and momentum exchange. Depending on the amount of gaseous phases in a cell, the fluid mixture behaves differently. SIMMER determines the respective flow regime and employs the adequate equations and coefficients for pressure loss, and intra-cell momentum exchange.

SIMMER's multi-phase, multi-component fluid dynamics module ensures energy, momentum, and mass conservation while relying on an analytical EOS model to close the equations.

SIMMER Structure Model

Local temperatures and structural breakup play an important role during HCDAs. In its structure model [KK04], SIMMER accounts for conductive heat transfer through structural components such as the fuel pin itself, cladding, and can walls. A thermal breakup condition initiates the disintegration of structural components.

All structural components in SIMMER-III are solid and stationary. Structural movement is solely possible in the form of particulate flow after structural breakup. Can walls, defined in the structural model, guide the flow through the reactor and do not permit lateral fluid motion. Adequate hydraulic diameters allow to quantify the momentum exchange between fluid and structure.

For the calculation of heat transfer between structure and surrounding fluids, SIMMER relies on a loose coupling between both models. In the simplest model version, both can wall and pin consist of two nodes – an internal and an external one. The calculation of internal heat transfer relies on an implicit formulation.

Modeling of pin / structural failure and disruption rely on a thermal breakup criterion. Additionally, the disintegration of supporting structures can also trigger the breakup. After disruption, SIMMER considers the former structural components as fluids. Either in the form of particulate flow or, if the temperature is sufficiently high, as molten fuel and steel. In case the temperature drops below the melting point, re-solidified material can deposit on the can walls. The resulting crusts are part of the structural model and considered for heat transfer calculations.

SIMMER's structural model accounts for heat transfer within the structural components as well as between structure and fluid flow. A thermal condition initiates the structural breakup of fuel and steel. Structural model and fluid dynamics model interact through the exchange of heat, mass and momentum between both domains. Redistribution of structural material is possible through meltdown and re-solidification. But structural elastic or elasto-plastic behavior is not part of SIMMER's internal structure model.

SIMMER Neutronics Model

Current shape and intensity of the neutron flux are important to determine the momentary power distribution in a nuclear reactor. SIMMER relies on an improved quasi-static model to calculate the current neutron flux shape [MRS+03]. The solvers are based on the particle transport codes TWODANT [ABMO84] [BHK+99] and THREEDANT [Alc95] for the 2-D and 3-D formulations respectively. The neutronics model also handles the calculation of decay heat.

SIMMER is a mechanistic severe accident code with a multi-phase, multi-physics Eulerian fluid dynamics model coupled with a space-, time-, and energy dependent neutronics model and heat transfer in structural components. The code's primary task is the analysis of the transition phase during HCDAs in nuclear reactors. Recent efforts aim to extend the code to treat the initiation phase and post accident heat removal [YT11].

2.2 Fluid Structure Interaction

FSI is a phenomenon frequently encountered in diverse fields of research. We find manifestations of FSI in flow over airfoils such as airplane wings [BKRG98] and wind turbines[BHK+10]. In civil engineering, harmonic excitation of a structure through steady wind must be considered during every design process to avoid disasters such as the often cited Tacoma bridge's spectacular collapse in November 1940 [GU06]. In biotechnology and medicine, interaction between blood vessels or organs and circulating blood is one of the most important aspect of haemodynamics [CRD+11].

In nuclear engineering, FSI effects are important when analyzing different aspects of reactor behavior. Steady flow between internal structures such as control and fuel rods or instrumentation can cause harmonic oscillations [Paï83]. Transportation of loose structural parts and debris can cause blockage of essential flow paths and compromise local coolability of the reactor. A partial core meltdown can lead to the occurrence of *sloshing* whereby recurring nuclear power excursions provoke a sloshing motion of coolant and molten corium [FF09] [DGH82]. During the expansion phase, the violent disassembly of the core and rapid expansion of the vapor bubble lead to deformation of internal structures and vessel wall [Wol82]. Interactions between fluid and internal structure dissipate energy during the slug acceleration [ZW85].

To give an overview on the state of the art in FSI simulations, I will first characterize two fundamental concepts. Then, I will outline the landscape of approaches for coupling and boundary representations before presenting previous studies of fast transient FSI in general and CDAs in particular.

2.2.1 FSI Models

The models and equations we use to analyse fluid structure interaction vary strongly with the application. We generally distinguish between two main families of FSI models. On one hand, monolithic models [HWD04] [WKHD05] use a single set of equations to describe the behavior of both structure and fluid at the same time. At each time step, we solve a single system of equations.

Partitioned models [MS02] [PFO01], on the other hand use two different sets of equations to describe the behavior of fluid on one side and that of the structure on the other side. Using this approach, we need to solve two systems of equations each time step. One for each domain. This method requires an additional coupling step wherein both domains exchange information. Depending on the problem, we need to solve the fluid and structural state multiple times per time step to ensure coherent behavior.

The main differences between monolithic and partitioned approach are the development effort, computational cost, and numerical stability of the solver [HHB08] [MHvBdB04]. With the partitioned approach, one can rely on existing solvers for the fluid dynamic and the structural domain. The development effort concentrates on the formulation of a coupling routine between both domains. A monolithic solver implementation generally requires a development from scratch. Solving both domains simultaneously, the monolithic approach is less prone to numerical instabilities than the partitioned approach. Thanks to the stable behavior of monolithic solvers, they can cope with larger time step size. But since the computational cost per time step is higher than for partitioned solvers, both methods have a comparable computational efficiency [MHvBdB04]. Advances in the development of monolithic solvers may lead to an improvement in efficiency giving them an advantage over partitioned solvers [HHB08].

Partitioned approaches are still more popular for the time being, most importantly because they offer the possibility to use legacy codes. As mentioned above, they require the use of a coupling method to account for the interaction between both computational domains. The following section gives an overview of coupling approaches.

2.2.2 Coupling Approaches

When two sets of equations are used to describe the behavior of structural and fluid domain respectively, we need to employ two solvers as well. We need to instate a communication between both models so that changes in the respective other domain are taken into account. There are several ways to realize this coupling and the literature distinguishes between two groups of coupled solvers.

Both coupling schemes have in common that *coupling variables* are exchanged between both domains. This happens every time a solver of one domain has converged on a solution. The interaction between both domains happens at the fluid solid interface. Instead of the entire solution, usually only variables at the interface are exchanged. New boundary conditions are imposed at the interface to account for the response of the respective other domain.

In *tightly coupled* systems, several solver runs in both domains occur for each time step. In that way, we can ensure convergence between both domains. The reference to convergence of course means that there must be some notion for a residual error. This residual is a measure for the discrepancy between the respective solutions of structural and fluid domain. Both solvers run in alternating fashion and exchange solutions each time until the coupling residual becomes sufficiently small and *global convergence* is achieved. Tight coupling is especially helpful when solutions for structural and fluid domain tend to diverge quickly. For example when large time steps are chosen.

In *loosely coupled* systems on the other hand, each solver is called only once per global time step. This setup is more prone to divergence when choosing larger time steps. But the computational effort per timestep is significantly less. Especially when both domains are insensitive to small changes in the coupling variables, loose coupling can be a sensible choice. It is also much

more straightforward to implement since it requires no extra convergence check or reiteration procedure.

2.2.3 Fluid Dynamics with Moving Boundaries

Early era fluid dynamic analysis used a predefined, rigid domain that did not change shape or size during the analysis. Still today, the majority of fluid dynamic problems can be solved with a static domain and moving boundaries are a rarity. But in some cases, and especially in FSI problems, the computational domain is subject to changes which we must account for.

The following sections present an overview of models and approaches to represent moving boundaries in a fluid dynamics solver.

Arbitrary Lagrangian Eulerian Method

The Arbitrary Lagrangian-Eulerian (ALE) method was first mentioned by Hirt in the seventies [HaAC74]. The idea is to use a body conformal mesh in which grid points can either remain fixed (Eulerian) or move with the flow (Lagrangian). The resulting conservation equations are composed of an Eulerian and a Lagrangian term.

The main advantage of ALE methods is that imposing boundary conditions is straight forward. There are always discretization points located at the boundary.

The disadvantage of ALE methods is that the quality of the mesh can suffer significantly in case of large displacements of the boundary. When mesh quality becomes too low, we need to re-mesh the domain during computation. This means that we need to automate the meshing procedure and guarantee that the result conforms to the quality standards. Alternatively, we need to interrupt the computation each time the mesh quality falls below a threshold. And then perform the remeshing per hand.

Immersed Boundary Methods

In the seventies, Peskin developed the *immersed boundary method* [Pes72] [Pes77] [Pes03] to compute blood flow through the heart. He chose the – at the time – unconventional approach to perform his calculations on a Cartesian grid that did not conform to the heart's geometry. Instead, he introduced an additional source term to the fluid dynamics equations that enforces the boundary condition inside the fluid domain. Immersed boundary methods today exist in several flavors [MI05]. The forcing term can be either continuous or discrete in nature.

An important advantage of immersed boundary methods is that we can employ structured grids regardless of the geometry of the domain boundaries. This allows more freedom in the choice of numerical methods.

The main selling point of immersed boundary methods is that mesh generation becomes a straight forward task. Re-meshing is also not an issue since mesh quality does not diminish during runtime. The use of Cartesian grids does not come without problems however. Since the mesh is not body-conform, there is no straight-forward possibility to refine the grid near the immersed boundary. If the problem requires a fine grid close to the boundary, we need to refine the mesh everywhere.

Within the class of Immersed Boundary (IB) methods, we discriminate between the continuous forcing and discrete forcing approach. In both cases, an additional forcing term represents the immersed boundary.

In case of continuous forcing, the term is applied before discretization. Peskin's original approach [Pes72], as well as [SB96] and [GHS93] fall in this category. The continuous forcing approach is well suited for problems with fluid flow around elastic boundaries [MI05]. This class of problems corresponds well to the continuous forcing approach. With increasing stiffness of the immersed boundary the associated forcing term becomes pathological.

In case of discrete forcing, the forcing term is applied after discretization. Representative implementations are [UMS99], [UMRK01], [KKC01], and [GFCK02]. The discrete forcing approach is better adapt for problems with rigid immersed boundaries [MI05]. However, those methods usually require a modification of the numerical stencil. A good example is the cut-cell approach [CHS86] [UMRK01] where the affected finite volume is redefined (or *cut*) along the boundary to satisfy the conservation laws.

Volume of Fluid Methods

In the late seventies, Hirt [HN81] developed another approach for representing free boundaries in fluid flows. The idea is to define an additional field variable that describes the volume fraction of fluid contained in each cell. A cell where this variable takes the value one, is entirely filled with fluid. While a cell with the value zero is completely voided.

The Volume Of Fluid (VOF) method does not allow a sharp representation of the interface in the fluid dynamic mesh. But we can track, which cells the boundary cuts. As well as what the orientation of the boundary in the affected cells is. We can determine the orientation of the interface normal by looking at the change of the volume fraction field in space. The direction in which the field diminishes quickest is the direction of the interface normal.

The original VOF method tracks the interface by solving a transport (or advection) equation for the volume fraction field. In that way, it is possible to have moving internal boundaries. It was designed with multi-phase flow problems in mind but has been applied to FSI problems in the past [AWvJ08] [SC08].

Fictitious Domain / Lagrange Multiplier Approach

The Fictitious Domain method uses Lagrange Multipliers to account for the presence of a boundary in a (usually) regular mesh. The method is also known as *capacitance matrix* or *domain imbedding* method [GPP94]. The idea behind this elegant approach is to introduce and link the fundamental equations in the domain and the boundary conditions with a Lagrange multiplier [GPP94]. The problem then transforms to a saddle point problem which can be solved with a conjugate gradient algorithm.

The method is able to accurately represent moving boundaries in regular meshed domains [GPHJ99]. Unfortunately, the implementation is anything but straightforward. The Lagrange multipliers change the formulation of the original problem and retrofitting it to an existing fluid-dynamics solver is impractical.

2.2.4 Fast Transient Fluid Structure Interaction

For low Reynolds number single-phase flows, the fluid can mostly be viewed as incompressible [FP08]. This greatly simplifies the problem. Other applications however are more demanding. In some cases, acoustics might play an important role in the analysis. Shock or pressure waves in a fluid impacting a deforming solid are one example. Those effects are often linked with the occurrence of cavitation, further complicating the matter. This section presents an overview of recent studies on fast transient fluid structure interactions.

Iakovlev [Iak07] discussed the impact of cavitation on the structural dynamics of a cylindrical structure subjected to a shock wave. He derived a mathematical model to describe the behavior of a completely submerged and fluid-filled cylinder and concluded that under certain conditions, cavitation can threaten the structural integrity of the cylinder. This is due to a collapse of cavitation bubbles on the surface following a separation of the shell from the liquid.

Cirak et al. [CDM07] developed a framework to analyze the impact of strong pressure waves on submerged structures. They used a loosely coupled combination of Lagrangian finite elements for the structural dynamics and Eulerian finite volume approach for the fluid side. The fluid dynamics solver uses a Cartesian grid and the fluid/solid boundary is represented with a ghost-fluid approach. The structural model uses shell elements and is capable of treating visco-plastic deformation and rupture. Both fluid-dynamic and structural solver are explicit in time. Cirak et al. found that cavitation occurs near the fluid / solid boundary directly after impact of the pressure wave on the shell structure. Their code models shock wave propagation in gases and liquids. Pressure wave progression in both cases is modeled with the inviscid Euler equations. They use a constant volume burn model to describe gaseous detonations in gas-filled tubes.

Wardlaw and Lutton [WL00] studied fluid structure interaction in under-water explosions with regards to naval weapon design. They examined internal and external explosion cases. Finding that for internal explosions, reflection of the pressure wave on the gas bubble played an important effect on *reducing* the pressure between source and structural surface. The effect reduced the surface pressure significantly, inducing cavitation in the near-wall region. With increasing flexibility of the surface, the cavitation zone expanded. The collapse of the cavitation bubbles causes a secondary load on the structure. For external explosions, interaction between gas bubble and shockwave is negligible. They used a 2D Cartesian grid Eulerian approach to model fluid dynamics. The moving boundary is represented with a ghost-cell approach. Water is modeled with a modified Tillotson equation of state Structural dynamics are modeled with the finite element method.

In 2001, Chambers et al [CSZ+01] measured wall pressures on a water filled aluminum cylinder in response to an internal explosive charge. The measurements were done to validate a previously developed computer code. They confirmed the occurrence of cavitation at the wetted surface through measurements with pressure gauges. Noting that the effect complicated both numerical simulations and measurements during the experiments.

Experimental and numerical investigations for shock loading of more complex structural materials were also undertaken. Zhu et al. [ZZLG09] investigated the deformation of honeycomb structures sandwiched between two aluminum plates. This type of structure is capable of dissipating considerable amounts of mechanical energy due to their nature of undergoing large plastic deformations at nearly constant stress levels. They were able to reach good agreement between experimental and numerical results. They used the finite element code LS-DYNA to simulate both structure and explosive charge with an ALE formulation for the gaseous domain.

The above mentioned works concentrate on the impact of shock waves on the structure. The source of the pressure wave generally lies within the fluid surrounding the structure. Large scale movement of the liquid is not part of those studies and none treats the impact of a fluid slug on the structure.

2.3 Analysis of Expansion Phase

The Expansion Phase (EP) in core disruptive accidents has been studied in the past both numerically and in experiments. This section gives an overview on important contributions for both experimental and numerical studies. For numerical studies, the focus lies on FSI implementations and analysis. Section 2.1 treats the application of severe accident codes (without FSI) to CDAs and resulting EP.

2.3.1 Experimental Analysis of Expansion Phase

In the late seventies, CEA conducted the *CARAVELLE* experiments [BLP$^+$79] [Bre82] that have since been referenced in other works [BC96] [FBLD82]. The experimental setup consisted of a water-filled vessel similar to a small-scale model of the *Super Phénix* experimental reactor. Three different energy sources to initiate the expansion phase were used: Thermite, a low-pressure explosive and hot water.

During the same time, Saito et al. [SYI85] conducted experiments to determine the structural response of small scale reactor vessel models under HCDA conditions. They used a specifically developed, slow burning explosive to model the energy release during a HCDA and the conversion of thermal to mechanical energy through fuel coolant interaction. The experiments included different combinations of internal structures and varying materials.

Deflection curves from their 1/15, 1/22 and 1/33 scale models of a Monju-like vessel geometry suggest that two different mechanisms are responsible for the deformation of upper and lower part of the vessel respectively. The maximum plastic deformation occurs near the vessel lid as a result of the liquid slug impact. In the lower part of the vessel, plastic deformations are less pronounced and caused by the impact of the initial pressure wave from the energy source. They concluded that the deformation in the mid-part of the vessel depends more on the initial energy release behavior. While the deformation of the upper vessel part depends more on the total release of energy over time which accelerates the liquid slug. In vicinity of the structural plate on which the core rests appears no significant deformation.

Experiments with internal structures mounted suggest that they can greately reduce the total strain experienced by the reactor vessel. Especially the thermal shielding below the vessel lid could reduce the total strain energy in the upper vessel region by up to 90%. The plastic deformation of the shielding absorbs much of the dynamic energy of the liquid slug. By deviating the coolant flow, even completely rigid upper internal structures were able to reduce the total vessel strain.

2.3.2 Numerical Analysis of Expansion Phase

Breton [Bre82] also developed a code to predict the behaviour of actual reactors during the expansion phase. The code was one-dimensional and relied on input from experiments and other codes for its parametric models. It was capable of predicting the mechanical work potential of the expansion phase which could then be used to analyse the resulting stresses and strains in the reactor vessel with a separate code.

Earlier codes for HCDAs had mostly relied on purely Lagrangian formulations [BK76] [DFSG76]. In 1982, Donea et al. [DGH82] were the first to present an arbitrary Lagrangian Eulerian approach. Their two-dimensional code used a finite element formulation for both fluid and structural domain. The structural part of the code allowed for geometric and material non-linearities, using a large-displacement, small-strain formulation. For the material non-linearities, the code uses a von Mises yield criterion, a plastic flow rule and an isotropic strain hardening rule. The yield criterion and hardening rule are both dependent on the strain rate. The code did not allow for multi-phase flows although free surface modeling was possible thanks to the ALE formulation. They analyzed a thin cylindrical vessel with a hemispherical bottom partially filled with water and loaded by an explosive charge. The pressure and volume of the explosive charge region developed according to a polytropic gas law. The code was able to reproduce experimental results with reasonable accuracy.

Zeuch and Wang [ZW85] developed and used the ALICE-II code to study the impact of internal reactor structures on the structural response of the reactor vessel. They concentrated on evaluating different UIS designs with respect to their impact on the vessel's structural response during a HCDA. The study suggests that restricting the flow paths out of the core region can contain part of the high pressure vapor bubble and mitigate the load on the reactor vessel. Rigidity of internal structures as well as their geometry and relative position in the reactor played a role in reducing the primary vessel strain.

The EUROPLEXUS [CHVD79] [BCHL89] [LSB85] FSI code was developed jointly by CEA and Joint Research Centre (JRC) to specifically deal with impacts and explosions. It uses a finite element formulation and is capable of dealing with material and geometric non-linearities. Robbe et al. [RLC03] used EUROPLEXUS to re-examine the MARA 8 [FLSZ85] experiments from a numerical standpoint. They initiated the expansion phase with a pressurized gas bubble in the core region. And investigated the pressure transient, progression of the liquid front and deformation of the vessel wall.

Nakamura et al. [NKI+04b] devised an approach to assess the structural integrity of reactor vessels during a HCDA. Their work includes several experiments modeling an expansion phase as well as material tests and a numerical analysis of the structural response. The experimental setup consists of a water-filled tank at atmospheric pressure. The expansion phase is initiated by abruptly inserting compressed gas from below after breaking the rupture disc separating test vessel and gas reservoir. Test were conducted using a rigid and a deforming test vessel. They proposed a method to evaluate structural integrity of the vessel based on the maximum plastic strain occurring in the deformed vessel.

Liu et al. [LZL05] also developed a code to analyze fluid structure interaction during HCDAs. They use an ALE approach to represent the moving interface of both the expanding gas bubble and the deforming reactor vessel wall. The release of mechanical energy is modeled by a polytropic expansion with a constant exponent.

In 2010, Chellapandi et al. [CCR10] developed the computer code FUSTIN to analyze the mechanical response of the Indian Prototype Fast Breeder Reactor during the expansion phase. They used an ALE approach for the fluid dynamic equations to model the movement of the reactor vessel wall. The structural domain uses a *convective coordinate system* which refers to a Lagrangian formulation where rigid body motion and structural deformation are separated. The resulting deformation components are small which justifies the use of linear strain-displacement relation. Both, fluid and structural domain were treated using finite elements. The fluid domain contains both liquid and gaseous phases and the two-phase flow is treated with a volume of fluid approach.

All of the above mentioned codes reliably reproduce experimental results. Some include sophisticated structural material models and most of them ensure accurate interface tracking through an ALE formulation. But they all rely on polytropic gas expansion with a constant exponent for modeling the mechanical work release.

No code currently exists that models both fuel coolant interaction and fluid structure interaction at the same time. Since both phenomena are connected through the internal pressure and temperature of the coolant, they influence one another. A polytropic expansion with constant exponent cannot accurately represent the unstable phenomenon of fuel coolant interaction. Only a fully coupled approach can reliably predict the mechanical work release of a reactor during an actual, nuclear induced expansion phase.

The following chapter describes how I extend the severe accident code SIMMER with a structural model to simultaneously account for FSI and FCI. SIMMER-III has proven to be capable of analyzing FCI [MKTB99]. The newly developed structural model relies on the FEM approach and accounts for radial elasto-plastic deformation of the reactor vessel wall.

3 Methodology

To simultaneously analyze FSI and FCI during the expansion phase resulting from a code disruptive accident in a nuclear reactor, I developed an extended version of the severe accident code SIMMER-III. This chapter details the models, assumptions, and third-party resources used for the implementation. Since the fluid dynamic formulation is an essential part of a FSI code, I start with a brief description of SIMMER's fluid dynamics module although I only performed minor modifications. A detailed description of the Finite Element Method (FEM)-based structural code follows before discussing the coupling model and implementation.

3.1 Fluid Dynamics

SIMMER is a code originally designed to analyze the progression of severe accidents in metal cooled fast reactors after the initialization phase. Fluid dynamics and thermohydraulics play an important role in those accidents and are a vital aspect of a severe accident code.

During the transition phase, multi-phase flows occur. From boiling of the coolant to the melting and reallocation of fuel inside the reactor core, the impact of multi-phase flow behavior on the evolution of the accident are manifold. Vapor explosions, provoked by expulsion of hot liquid fuel into colder surrounding coolant are the drivers of the expansion phase that is the subject of this work.

As detailed in section 2.1.2 original SIMMER III code consists of three fundamental parts [YFT+03]. The fluid dynamic model, the structural model treating heat transfer and breakup of fuel pin and cladding, and the neutronics model providing the nuclear heating terms. Structural and fluid dynamic code interact through heat and mass transfer terms. Each SIMMER cell contains volume fractions of structural material, liquids and gases (vapor). The fluid dynamics model treats the fraction of the cell that is non-structural $(1 - \alpha_s)$.

By default, SIMMER possesses three distinct velocity fields for fluids. For numerical consistency (mass conservation and physical pressure behavior at phase change), both liquid and vapor state are treated in all cells. Even if there is virtually no vapor present in the cell. If the vapor volume fraction falls below a threshold value (α_0), SIMMER considers the cell to be single-phase.

3.1.1 Fundamental Equations

The fundamental equations of SIMMER's fluid dynamics model enforce the conservation of:

1. Mass
2. Momentum
3. Energy

The conservation of mass in a unit volume is given by:

$$\frac{\partial \bar{\rho}_m}{\partial t} + \nabla \cdot (\bar{\rho}_m \vec{v}_q) = -\Gamma_m \tag{3.1}$$

Where ρ is the density, the subscript m denotes the density components and $\vec{v}_q$ is the velocity vector of the q^{th} momentum component. Γ is the phase change rate per unit area.

The equation for the conservation of momentum is:

$$\begin{aligned}\frac{\partial \bar{\rho}_q \vec{v}_q}{\partial t} + \nabla \cdot (\bar{\rho}_q \vec{v}_q \vec{v}_q) + \alpha_q \nabla p - \bar{\rho}_q \vec{g} + K_{qS} \vec{v}_q \\ - \sum_{q'} K_{qq'} (\vec{v}_{q'} - \vec{v}_q) - VM_q = - \sum_{q'} \Gamma_{q'q} [H(\Gamma_{qq'}) \vec{v}_q + H(-\Gamma_{qq'}) \vec{v}_{q'}]\end{aligned} \tag{3.2}$$

Where subscript m denotes density components, and K is a factor describing the rate of momentum exchange between two components. The term $K_{qq'}(\vec{v}_{q'} - \vec{v}_q)$ describes the momentum exchange between two velocity fields q and q' and $K_{qS}\vec{v}_q$ the momentum exchange between velocity field q and the structure. H() is the heavyside function, and VM the virtual mass force term. A detailed description of the momentum exchange functions in SIMMER III is given in [Tob04].

And the equation for the conservation of energy:

$$\begin{aligned}&\frac{\partial \bar{\rho}_M e_M}{\partial t} + \sum_{m \in M} \nabla \cdot (\bar{\rho}_m e_m \vec{v}_q) + p \left[\frac{\partial \alpha_M}{\partial t} \nabla \cdot (\alpha_M \vec{v}_q) \right] \\ &- \frac{\bar{\rho}_M}{\bar{\rho}_m} \left[\sum_{q'} K_{q'q} (\vec{v}_q - \vec{v}_{q'}) \cdot (\vec{v}_q - \vec{v}_{q'q}) + K_{qS} \vec{v}_q \cdot (\vec{v}_q - \vec{v}_{qS}) - VM_q \cdot (\vec{v}_q - \vec{v}_{GL}) \right] \\ &= Q_N + Q_{MF}(\Gamma_M) + Q_{HT}(h, a, \Delta T)\end{aligned} \tag{3.3}$$

Here, α is the volume fraction, e the specific energy, and subscript M denotes the energy components. The source terms stem from nuclear heating (Q_N), melting / freezing processes (Q_{MF}) and heat transfer (Q_{HT}) which depends on the heat transfer coefficient denoted wih h and the binary-contact area per unit volume a.

Turbulence SIMMER III uses a simplistic turbulence model to account for momentum dissipation through turbulence [Tob04].

3.1.2 Multi-Step Fluid Solver

To cope with the complex fluid behavior including multiple phases, heat-and mass transfers and acoustic effects, SIMMER resorts to a 4- step solver algorithm. This results in a semi-implicit formulation.

- Step 1 handles intra-cell heat and mass transfers including phase changes
- Step 2 predicts the end-of timestep quantities in each cell, accounting for convection but neglecting intra-cell transfers.
- Step 3 computes the end-of timestep pressure.
- Step 4 adjusts all quantities to guarantee coherence with the pressure computed by step 3.

Step 1

Step 1 is the most complex part of SIMMER III's fluid dynamics algorithm. Here, we solve the conservation equations for mass and energy while neglecting the convective terms:

$$\frac{\partial \bar{\rho_m}}{\partial t} = -\Gamma_m$$

and

$$\frac{\partial \bar{\rho}_M e_M}{\partial t} = Q_N + Q_{MF}(\Gamma_{MF}) + Q_{VC}(\Gamma_{VC}) + Q_{HT}(h, a, \Delta T)$$

Where subscripts *MF* and *VC* denote *melting / freezing* and *vaporization / condensation* respectively. Q_N is the source term for nuclear heating obtained either from the neutronics model or prescribed through a time-dependent, user-defined function. Q_{HT} is the source term for heat transfer between energy component M and other components in the cell.

Step 1 also determines the momentum exchange functions for later use in steps 2, 3 and 4.

Step 2

Step 2 gives an estimation on the end-of-timestep field variables through time-explicit integration of the conservation equations. This time, source-terms are neglected during integration.

The distinct momentum conservation equations for each component are coupled through drag terms and solved as a linear matrix equation.

Step 2 also calculates the velocity derivatives with respect to the pressure ($\partial \vec{v}/\partial p$) for later use in step 3.

Step 3

Step 3 establishes consistency between cell pressure and cell-edge velocities. Also, EOS pressures are determined as a function of cell pressure. The six distinct residuals in SIMMER III's step 3 are:

- Difference between cell pressure and EOS pressure
- Density residuals for all four velocity fields
  - liquid fuel & particles
  - liquid steel
  - coolant
  - gas and vapor
- Vapor internal energy

With the velocity derivatives from step 2, we obtain a multivariate matrix equation. Which, when inverted, yields six equations. One for each residual. SIMMER solves the pressure equation first, substituting the new pressure into the remaining five equations.

Step 4

The fourth step performs the final update of all cell variables with pressure and velocities obtained from step 3. This yields the new volume fractions for liquid and gas phases as well as the new internal energies of all energy components.

The four-step, semi-implicit approach allows SIMMER to treat the complex multi-phase flow with inter- and intra-cell heat and mass transfer while preserving numerically stability. This approach was state-of-the art in the 1990's when SIMMER-III was developped. The method does not come without drawbacks, as presented out below.

Features and Limitations

The decoupling of intra-cell heat and mass transfers (step 1) from the fluid convection algorithm (steps 2 - 4) greatly simplifies the treatment of both highly nonlinear processes. This allows for an efficient treatment of multi-phase flow problems with phase changes as are typical in severe accident reactor analysis. The approach however is not without problems.

The decoupling introduces a time step sensitivity especially when mass-transfer from vaporization or condensation opposes fluid convection. Hence we need to restrict the minimum time step size to the order of 10^{-4} where vaporization or condensation processes prevail.

3.1.3 SIMMER's Mesh

Two SIMMER versions are used for production runs. One uses a 2-D, the other a 3-D formulation. I concentrated on the 2-D version (SIMMER S3V3F) since at the time of writing it is the more frequently used. For the sake of brevity, I will concentrate on the computational grid of the 2-D version.

SIMMER-III's fluid dynamics algorithm uses a 2-D staggered grid. Density, energy and pressure are defined at the cell center while velocities are defined at the cell edges.

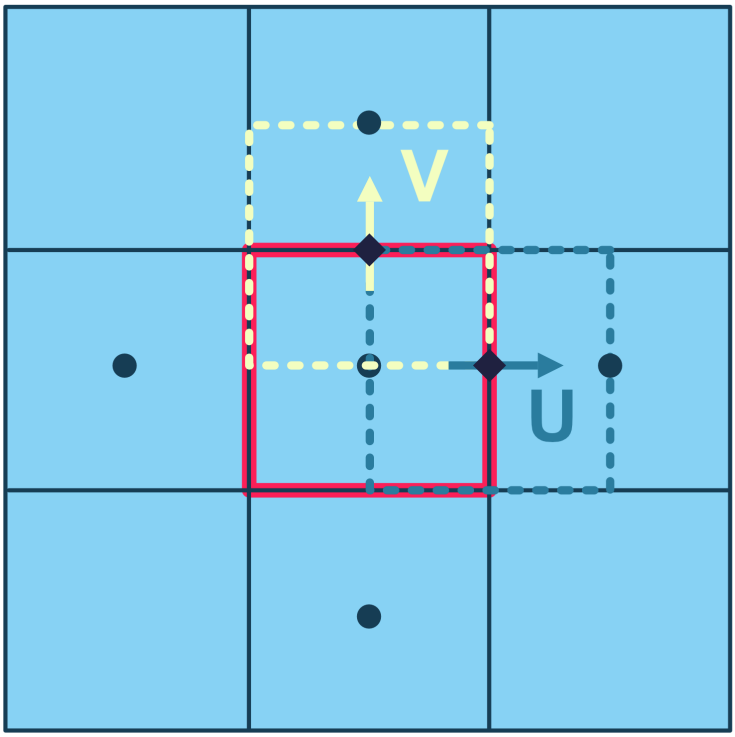

Figure 3.1: Staggered grid as used by SIMMER-III.

The grid is regular and defined through an input file. It is non-deformable. Two options for the coordinate system are available:

1. A cylindrical, rotationally symmetric coordinate system is the default and the two coordinates are radius and axial height.
2. A Cartesian coordinate system is also available allowing the analysis of rectangular reactor geometries.

3.1.4 Boundary Condition Treatment in SIMMER

SIMMER differentiates between two types of boundaries. *External* boundary conditions are applied in a cell-wise manner on the outermost cells of the computational domain. The user

can prescribe pressure, velocity and temperature individually at each boundary cell to either a constant value or a time-dependent function.

Internal boundary conditions, or: *virtual walls*, can be located inside the computational domain. They restrict fluid flow in normal direction and decouple cells on either side of the boundary thermally. The fluid dynamics algorithm treats virtual walls as free-slip boundaries. Virtual walls have no volume or mass assigned to them.

3.1.5 Material Properties and Equations of State

The SIMMER III code, which handles the fluid dynamics side of the problem, is capable of modeling a wide range of materials. The code features an EOS model that allows materials to change their aggregate state. Both, thermo-physical properties and the equations of state for the involved materials are defined over a large temperature and pressure range. To ensure the practicality of both models, they rely on empirical equations. Those empirical equations depend on three parameters only. A direct consequence of this, is that we trade precision for range. Meaning that while we can use the same equations for the entire temperature and pressure range, the results become worse the further we depart from the support points used to extract the three model parameters.

The moving wall now makes it more likely that we enter those poorly defined areas. To illustrate the problem, let us assume that a pressure wave has accelerated the vessel wall outwards. When, later, the pressure on the wall decreases, the inertia of the vessel wall will carry it on for some more time. On the fluid dynamics side, this increase in volume provokes a further drop in pressure. In some cases, the effect is so significant that the pressure drops below the atmospheric pressure. As a consequence, the material model can predict nonphysical material behavior in the near zero pressure range, causing the code to diverge in severe cases.

The problem mainly occurs for lower temperatures where close to the melting curve. Analysis with water at room temperature and atmospheric pressure as coolant for example, are a problematic setup.

I chose to limit the defined variable range to prevent the issue from corrupting the calculations. The mechanism to do so was already implemented in SIMMER. For water, I limited the calculated saturation pressure to 1000 Pa, well above the triple-point pressure of 612 Pa [WP02]. The temperature limit at 277 K also lies above the triple point temperature of 273.16 K. Figure 3.2 shows the phase diagram of water with the enforced limits.

Now, whenever the equations of state yield a temperature that lies below the limit, the defined minimum temperature is used instead of the calculated one. This is true for both liquid and vapor phase. The mechanism for the saturation pressure limit works similar to this.

Minimum Vapor Volume Fraction

SIMMER cells always carry a mixture of liquid coolant and coolant vapor. Even single-phase liquid cells, still hold a virtual amount of vapor. This is necessary to guarantee the stability of the EOS solver which cannot handle a 0.0% vapor volume fraction. This virtual amount of vapor in each cell makes a single-phase system less stiff. It reduces the speed of sound in the domain and increases compressibility. And this can work to our advantage. For numerical stability, a

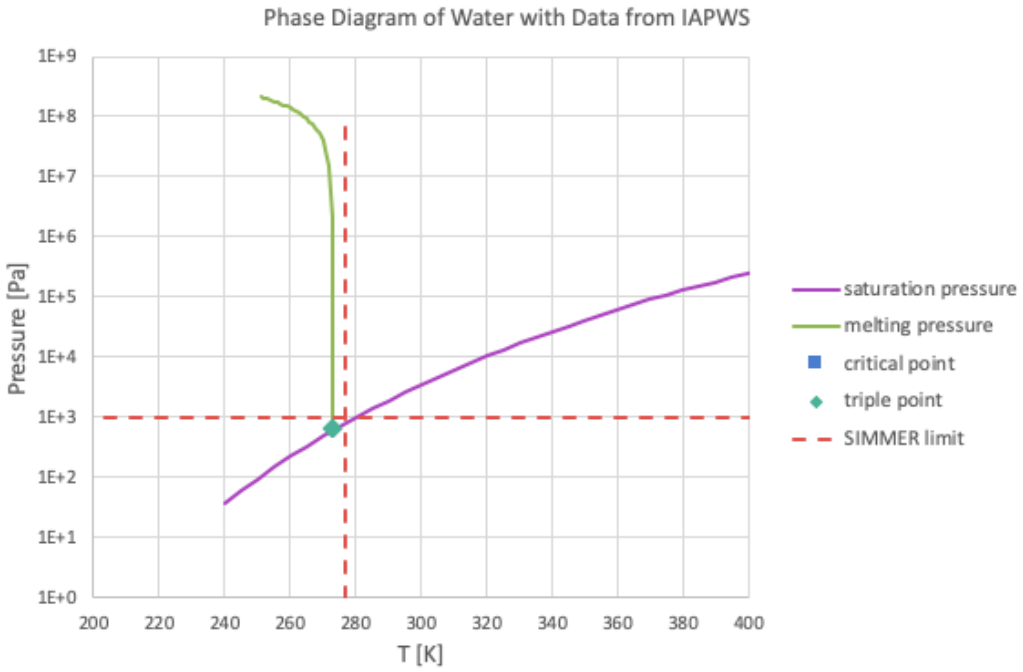

Figure 3.2: Phase diagram for water with imposed limits to ensure numerical stability of coupled SIMMER code.

less stiff system is beneficial. By adjusting the minimal vapor volume fraction in each cell, we can make the system behave more gentle and improve convergence.

For water at room temperature, I found that a minimum vapor volume fraction of 5% allowed the code to run stable without introducing a significant error The default value of SIMMER III lies at 1%.

For sodium cooled reactors at operation temperature, the minimum vapor volume fraction can remain at the default value.

This concludes the description of the fluid dynamics models and implementation. SIMMER uses a VOF- based approach to solve the energy, momentum and mass conservation equations for the multi-phase, multi-component flow problem. Its four-step semi-implicit solver relies on a finite volume approach on a staggered regular grid. To ensure numerical stability of the coupled code, modifications of the minimum vapor volume fraction, as well as minimum saturation temerature and -pressure are necessary. The following sections describe models and implementation for the structural dynamics solver and the coupling approach.

3.2 Structural Analysis

To account for wall deflection in a coupled FSI analysis first requires an method to determine the structural response at any time. State of the art approach for structural analysis is the finite element method in Lagrangian formulation. This section describes which framework and material models I use in this instance, and details their implementation. It mentions as well other, third-party tools, for meshing, partitioning and solvers.

3.2.1 Governing Equations

The fundamental equations describing the structural behavior follow from Newton's second law of motion:

$$\nabla \cdot \boldsymbol{\sigma} + \vec{P} = \rho \ddot{\vec{x}} \tag{3.4}$$

Where $\vec{P}$ is the external volumetric force, $\boldsymbol{\sigma}$ is the Cauchy stress and $\ddot{\vec{x}}$ the second time derivative of the position vector. ρ is the material density and ∇ is the differential operator $\left(\frac{\partial}{\partial x_1}, \frac{\partial}{\partial x_2}, \frac{\partial}{\partial x_3}\right)$.

Equation 3.4 describes the movement of structure in space and time; provided knowledge of the current stress state. To determine the stress state inside the structure requires a relationship between displacements stress. Commonly, the relationship is the combination of a stress-strain and a strain-displacement relationship.

The general form of the stress-strain relationship is:

$$\boldsymbol{\sigma} = \underline{\underline{\boldsymbol{C}}} : \boldsymbol{\epsilon} \tag{3.5}$$

Where $\boldsymbol{\epsilon}$ is the second order Cauchy strain tensor and $\underline{\underline{\boldsymbol{C}}}$ is the fourth order constitutive tensor. The : operator presents a double contraction and equation 3.5 in index notation equals $\sigma_{ij} = C_{ijkl}\epsilon_{kl}$.

The strain-displacement relation, as the name suggests, describes the strain as a function of the current displacements. In general form, adopting the nomenclature from [BRW75]:

$$\boldsymbol{\epsilon} = \underline{\boldsymbol{B}}\vec{u} \tag{3.6}$$

With $\vec{u}$ the vector of current displacements and $\underline{\boldsymbol{B}}$, in this case, a third order tensor. A vector notation for strain and stress is also frequently used, since both quantities are commonly symmetric. $\boldsymbol{B}$ then becomes the strain-displacement relation matrix.

Equations 3.4, 3.5, and 3.6 describe the behavior of a structural system. Together with boundary conditions, this translates to the following set of equations:

$$\begin{cases} \nabla \cdot \boldsymbol{\sigma}(\vec{u}) + \vec{f}^b = 0, & x \in \Omega \\ \vec{u} = 0, & x \in \Gamma^h \\ \boldsymbol{\sigma} \cdot \mathbf{n} = \mathbf{t}, & x \in \Gamma^s \end{cases} \tag{3.7}$$

Where $\vec{f^b}$ are the body forces, $\vec{n}$ is the unit normal vector, $\vec{t}$ is the traction vector on the surface, and Γ^h and Γ^s are the essential and natural boundaries respectively.

Finding a solution to equation 3.7 requires the application of numerical methods for all but the simplest of cases. The state of the art approach for structural analysis is the finite element method, which the following section discusses briefly.

3.2.2 The Finite Element Approach

The finite element method has been around since the sixties [AS69] , with precursors dating back to the fifties [Clo90], and has continuously gained importance with increasing computing power. FEM is today widely accepted as the go-to method for structural analysis. Numerous commercial, as well as open-source and proprietary implementations are available .

The fundamental idea behind the finite element approach is to solve the weak formulation of a partial differential equation.

The Weak Formulation

The weak formulation is the key concept of finite element methods. The concept makes use of the Galerkin Principle. The fundamental idea is to multiply the equation by a set of test functions and integrate over the relevant domain. If the equation holds true for all test functions (or in the case of FE a finite number of them) then the original equation is satisfied as well.

The multiplication and integration permits the application of Green's Identities and hence does simplify the solution space in the sense that the requirements for the functionals populating it are reduced.

Assume a set of vector valued *test functions*:

$$\vec{\phi} \in H_0^1(\Omega) \tag{3.8}$$

where H_0^1 is the Sobolev space containing at least once continuously differentiable compact functions in the domain Ω.

With this, the weak formulation of equation 3.7 is [MÖ18]:

$$< \vec{\phi}, \nabla \cdot \boldsymbol{\sigma}(\vec{u}) > + < \vec{\phi}, \vec{f^b} >= 0 \tag{3.9}$$

With $< ., . >$ the inner product operator.

This equals to:

$$\int_\Omega \vec{\phi}(\nabla \cdot \underline{\underline{\mathbf{C}}} : \boldsymbol{\epsilon}(\vec{u}))\ d\Omega + \int_\Omega \vec{\phi}\vec{f^b}\ d\Omega = 0 \tag{3.10}$$

A solution $\vec{u}$ for equation 3.10, that holds for all $\forall \phi \in H_0^1$, is also a solution for equation 3.7 [MÖ18].

The weak formulation is of interest for numerical applications because it can simplify numerical differentiation. Applying Green's first identity transforms equation 3.10 to [MÖ18]:

$$\int_\Omega - \left(\underline{\underline{\mathbf{C}}} : \boldsymbol{\epsilon}\right) \cdot \nabla \vec{\phi} \; d\Omega + \int_\Omega \vec{\phi} \vec{f^b} \; d\Omega = 0 \tag{3.11}$$

If, instead of all $\phi \in H_0^1(\Omega)$, we only use a subset of easily differentiable functions in Ω, the weak solution is still a good approximation of the original solution if the number of functions is sufficiently large.

This is the fundamental idea of the finite element approach and leads to the discrete form of equation 3.7 presented below.

Discrete Form of the Structural Fundamental Equations

The above section 3.2.2 describes how to derive the weak form of the governing equations from section 3.2.1. The Sobolev space $H_0^1(\Omega)$ however contains an infinite amount of functions and the numerical treatment of equation 3.11 is not easier than treatment of equation 3.7.

But if we chose an adequate finite subset of $\phi \in H_0^1(\Omega)$, the numerical differentiation becomes straight forward and equation 3.11 transforms to a system of equations:

$$\int_\Omega -\boldsymbol{\sigma}(\mathbf{u}(x)) \nabla \vec{\phi_i} \; d\Omega + \int_\Omega \vec{\phi_i} \vec{f^b} \; d\Omega = 0 \tag{3.12}$$

Now, $\boldsymbol{\sigma}$ and $\vec{u}$ are still defined on a continuous domain. We can discretize the displacements as well, ideally using the same subset of at least once differentiable compact *trial functions* on Ω as before. The approximation of the displacement field is then:

$$u(x) \approx \sum_{i=1}^{n} u_i \psi_i(x) \tag{3.13}$$

Where commonly $\psi = \phi$.

And with this, we derive the finite element formulation of 3.7:

$$\int_\Omega -\nabla \vec{\phi_i} \boldsymbol{A} \nabla \vec{\psi_i} \; d\Omega + \int_\Omega \vec{\phi_i} \vec{f^b} \; d\Omega = 0 \tag{3.14}$$

The stiffness matrix A relates the discrete displacement gradient to the discrete Cauchy stress tensor and depends on the trial and test functions employed, the general stress strain relationship and the strain-displacement relationship.

After determining the stiffness matrix A , one can solve the system of equations. In case A depends on the current solution vector u_i, a linearization step is required primarily. In this instance, the numerical library Portable, Extensible Toolkit for Scientific Computing (PETSc) [BAA+16] takes care of assembling the global stiffness matrix and the solving process.

3.2.3 Finite Element Implementation with PETSc

To solve the system of equations 3.14, requires the use of an iterative solver. The Newton-Raphson method is most commonly used, but a wide array of other numerical schemes is available.

I rely on an external numerical library to handle the solving process. This offers the possibility to chose from numerous iterative algorithms and test different combinations of pre-conditioners, time-stepping schemes, linear, and non-linear solvers. PETSc[BAA+16] also handles the assembly of the finite element stiffness matrix. It provides finite element- and dual-space instances to link geometry, mesh topology, and the fundamental equations.

To assemble the (non-) linear matrix equation, PETSc expects user provided, point wise residual functions. These are variations of equation 3.7, where the precise formulation depends on stress-strain and strain-displacement relation for the respective case (elastic vs. elasto-plastic etc.). The input for the point-wise residual functions has the form:

$$\int_{\Omega} \phi f_0(u, u_t, \nabla u, x, t) + \nabla\phi \cdot \vec{f_1}(u, u_t, \nabla u, x, t) \tag{3.15}$$

Where ϕ is the test function and $\nabla\phi$ the gradient of the test function. $f_0(u, u_t, \nabla u, x, t)$ and $\vec{f_1}(u, u_t, \nabla u, x, t)$ are the user provided functions for the integrands of the test function and the test function gradient term respectively.

The Krylov subspace methods also require an evaluation routine for the conjugate gradient and the user provides the appropriate Jacobian evaluation functions. Akin to the residual functions, the input for the point-wise Jacobian evaluation functions has the form:

$$\begin{aligned}&\int_{\Omega} \phi g_0(u, u_t, \nabla u, x, t)\psi + \phi\vec{g}_1(u, u_t, \nabla u, x, t)\nabla\psi \\ &+ \nabla\phi \cdot \vec{g}_2(u, u_t, \nabla u, x, t)\psi + \nabla\phi \cdot \overleftrightarrow{g}_3(u, u_t, \nabla u, x, t) \cdot \nabla\psi\end{aligned} \tag{3.16}$$

The first user-provided function g_0 is the integrand for the test function and the trial function term. It has the order 2. The next two functions, g_1 and g_2 have the order 3. g_1 is for the test function and trial function gradient term. And g_2 is for the test function gradient and trial function term. The last user-provided function, g_3, is for the test function gradient and trial function gradient term and has the order 4.

Boundary conditions, Neumann and Dirichlet, are handled separately in PETSc. With the Neumann conditions having an input interface similar to the residual input. The code enforces Dirichlet boundary conditions by removing the relevant degrees of freedom from the global system of equations and re-inserting the appropriate values after completion of the solve.

With PETSc handling global matrix assembly and solver routines, I provided the appropriate point-wise residual and Jacobian evaluation functions. Both change depending on the material model and infinitesimal vs finite strain formulation. The following sections go into detail on the respective formulations and mention the appropriate residual and Jacobian terms.

3.2.4 Linear Elastic, Infinitesimal Strain Formulation

The most basic case of material behavior is a linear elastic relationship between stress and strain state in a structure. Combined with the assumption of infinitesimal strains, this represents the elemental model for structural behavior. This section revisits the stress-strain and the strain-displacement relationships under the assumption of infinitesimal strain and linear elasticity.

Equation 3.6 under assumption of infinitesimal strains transforms to:

$$\boldsymbol{\epsilon} = \frac{1}{2}(\nabla \vec{u} + \nabla \vec{u}^T) \tag{3.17}$$

And with linear elastic material behavior, the fourth order constitutive tensor becomes [Kim15]:

$$\underline{\underline{\boldsymbol{C}}} = \lambda \mathbf{1} \otimes \mathbf{1} + 2\mu \underline{\underline{\boldsymbol{I}}} \tag{3.18}$$

$$C_{ijkl} = \lambda \delta_{ij}\delta_{kl} + \mu(\delta_{ik}\delta_{jl} + \delta_{il}\delta_{jk}) \tag{3.19}$$

With $\mathbf{1}$ the second order unit tensor, $\underline{\underline{\boldsymbol{I}}}$ the fourth order identity tensor and $\otimes$ the dyadic product. The kronecker delta function δ_{ij} is defined as:

$$\delta_{ij} = \begin{cases} 1 & i = j \\ 0 & i \neq j \end{cases}$$

λ and μ are the material specific Lamé parameters and related to Young's modulus E and Poisson ratio ν by:

$$\lambda = \frac{E\nu}{(1+\nu)(1-2\nu)} \tag{3.20}$$

$$\mu = \frac{E}{2(1+\nu)} \tag{3.21}$$

The point-wise residual evaluation functions for the linear elastic case with infinitesimal strains are, referring to equation 3.15:

$$\begin{aligned} f_{0[i]}(u, u_t, \nabla u, x, t) &= 0 \\ f_{1[ij]}(u, u_t, \nabla u, x, t) &= \mu\left(\nabla u_{ij} + \nabla u_{ji}\right) + \delta_{ij}\lambda \nabla u_{ii} \end{aligned} \tag{3.22}$$

And the Jacobian evaluation functions are:

$$\begin{aligned} g_{0[ij]}(u, u_t, \nabla u, x, t) &= 0 \\ g_{1[ijk]}(u, u_t, \nabla u, x, t) &= 0 \\ g_{2[ijk]}(u, u_t, \nabla u, x, t) &= 0 \\ g_{3[ijkl]}(u, u_t, \nabla u, x, t) &= \lambda \delta_{ij}\delta_{kl} + \mu(\delta_{ik}\delta_{jl} + \delta_{il}\delta_{jk}) \end{aligned} \tag{3.23}$$

The test function gradient and trial function gradient term g_3 is exactly the fourth order constitutive tensor given in equation 3.18

Together, 3.22 and 3.23 allow for an efficient solution of linear elastic, infinitesimal strain, 3-D structural problems in a finite element analysis. Examples and verification problems for the formulation are given in 4.1. The here following sections concern the special case of 2-D formulations as well as formulations for geometric- and material non-linearities.

3.2.5 Nonlinearities

When analyzing the expansion phase of a reactor, we can expect the vessel to plastically deform. This entails two non-linearities that we need to deal with. Firstly, the elasto-plastic behavior of the material for which we must chose an appropriate model. Secondly, large deformations forbid the linear approximation for the strain-displacement relation. To obtain reliable results, we must treat both non-linearities.

Geometric Nonlinearities

For small deformations, initial geometry and deformed geometry are virtually identical. For important quantities like the stress, we can reference the initial geometry. This stress measure is referred to as the Cauchy stress. The Cauchy stress describes the current load with respect to the initial geometry.

For very small deformations, this simplification is justified. But once deformations become larger, the Cauchy strain is no longer an adequate approximation of the current stress state inside the structure. We instead need to find another formulation for the stress that accounts for the change in geometry.

For the large deformation formulation of structural dynamics, I rely on the Lagrange strain tensor and the second Piola-Kirchhoff stress. Both refer the current stress- and strain state respectively to the original, undeformed geometry. The approach is known as the *total Lagrangian* formulation.

The total Lagrange strain tensor, accounting for the deformation of the geometry, is defined as:

$$\boldsymbol{E} = \frac{1}{2}\left(\boldsymbol{F}^T\boldsymbol{F} - \mathbf{1}\right) \tag{3.24}$$

Where $\boldsymbol{F}$ is the deformation gradient defined as $\boldsymbol{F} = \frac{\partial \vec{x}}{\partial \vec{X}}$ with $\vec{X}$ the undeformed and $\vec{x}$ the deformed vector.

The first Piola-Kirchhoff stress, referring forces in the current geometry to areas in the undeformed geometry, is defined as:

$$\boldsymbol{P} = J\boldsymbol{F}^{-1}\boldsymbol{\sigma} \tag{3.25}$$

Where $\boldsymbol{F}^{-1}$ is the inverse of the deformation gradient $\boldsymbol{F} = \mathbf{1} + \nabla_0 u$ and $J = \det \boldsymbol{F}$ the determinant of the deformation gradient tensor.

Since the first Piola-Kirchhoff stress is not a symmetric quantity, it is common to use the second Piola-Kirchhoff stress for the formulation of the equilibrium equation instead [Kim15]. To obtain it, we multiply 3.25 with the transposition of the deformation gradient's inverse:

$$\boldsymbol{S} = \boldsymbol{P}\boldsymbol{F}^{-T} = J\boldsymbol{F}^{-1}\boldsymbol{\sigma}\boldsymbol{F}^{-T} \tag{3.26}$$

Material Nonlinearities

Basic structural analyses assume a linear relation between strain and stress inside a structure. A load imposed to a structure causes a corresponding deformation that reverses the moment the load is lifted. For any stress state inside the structure, there is only one corresponding strain state and vice-versa. For most metals, this assumption is justified as long as the stress remains below the plastic limit.

In case the loads become higher, the material behavior changes. The structure now suffers irreversible, plastic deformation. Once the plastic limit is passed, the stress-strain relationship changes and so-called *hardening* occurs. For any stress state, there are now several possible strain states. And for every strain state of the structure, several stress states are possible depending prior deformations of the structure. The problem becomes history-dependent. Meaning that, for plasticity problems, all previous states of the structure have an impact on its current state.

To derive a model for plasticity that is practical to include in SIMMER, I rely on some simplifying assumptions summarized in the paragraph below.

Assumptions The treatment of elasto-plastic material behavior adds to the overall complexity of the problem. Depending on the model, the implementation requires solving additional nonlinear equations at each Gauss-point to determine the current stress state.

To keep required resources and numerical instabilities at bay, I rely on a set of simplifying assumptions for the elasto-plastic model.

To summarize, the assumptions for the elasto-plastic model are:

- Infinitesimally small strain
- Elastic and plastic parts of strain can be decomposed additively
- Constant temperature
- Plastic strain occurs only in deviatoric space $=> tr(\epsilon^p) = 0$

Some additional assumptions and models are necessary to describe elasto-plastic material behavior and to close the resulting structural equations. The following sections describe those additional equations and models briefly.

Flow criterion In a one dimensional stress state, it is relatively straight-forward to determine the exact loading point at which a material stops behaving elastically and enters the domain of plastic deformation. For multidimensional stress states, there is no such obvious elastic limit. We need some mapping from the stress tensor to a scalar quantity. We can then use this scalar to determine on which side of the elastic limit we are.

We define a yield function that compares the current stress state to a yield condition:

$$F(\underbrace{\sigma_{ij}}_{\text{current stresses}}, \underbrace{\kappa}_{\text{function of plastic strains}}) \leq 0 \tag{3.27}$$

If $F < 0$, the material behavior is elastic. $F = 0$ equates to plastic behavior. Per definition, F can never be positive, since the current stress state must always be either below, or exactly equal to the yield condition.

We now require a formulation for F, to map the multidimensional stress state to a scalar. The two most popular such mappings are called the *Tresca* and the *von Mises* flow criterion respectively.

Tresca's formulation seems to work best for brittle material like stone and concrete. It is used primarily in geodynamics and structural engineering of concrete structures. Due to it's minor importance for the elasto-plastic analysis of metal structures, the Tresca flow criterion is not further discussed here.

Von Mises' approach on the elastic limit on the other hand is the most commonly used flow criterion in elasto-plastic analysis of steel and metal structures. The *von Mises Stress* is defined as:

$$\sigma_{vM} = \sqrt{3\left(\frac{1}{6}\left[(\sigma_{11}-\sigma_{22})^2 + (\sigma_{22}-\sigma_{33})^2 + (\sigma_{33}-\sigma_{11})^2\right] + \sigma_{12}^2 + \sigma_{23}^2 + \sigma_{31}^2\right)} \tag{3.28}$$

Alternatively, the von Mises stress is equal to:

$$\sigma_{vM} = \sqrt{\frac{3}{2}\,\boldsymbol{s} : \boldsymbol{s}} \tag{3.29}$$

Where $\boldsymbol{s}$ is the deviatoric stress tensor defined as:

$$\boldsymbol{s} = \boldsymbol{\sigma} - \frac{1}{3} tr(\boldsymbol{\sigma}) \tag{3.30}$$

From this, we can derive the *von Mises yield criterion* in the plastic regime:

$$F = \sigma_{vM}^2 - \sigma_y^2 = 0 \tag{3.31}$$

Where σ_y is the *current* yield stress. With the norm $||\boldsymbol{s}||^2 = \sum_{i,j} s_{ij}^2$, and using equation 3.29, equation 3.31 can be rewritten to:

$$F = ||\boldsymbol{s}|| - \sqrt{\frac{2}{3}}\sigma_y = 0 \tag{3.32}$$

The von Mises yield criterion relies on the assumption that shear stress drives plasticity. Hydrostatic stress, no matter how significant, will never lead to plastic deformation according to its definition.

This leaves us with a criterion for when yielding occurs. To describe the material behavior after yielding, we need to define a hardening rule. This is the subject of the following section.

Hardening Rule The hardening rule describes the relation between plastic strain and its related stress. Essentially, the question is what happens to the elastic limit after it was once reached. If the limit increases, we speak of plastic hardening. If it stays the same, the material behavior is called elastic-perfectly plastic. And in case the elastic limit decreases after surpassed once, we call this plastic softening.

Typically, metals display some sort of hardening behavior after the plastic deformation sets in while other materials such as plastics and concrete may be prone to plastic softening. Both, plastic softening and perfectly plastic behavior are not relevant in the context of this work.

When considering strain hardening , the relation between plastic stress and increase in the elastic limit are rarely linear in reality. This means that remodeling the exact material behavior requires the solving of another nonlinear equation. To limit the computational effort, it is common to approximate the strain hardening behavior either with a multi-linear or a linear model. As a first step, I chose to use a simple linear hardening rule.

The linear hardening law states:

$$\sigma_y = \sigma_{y0} + K_{iso}\hat{\epsilon}_p \tag{3.33}$$

Where σ_{y0} is the initial yield stress, K_{iso} is the isotropic hardening parameter, and $\hat{\epsilon}_p$ is the equivalent plastic strain. Both, σ_{y0} and K_{iso}, are material specific parameters that are determined experimentally through tensile tests.

Associated Flow Rule The flow rule describes the evolution of the plastic strain in dependence of the stress state. It is often assumed, that the plastic strain increment has the same fundamental direction as the normal to the yield surface [Kim15]. This is then called an *associated flow rule*. The amount of the plastic strain increment is given through the plastic consistency parameter γ. Then, the plastic strain increment can be written as:

$$d\boldsymbol{\epsilon}^p = \gamma \frac{\partial F}{\partial \boldsymbol{\sigma}} = \gamma \frac{\boldsymbol{s}}{||\boldsymbol{s}||} = \gamma \boldsymbol{N} \tag{3.34}$$

Consistency Condition The yield criterion defines when the elastic limit is passed. And the hardening model describes how the elastic limit changes once the load on the material has passed it. Now, what is left to do is to deduct a rule that allows us to determine the stress state inside the structure for loads surpassing the current elastic limit.

The consistency condition states that, in case of plastic deformation during the current load step, the current stress state must lie on the current yield surface. For a hardening material, both stress state and yield surface change during plastic deformation and behave interdependent. The consistency condition writes as:

$$f = |\boldsymbol{\sigma}| - \sigma_y = 0 \tag{3.35}$$

We cannot directly identify the stress from the total displacement. The elasto-plastic stress-strain relation depends on the current stress tensor itself. This is why we have to rely on an internal solver to find the appropriate stress state on the yield surface.

Internal Solver To identify the appropriate stress state inside the structure, we have to rely on an internal solver. Assuming isotropic hardening only, and an associated flow rule we need to solve the following equation for the current plastic consistency parameter γ to determine the stress state:

$$f = ||\boldsymbol{s}^{trial}|| - 2\mu\gamma - \sqrt{\frac{2}{3}}\kappa(e_p) = 0 \tag{3.36}$$

In case of a linear hardening rule, γ is given directly as:

$$\gamma = \frac{||\boldsymbol{s}^{\boldsymbol{tr}}|| - \sqrt{\frac{2}{3}}\kappa(e_p)}{2\mu} \tag{3.37}$$

Where K_{iso} is the linear isotropic hardening factor.

Updating Stresses With γ now known, we can proceed to update plastic strain and current stresses:

$$^{n+1}\boldsymbol{\sigma} = \ ^{n}\boldsymbol{\sigma} + \Delta\boldsymbol{\sigma}$$

where:

$$\Delta\boldsymbol{\sigma} = \underline{\underline{\boldsymbol{C}}}_{elast} : \Delta\boldsymbol{\epsilon} - 2\mu\gamma\boldsymbol{N} \tag{3.38}$$

$$\boldsymbol{N} = \frac{\boldsymbol{s}^{trial}}{||\ \boldsymbol{s}^{trial}||} \tag{3.39}$$

in the case of isotropic hardening.

Consistent Tangent Operator An efficient numerical solver requires the preparation of a tangent stiffness operator. For linear elastic cases, the tangent stiffness operator equals the fourth order consistency tensor, as presented in section 3.2.4.

In case of elasto-plastic material behavior, the *algorithmic tangent stiffness tensor* differs from the *continuum tangent stiffness tensor* and depends on the numerical scheme employed [Kim15]. The elasto-plastic tangent stiffness tensor consistent with the numerical scheme employed is called the *consistent tangent operator*. Simo and Taylor [ST85] showed the importance of using such a consistent operator on the rate of convergence.

I use the consistent tangent stiffness operator for rate independent (multi-) linear isotropic plasticity as derived by [ST85]:

$$\underline{\underline{\boldsymbol{D}^{alg}}} = \frac{\partial \boldsymbol{\sigma}}{\partial \boldsymbol{\epsilon}} = \underline{\underline{\boldsymbol{C}}} - \frac{4\mu^2 \boldsymbol{N} \otimes \boldsymbol{N}}{2\mu + \frac{2}{3}K_{iso}} - \frac{4\mu^2\gamma}{||\boldsymbol{s}^{trial}||}[\underline{\underline{\boldsymbol{I}_{dev}}} - \boldsymbol{N} \otimes \boldsymbol{N}] \tag{3.40}$$

Where $\underline{\underline{\boldsymbol{I}_{dev}}}$ is the fourth order deviatoric identity tensor.

3.2.6 2-D Structural Formulation

SIMMER III is a 2-D code. It can handle both axisymmetric and Carthesian cases. To conserve resources, it makes sense to rely on a 2-D FEM formulation for the structural response as well.

The fundamental equations for the 2-D cases are the same as the ones for the 3-D case presented in section 3.2.1. The same principles of weak formulation and discretization as in sections 3.2.2 and 3.2.2 also apply. Depending the case, stress or strain do not vary in one particular, spatial direction. This allows to reduce the number of equations to solve per discrete point, and hence the degrees of freedom, from three to two.

I implemented three different 2-D formulations to use in the structural code. The *plane-stress* formulation is best suited for structures that have a small extend in one spatial direction. For structures with constant cross-sections but large extend in one spatial direction, the choice generally falls on the *plane-strain* formulation. Last, the *axisymmteric* formulation handles structures with constant cross-sections around an axis of revolution.

In some details, the 2-D implementations differ slightly from the general 3-D case. This concerns mainly changes in the constitutive relations to account for shear-stresses and shear-strains involving the third dimension.

This section presents the implementation of all three 2-D formulations with an emphasis on the axisymmetric case, which is the most relevant in the context of HCDA numerical analysis.

Axisymmetric 2-D Formulation

The most relevant structural model for the coupled case is the axisymmetric formulation. SIMMER III is a 2-D code and most reactor geometries are, primarily, cylindrical and not rectangular.

In an axisymmetric problem, two independent displacement variables suffice to describe the system. Those variables are radial and vertical displacement u and v respectively. This implies the use of a reduced cylindrical coordinate system $\{r, z\}$. The circumferential coordinate Θ is missing as the system does not vary in circumferential direction.

The strain-displacement relation for the axisymmetric case is (given in matrix-vector form for the sake of simplicity) [SGM14]:

$$\begin{Bmatrix} \epsilon_r \\ \epsilon_z \\ \gamma_{rz} \\ \epsilon_\Theta \end{Bmatrix} = \begin{bmatrix} \frac{\partial}{\partial r} & 0 \\ 0 & \frac{\partial}{\partial z} \\ \frac{\partial}{\partial z} & \frac{\partial}{\partial r} \\ \frac{1}{r} & 0 \end{bmatrix} \begin{Bmatrix} u \\ v \end{Bmatrix} \tag{3.41}$$

While the stress-strain relation in the linear elastic case is [Bat06]:

$$\mathbf{C} = \frac{E(1-\nu)}{(1+\nu)(1-2\nu)} \begin{bmatrix} 1 & \frac{\nu}{1-\nu} & 0 & \frac{\nu}{1-\nu} \\ \frac{\nu}{1-\nu} & 1 & 0 & \frac{\nu}{1-\nu} \\ 0 & 0 & \frac{1-2\nu}{2(1-\nu)} & 0 \\ \frac{\nu}{1-\nu} & \frac{\nu}{1-\nu} & 0 & 1 \end{bmatrix} \tag{3.42}$$

yielding the stress components

$$[\sigma_{rr}\ \sigma_{zz}\ \tau_{rz}\ \sigma_{\Theta\Theta}]$$

Remark how stress and strain tensor have three dimensions while the displacement vector only has dimension two.

Equilibrium Equations in the Axisymmetric Case In the axisymmetric case, the equilibrium equation in finite element formulation is the same as in equation 3.14 from section 3.2.2. This time, using a cylindrical coordinate system:

$$\iint_\Omega -\boldsymbol{\epsilon} : \underline{\underline{\boldsymbol{C}}}\boldsymbol{\epsilon}\ r\ dr\ \ dy + \int_\Omega \vec{v}_i \vec{f^b}\ r\ dr\ dz = 0 \tag{3.43}$$

The fundamental equations in the axisymmetric case are the same as for the general, 3-D case. But integration in cylindrical coordinates introduce an additional r. Stress-strain and strain-displacement relations are also slightly different. Deriving the point-wise residual and Jacobian evaluation functions now is straight forward.

This concludes the description of the axisymmetric formulation for the structural code. By assuming zero shear stress- and shear strain-components in circumferential direction, the necessary components of the displacement vector reduce from three to two. This cuts down the numerical effort significantly since an axisymmetric problem only requires a 2-D mesh. This decreases both local and global degrees of freedom simultaneously.

3.2.7 Meshing

For meshing, I use Christophe Geuzaine's gmsh [GR09]. It is one of the few open-source and easily available tools that offer the functionality I need for mesh generation. The mesh format can directly be input to PETSc and allows a seamless integration. Meshes can consist of simplex- (tetraherdon and tri) or vector product (hexahedron an quad) cells. A mix of both cell types is currently not accepted as it is not supported by PETSc. The user is responsible for creating an appropriate mesh and the code performs no sanity checks.

3.2.8 Material Parameters

The material model I use is rather straight forward. I rely on a rate-independent, isotropic strain hardening rule. The user has to carefully select the correct material parameters for the relevant temperature range and expected strain rates.

The structural material most commonly used in fast reactor applications is type 316 stainless steel with a low carbon content (316L[SRR^{+}13] or 316FR developed by JAEA specifically for fast reactor applications). As shown in figure 3.3 , the hardening behavior for 316 stainless steel changes significantly with temperature. Strain rate, especially at room temperature, is also an important factor in determining the correct hardening parameters for a given analysis setup.

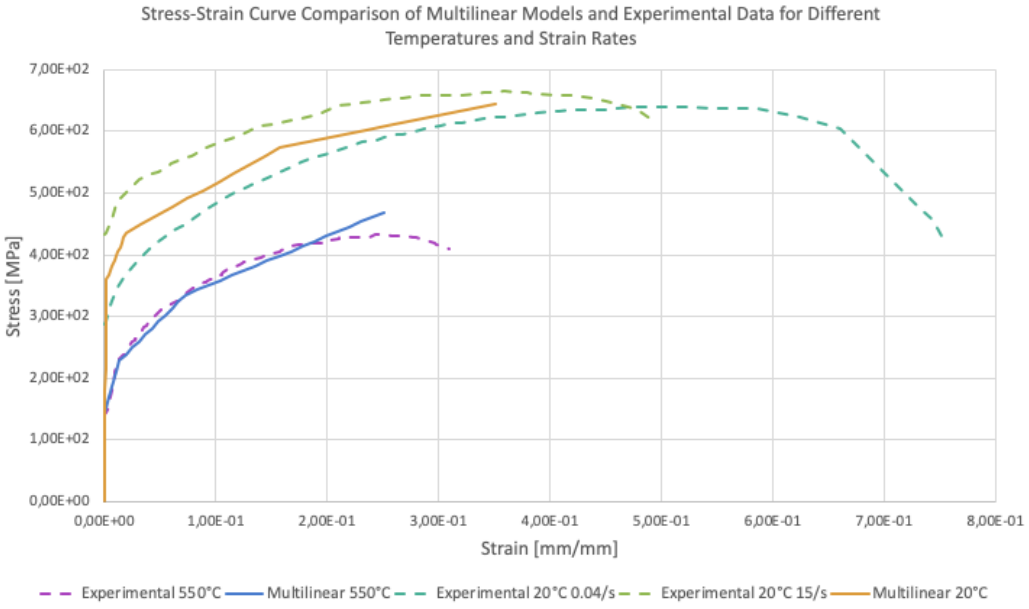

Figure 3.3: Comparison of 316L tensile behavior for different temperatures and strain rates with resulting multi-linear hardening curves.

In this work, I use two different material models for stainless steel at 20°C and 550°C respectively. Since experiments that can serve as validation and verification cases are often conducted at room temperature, it makes sense to have a corresponding material model.

While hardening behavior and elastic limit change with temperature, the material behavior in the elastic regime remains unchanged. Table 3.1 shows the elastic material parameters for 316 type stainless steel.

High Temperature Material Model

The operation temperature of sodium cooled fast reactors typically lies between 400°C and 600°C [Int07]. The material model assumes that during the HCDA, the vessel temperature does not rise significantly from initiating event to the impacto of the sodium slug. In case of a slow rise of temperature in the reactor over an extended period of time, the user should update the material

Table 3.1: Elastic parameters for 316 type stainless steel.

Quantity	Symbol	Unit	Value
Young's Modulus	E	GPa	198
Poisson ratio	ν		0.28
Lamé's first parameter	λ	GPa	91
Bulk Modulus	μ	GPa	78

parameters by hand prior to the coupled analysis. Yield stress and hardening parameters can be derived from tensile tests or dedicated material models given in [AM80], [OAKKI98], [Bri01] and [DB06].

For a pool type reactor, temperatures during operation are around 400°C for the vessel wall and 470°C in average for the core structure [FV11]. Tensile test data are available for 316L at 550°C [AM80] for different strain rates. Nakamura et. al [NKI+04b] provide a multi-linear stress-strain curve for 316FR at 450°C with a strain rate of 0.001/s.

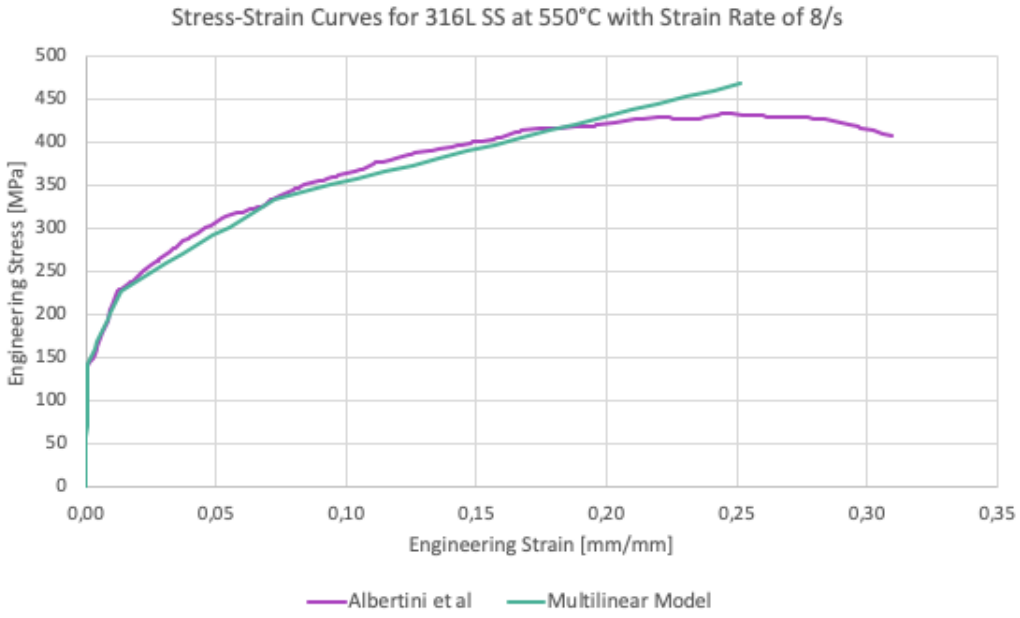

Figure 3.4: Stress-strain curves for 316L at 550° with a strain rate of 8/s. Multi-linear isotropic hardening model compared to experimental data from [AM80].

For the high temperature material model I chose to rely on data from Albertini et. al[AM80] since they provide data for the relevant strain rates. I adapted a multi-linear isotropic strain hardening model to fit the experimental stress-strain curve for uniradiated 316L steel at 550°C with a strain rate of 8/s. Figure 3.4 shows the comparison between experimental data[AM80] and the multi-linear model. Table 3.2 gives the relevant material parameters for the high temperature material model.

Table 3.2: Material parameters for the high temperature multi-linear isotropic hardening model.

Variable	Symbol	Range	Quantity
Yield Stress	σ_{y0} $[MPa]$	-	144
First Plastic Modulus	$K_{iso}^{(1)}$ $[GPa]$	$0\% < \hat{\epsilon}_p \leq 1.21\%$	6.914
Second Plastic Modulus	$K_{iso}^{(2)}$ $[GPa]$	$1.21\% < \hat{\epsilon}_p \leq 7.11\%$	1.814
Third Plastic Modulus	$K_{iso}^{(3)}$ $[GPa]$	$7.11\% < \hat{\epsilon}_p$	0.754

Low Temperature Material Model

While for analysis of expansion phases in SFRs, the relevant temperature range lies between 400°C and 550°C, experiments that serve as validation cases are often conducted at room temperature. I hence created a second, low temperature material model following the same approach as before in the high temperature case. Since no stress-strain curve were available for the relevant strain rate of 8/s, I interpolated the values from 0.04/s and 15/s data respectively.

Table 3.3 shows the resulting material parameters for the low temperature material model.

Table 3.3: Material parameters for the low temperature multi-linear isotropic hardening model.

Variable	Symbol	Range	Quantity
Yield Stress	σ_{y0} $[MPa]$	-	360
First Plastic Modulus	$K_{iso}^{(1)}$ $[GPa]$	$0\% < \hat{\epsilon}_p \leq 1.71\%$	4.381
Second Plastic Modulus	$K_{iso}^{(2)}$ $[GPa]$	$1.71\% < \hat{\epsilon}_p \leq 15.5\%$	1.013
Third Plastic Modulus	$K_{iso}^{(3)}$ $[GPa]$	$15.5\% < \hat{\epsilon}_p$	0.358

3.2.9 Limits of the Material Model

Especially at elevated temperatures, material creep can be an issue in reactor applications. The current material model neglects this phenomenon as the focus of this work lies on expansion phase scenarios. Time-scales for expansion phase and creep fatigue are orders of magnitudes apart.

Another commonly encountered phenomenon in reactors is the embrittlement of structural members by neutron impact. This phenomenon is also neglected in the material model. To account for neutron hardening, the user should adapt the material parameters prior to the analysis relying on empirical models or other sources such as [FH73].

3.2.10 Numerical Solver

To predict the structural behavior requires iteratively solving the fundamental equations 3.7. For solvers, matrix assembly and preconditioners, I rely on the PETSc [BAA+16] library. This section briefly describes the combination of solvers I used in the context of this work. The user can, however, chose from a large selection of available solvers and preconditioners to optimize convergence and stability.

Time Stepping

In non-linear structural dynamics, the initial value problem we are looking to solve has the semi-discrete form:

$$\mathbf{M}\ddot{\vec{u}}(t) + \mathbf{D}\dot{\vec{u}}(t) + \mathbf{A}(\vec{u})\vec{u}(t) = \vec{F}(t) \tag{3.44}$$

where $\vec{u}$ is the vector of displacements and F the vector of external forces. $\mathbf{M}$ and $\mathbf{D}$ are the constant mass and dampening matrix respectively. $\mathbf{A}$ is the stiffness matrix representing the nonlinear function relating displacements and internal forces. In our case, since I neglect structural dampening, $\mathbf{D} = 0$.

To solve equation 3.44 numerically, we need to determine time derivatives which requires a discretization of the time domain. Let t_i be in $[t_0, t_{fin}]$ where $t_0 < t_1 < t_2 < ... < t_{fin}$ and $\Delta t_i = t_{i+1} - t_i$.

I chose the generalized alpha method as time integration and -differentiation scheme. The method is generally suited for structural nonlinear problems. It guarantees second order accuracy for displacements and velocities, and first order accuracy for accelerations independently of the employed quadrature rule [EBB+02]. Depending on the method parameters, we can even achieve second order accuracy for the accelerations.

With the generalized alpha method, equation 3.44 transforms to [EBB+02]:

$$\mathbf{A}_{i+1-\widetilde{\alpha}_f}\vec{u}_{i+1} - \vec{F}_{i+1-\widetilde{\alpha}_f} \tag{3.45}$$

$$-\mathbf{M}\left[-\frac{1-\widetilde{\alpha}_m}{\widetilde{\beta}\Delta t^2}\left(\vec{u}_{i+1} - \mathbf{u}_i\right) + \frac{1-\widetilde{\alpha}_m}{\widetilde{\beta}\Delta t}\vec{v}_i + \frac{1-\widetilde{\alpha}_m - 2\widetilde{\beta}}{2\widetilde{\beta}}\vec{a}_i\right] = 0 \tag{3.46}$$

where $\vec{v}_i$ and $\vec{a}_i$ are the velocities and accelerations from the last time step respectively. After $\vec{u}_{i+1}$ is found, we can determine $\vec{v}_{i+1}$ and $\vec{a}_{i+1}$ for the next time step as:

$$\vec{a}_{i+1} = \frac{\vec{u}_{i+1} - (\vec{u}_i + \Delta t\vec{v}_i + (\frac{1}{2} - \widetilde{\beta})\delta t^2\vec{a}_i)}{\widetilde{\beta}\Delta t^2}$$

$$\vec{v}_{i+1} = \vec{v}_i + (1-\widetilde{\gamma})\Delta t\vec{a}_i + \widetilde{\gamma}\Delta t\vec{a}_{i+1}$$

$\{\widetilde{\alpha}_f, \widetilde{\alpha}_m, \widetilde{\beta}, \widetilde{\gamma}\}$ are parameters of the generalized alpha method and all lie within $[0, 1]$. For $\widetilde{\alpha}_m = \widetilde{\alpha}_f$, the acceleration computed with the generalized alpha method is second order accurate [EBB+02].

To solve the equation linearized in time requires a nonlinear iterative solver. The following section briefly describes the respective implementation used in this work.

Nonlinear Solver

To solve equation 3.45 requires the use of an iterative solver. I chose to use a Newton-Raphson method where the step size is determined with help of a line-search with cubic backtracking [DS96]. The method solves a system of nonlinear equations of the form:

$$\vec{F}(\vec{u}) = 0 \tag{3.47}$$

At each iteration step, the solution vector is updated according to:

$$\vec{u}_{k+1} = \vec{u}_k + \eta \Delta \vec{u}_k \tag{3.48}$$

Where η is a factor determined through the linesearch method, and $\Delta\vec{u}_k$ the k^{th} increment of the solution vector determined though:

$$\boldsymbol{J}(\vec{u}_k)\Delta\vec{u}_k = \vec{F}(\vec{u}_k) \tag{3.49}$$

Where $\boldsymbol{J}(\vec{u}_k)$ is the Jacobian ($\frac{\partial \vec{F}}{\partial \vec{u}}$), or consistent tangent stiffness matrix.

Determining the step direction ($\Delta\vec{u}_k$) requires solving equation 3.49 with the help of a linear solver.

Linear Solver

As a linear solver, I use the Generalized Mean RESidual (GMRES) method as developed by Saad [SS86]. The method is part of the Krylov subspace solvers implemented in PETSc.

3.2.11 Implementation

In summary, I use a finite element method with second degree test- and trial functions. The code is capable of both 3D and 2D structural analysis. It can handle elasto-plastic material behavior and geometric non-linearities resulting from large deformations. I rely on PETSc [BAA+16] for nonlinear solvers and preconditioners. As well as for parallel mesh handling and mesh partitioning (via an interface to PARMETIS [SKK02]). The solver is fully implicit and using a second order time integration scheme.

3.3 Coupling

The extended SIMMER code uses a partitioned approach for the analysis of FSI. Fluid and structural domain are treated with separate solvers and interaction between both domains is modeled through the exchange of coupling variables.

Section 3.1 established the fundamental equations and solver implementation for the fluid domain. Section 3.2 did the same for the structural domain. This section describes the coupling scheme, coupling variables and implementation in the extended SIMMER code.

I represent the moving boundary in SIMMER with a VOF approach. This allows to use the existing codebase and limits modifications to a minimum, since SIMMER provides its own integrated VOF model.

3.3.1 Determining the Obstructed Volume Fraction

I use a modifiable volume fraction that obstructs part of the cell and prevents radial movement of fluid to model the movement of the fluid / solid boundary in affected SIMMER cells. Every time the structure moves, the code recomputes and reapplies the new adequate volume fractions. An important aspect of this approach is to reliably determine the adequate volume fraction for the obstructive material. While the SIMMER mesh is always two-dimensional, the structural grid can be both two- and three-dimensional. To compute the correct volume fractions, I follow these steps:

1. Resolve the interface shape and location relative to the SIMMER mesh
2. Determine the orientation of the fluid / solid interface
3. Identify cells that are partly or entirely obstructed by structure
4. Interpolate missing vertices if necessary
5. Compute the volume occupied by the structure inside each affected cell

Resolving Interface Shape and Position

The first step to determine the adequate obstructed volume fractions is to determine the current location and shape of the fluid / solid interface relative to the SIMMER mesh.

The structural mesh has labeled boundaries. This makes identifying the interface vertices on the structural grid easier. After referencing them by their assigned label name, I compute their current position by adding the current solution (displacements at time t) to the initial vertex position. This leaves me with a subset of vertices and their current position in space.

In case of a three-dimensional structural mesh, I take the additional step of projecting the interface from 3D to 2D space. I do this by transforming into cylindrical coordinates and neglecting the angular coordinate.

The collection of boundary vertices forms an unordered set. Connectivity information is available in the original mesh, but it is not preserved during the projection.

Identifying Interface Orientation

To calculate the volume obstructed by structure requires information on interface geometry and orientation. Step 1 yields the interface location at discrete points. But detailed information on the shape and orientation of the interface is not available. To determine the orientation of the interface and differentiate between fluid and non-fluid domain, I rely on the following assumptions:

1. The primary orientation of the interface is vertical
2. The interface does not self-intersect
3. No fluid occurs in increasing radial direction behind the interface

The discrete locations of the interface and the above mentioned assumptions provide enough information to determine the interface orientation and distinguish between fluid and non-fluid domain.

Identifying Affected Cells

The next step is to identify the cells that require adjustment of their obstructed volume fraction. To do this, I iterate through all vertices in the fluid / solid interface and overlay their position with the SIMMER mesh. Whenever a vertex falls inside a SIMMER cell, I mark this cell as a boundary cell. I then rely on the assumption that everything behind the interface (where $r > r_{interface}$) is obstructed volume. It follows that all SIMMER cells in increasing radial direction behind the boundary cell must be completely obstructed even though they contain no boundary vertices.

Interpolating Boundary Vertices

When the structures are large, like in the case of a vessel wall, the solid mesh can become relatively coarse with respect to the SIMMER mesh. In that case it can be problematic to track the interface and compute the correct obstructed volume fractions. This is especially problematic when using regular structural 3D grids.

In case of irregular meshes, the projection onto the two-dimensional domain generally increases the vertex density in vertical direction. For regular meshes on the other hand, all projections fall onto the same vertical coordinate. Two types of problems can occur.

The first problem is that cells that should contain fluid / solid interface vertices do not. This happens when the structural grid in a region is coarser in one dimension than the SIMMER mesh. This causes gaps in the interface. And what should be one single structural entity is now represented as a collection of structural components in SIMMER.

The second problem concerns precision. I use a three-point Gauss integration to compute the adequate volume fraction in each boundary cell. If a cell contains less than three vertices or the vertices are too far from the Gauss points, the result can become inaccurate.

The remedy for both problems is to increase the number of vertices. Since the primary orientation of the boundary is vertical, this usually means increasing the mesh density in z-direction. And there are two way to achieve this.

The first, most obvious way is to refine the structural grid. Not only does this improve the precision of the obstructed volume but also that of the structural analysis itself. The downside of this method is that it increases the complexity of the structural analysis and therefore consumes more resources.

The second way is to introduce additional vertices after the structural analysis has already been run. After the projection, interpolating the boundary position is a one dimensional problem. In its current form, the code uses a straight forward approach. Assuming a primarily vertical orientation of the boundary, I chose z as independent, and r as dependent variable. Then, I discretize the space between z_{max} and z_{min} of the original grid with the needed interval size. And finally I linearly interpolate the r-positions at the new z-positions between the old points.

This approach can prove problematic where the primary orientation of the interface is not horizontal. In this case, the solution would be to create a second, finer 3D mesh. We can then project a field onto it from the coarser grid. PETSc comes with most of the required functionality to implement this. But for the sake of simplicity I did not yet implement this in the code. The advantage would be that geometric information is preserved. But at the cost of additional computational effort.

Compute the Volume Occupied by the Structure

After identifying the boundary cells and having determined the orientation and discrete positions of the fluid / solid interface inside those cells, the next step is to compute the non-fluid volume inside each affected cell. I do this with the help of a two point numerical Gauss integration. Figure 3.5 illustrates the setup.

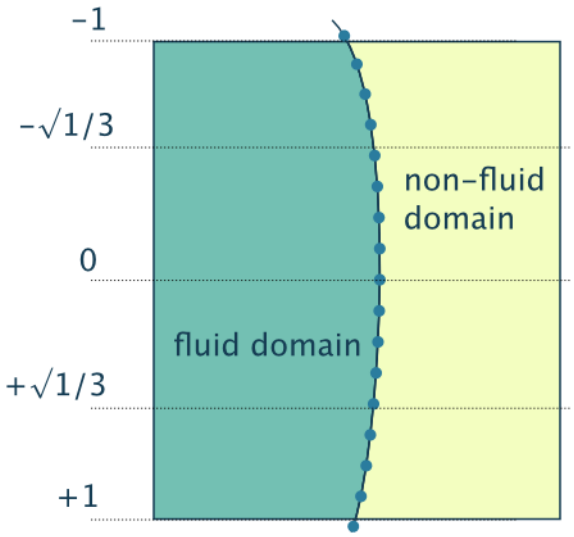

Figure 3.5: Fluid / solid interface cell with interface vertices and Gauss point locations.

First, I determine the two vertices closest to the gauss points at $\pm\sqrt{1/3}$ of the cell height and their radial position. The non-fluid volume is then given by:

$$V_{nf} = V_{cell} - h_{cell}\frac{1}{2}\pi\left((r_I^2 - r_0^2) + (r_{II}^2 - r_0^2)\right) \tag{3.50}$$

Where r_I and r_{II} are the radii of the first and second gauss point respectively, r_0 is the radius of the innermost cell boundary, and h_{cell} the height of the cell.

The obstructed volume fraction is then simply given by:

$$\alpha_{nf} = \frac{V_{nf}}{V_{cell}} \tag{3.51}$$

In case the cell is located entirely in the non-fluid domain, no interface vertices are present and the obstructed volume fraction is equal to 1.

3.3.2 Representing the Boundary in SIMMER's Fluid Dynamics Algorithm

SIMMER follows a volume of fluid approach to represent different materials in the computational domain. The code discriminates between 3 different aggregate conditions. Both gaseous and liquid phases have velocity fields associated with them. Meanwhile, structural components are fixed in place and do not follow any laws of motion.

Figure 3.6 shows the set-up of a generic SIMMER computational cell. Before meltup, the fuel is contained inside the pin, which is surrounded by the cladding. Each cell potentially also has a canwall in it. I case a right or left canwall is present in a cell, fluid flow across the right / left edge of the cell respectively is prevented. In real reactors, we find a small gap in between canwalls that allows easy removal and insertion of subassemblies. Inside this gap, no fluid motion generally occurs. SIMMER models these gaps by introducing a no flow area associated with the right or left canwall. This no flow area has no mass or material assigned to it.

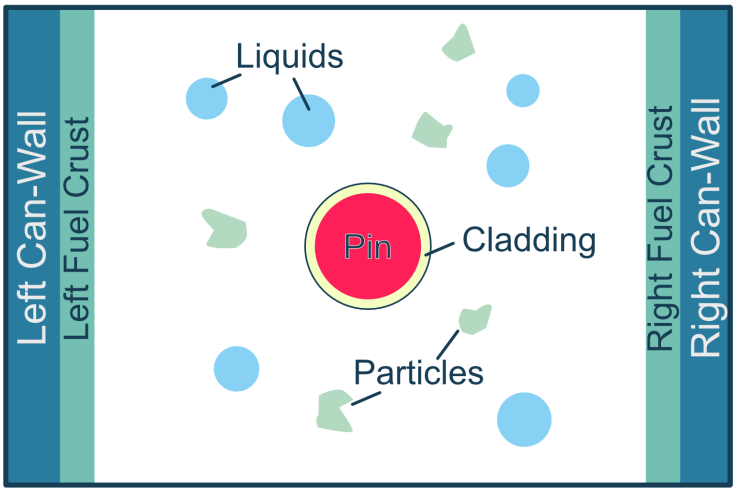

Figure 3.6: Exemple of a SIMMER cell with structural, fluid and gaseous components.

Inside the fluid / solid boundary cells, we do not want to permit fluid movement in normal direction of the boundary orientation. This is, of course, assuming that the submerged structure is lager than computational cell. In case of the reactor vessel wall, the orientation of the fluid / solid boundary is primarily vertical as previously established. Since it effectively bounds the computational domain, it always restricts fluid flow rightwards in any affected cell. This makes the right canwall an ideal candidate for representing the reactor vessel wall inside boundary SIMMER cells.

The problem is, that there is no mechanism in place to move right canwall material into and out of a cell without breaking up the structure. A disintegrated right canwall would no longer

restrict fluid flow. I therefore manipulate the volume fraction by prescribing it a new value each time step.

I chose to use the right canwall no flow area volume to represent the moving reactor vessel wall in SIMMER. By modifying the volume fraction of this obstructive material, I can mirror the advancing or retreating boundary across the cell. If the boundary accelerates inwards, I increase the volume fraction. If the boundary falls back outwards, I reduce it. And since no material is assigned to the no flow area, mass conservation is preserved.

Whenever the boundary moves inward, the increased no flow area volume leads to an *overfilling* of the cell. Since the overall volume of the cell remains constant, this causes a compression of compressible material inside the cell. The resulting increased pressure drives out fluid from the cell. In case of an outward moving vessel wall, the opposite effect causes an inflow of fluid from the surrounding cells.

The modification of the no-flow area volume fraction takes place between step 1 and 2 of the fluid dynamic solver. As a reminder, SIMMER's fluid-dynamics solver consists of:

- Step 1: Intra-cell heat and mass transfers.
- Step 2: Estimation of the end-of-timestep variables.
- Step 3: End-of-timestep velocities and pressures.
- Step 4: Consistent energy, mass and momentum convection.

The source term calculations in step 1 rely on the pressure and internal energy state determined by step 3 and 4 of the previous time step. Changing the volume fractions just after step 1 allows for step 2 to make accurate predictions regarding the end-of-timestep variables.

In this section, I detail the approach for representing a moving boundary in SIMMER. I established a method to determine the volume that is obstructed by non-fluid material, as well as a procedure to identify interface cells and enforce the newly determined volume fractions in them. The first coupling variable, the obstructed volume fractions for each SIMMER cell, results from the displacement of the fluid/solid interface determined in the structural analysis. The following section presents the approach for determining the second coupling variable, the flow-induced load on the structure.

3.3.3 Load on the Structure

Structural components inside the reactor as well as the vessel wall experience a load exerted on them by the contained fluid. Moving fluids can exert force in the form of (dynamic) pressure in normal direction and skin friction in tangential direction. The forces on the fluid/solid interface result from the fluid dynamics solve and serve as Neumann boundary condition during the structural solve.

In this work, the focus lies on the structural response of the reactor vessel during the expansion phase. Skin friction inside the densely packed core region and around the upper internal structures plays a big role in slowing down the accelerated slug and reducing its kinetic energy. Outside the core region, to determine the load on the vessel wall during the expansion phase, skin friction is a negligible effect.

For the force coupling between structural and fluid domain, I solely consider pressure loading on the structure. Determining the space- and time dependent load is a straight forward procedure. For each vertex on the structural side of the fluid/solid interface, I identify the corresponding

SIMMER cell. Then I extract the appropriate cell pressure from the most recent converged SIMMER time step and apply it to the surface as a Neumann boundary condition.

After now having established the necessary coupling variables for both domains, the next section describes the coupling scheme between both solvers.

3.3.4 Code Communication

The preceding sections established the method for deriving the coupling variables and applying them as boundary conditions in the respective other domain to achieve coupling between structural and fluid dynamics analysis. This section describes a protocol for where, how often and in which form both codes exchange information.

I coupled both codes loosely, resulting in a single solver call per time step and domain. This type of coupling is more sensitive to time step size than *tightly coupled* codes which ensure consistency between both domains by solving fluid and structural domain multiple times each time step with updated loads and boundary positions. In the unmodified SIMMER, time step size during the expansion phase typically lies in the order of 1E-4 s. I hence do not expect the coupling method to be the limiting factor for time step size. The advantage is that computational time per step is much lower thanks to less solver calls. And the implementation is much more straight forward and avoids significant modifications of the SIMMER code base.

To advance to the next time step, the structural solver needs information on the current load configuration and the size of the current time step. As discussed previously, the load obtained from the pressure acting on the surface. I transfer the current pressure field from the SIMMER code to the structural analysis prior to starting the structural solve. Since SIMMER dynamically adapts its time step size, I also transfer this information to guarantee the synchronous advancing of both codes.

The SIMMER code receives the updated volume fractions of no-flow area volume from the structural analysis. This information is sufficient to adequately represent the current position of the fluid / solid boundary and is exchanged every time step. Figure 3.7 illustrates the sequential call of fluid dynamic and structural solver, and the exchange of coupling variables.

Prior to starting the solve, the structural code needs information on the mesh configuration of the SIMMER analysis. First, to determine the load along the immersed boundary by choosing the correct cell pressure for each boundary section. And second, to compute the adequate volume fractions for SIMMER boundary cells. The structural code obtains this information in the same way the SIMMER code does by reading the *sim05* input file.

In this chapter, I detail the models and numerical methods used to analyze both the fluid dynamic and structural problem. Then, I present the method I use to couple both domains, allowing the analysis of coupled fluid structure interaction problems. The next chapter describes the validation and verification efforts for the newly developed coupled code.

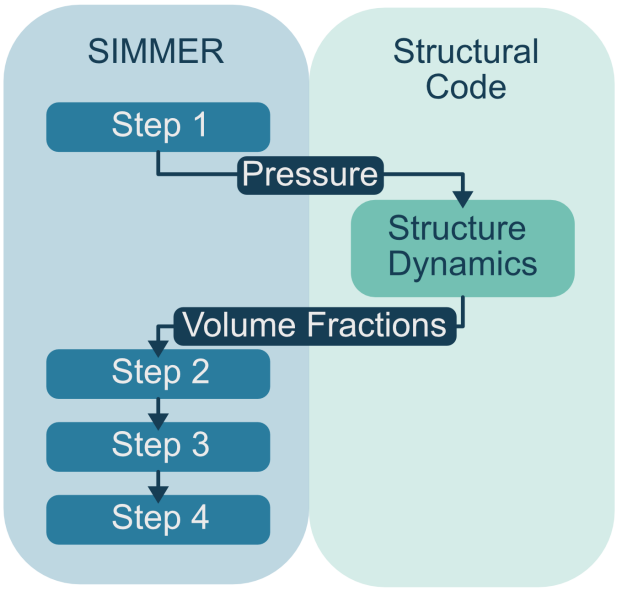

Figure 3.7: Schematic representation of the coupling between structural and fluid dynamic code with calling sequence and coupling variables.

4 Validation and Verification

After establishing a method to analyze coupled FSI problems with SIMMER in the previous chapter, this chapter illustrates the fitness of the resulting implementation for the analysis of expansion phases in sodium cooled fast reactors. The first stage consists of verifying that the coupled code provides results that are consistent with the models employed. The second stage checks if those models are adapt for modeling EP in SFRs.

The terms validation and verification are sometimes used interchangeably. In this work, I use the terminology as introduced in [OTH04] where *verification* describes the process of ensuring consistency between the original model and the numerical implementation, and *validation* refers to ensuring the adequacy of the chosen approach to the problem at hand.

4.1 Verification

For verification of the code, I compared results of both coupled and standalone structural analysis to analytical solutions for known reference problems. The reference problems consist of:

- Bending beam (static linear elastic)
- Inflating Cylinder (static linear elastic)
- Tensile probe (elasto-plastic)
- Water hammer in one dimension (coupled dynamic linear elastic)

4.1.1 Bending Beam Problem

The bending beam problem is a well studied and extensively described problem of continuum mechanics. Analytical solutions are available for a multitude of problem configurations and both 2-D and 3-D versions of the finite element code can be compared.

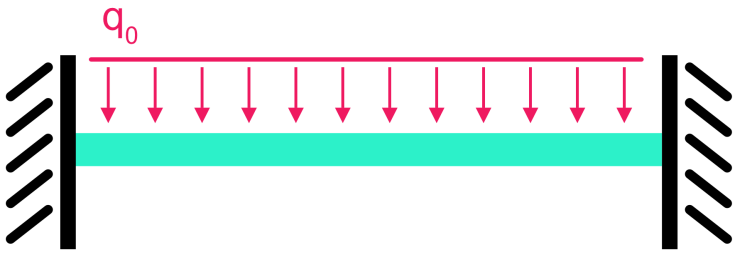

Figure 4.1: Double cantilevered bar under uniform load.

The analytical solution for the bending line of a cantilevered beam under uniformly distributed load, as presented in figure 4.1 derives from the following relation[Fri19]:

$$w''(x) = -\frac{M_B(x)}{EI_y(x)} \tag{4.1}$$

Where w'' is the local curvature of the beam or the second derivative of the deformed beam's location in y-direction under load. M_B is the bending moment, E the Young's module and I_y the geometrical moment of inertia.

Integrating twice, this leaves us with an equation describing the bending line of a beam:

$$w(x) = \int\int -\frac{M_B(x)}{EI_y(x)} dx\ dx + C_1 x + C_2 \tag{4.2}$$

For a cantilevered beam under uniform load, force and bending moment are given by:

$$F(x) = q_0(l - x) \tag{4.3}$$

$$M_B(x) = -\frac{q_0}{2}(l - x)^2 \tag{4.4}$$

Where q_0 is the constant loading and l is the length of the beam. The fixed end of the beam is hereby located at $x = 0$.

The geometrical moment of inertia for a beam with rectangular cross section is given by [Fri19]:

$$I_y = \frac{bh^3}{12}$$

Where b is the width of the beam and h its height.

The boundary conditions are:

$$\begin{aligned} w(0) &= 0 \\ w'(0) &= 0 \\ w(l) &= 0 \\ w'(l) &= 0 \end{aligned}$$

This leads to the following function describing the deflection of the double cantilevered bar:

$$w(x) = -\left(\frac{1}{24}q_0x^4 - \frac{q_0 l}{12}x^3 + \frac{q_0 l^2}{24}x^2\right)\frac{1}{EI_y}$$

Figure 4.2 shows the comparison of deflection lines obtained from 3D and 2D (plane stress) FEM analysis with the analytic solution. The resulting curves are virtually identical as should be expected for such a trivial use case.

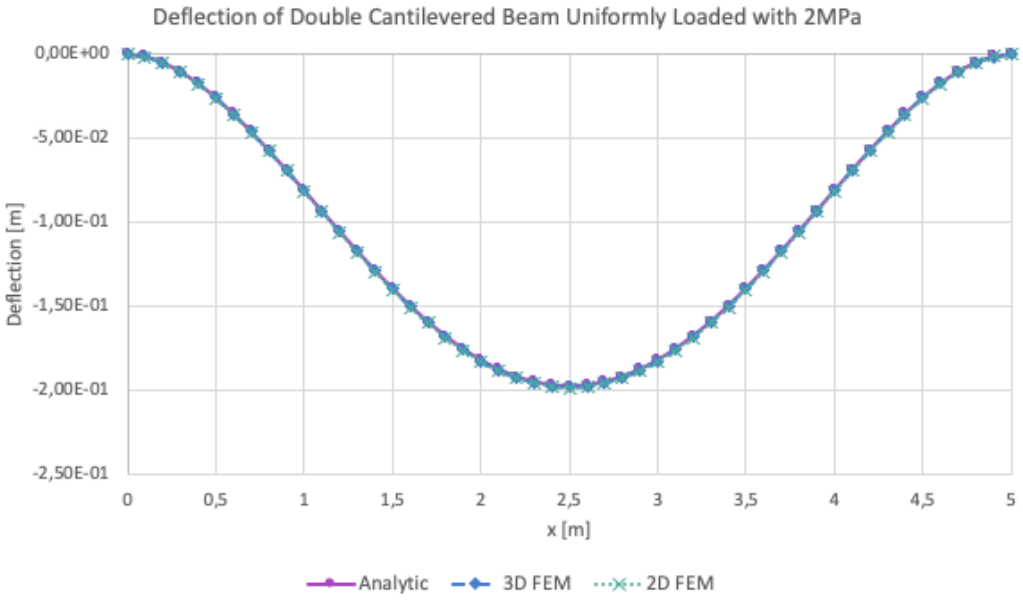

Figure 4.2: Deflection line of a double cantilevered bar uniformly loaded with 2MPa

4.1.2 Pressurized Thin-Walled Cylinder with Infinitely Rigid Closed Ends

The pressurized cylinder problem in its setup is very similar to the double cantilevered bar problem with uniform loading. The goal of this test is to verify the 2-D axisymmetric FEM formulation. We suppose the cylinder to be closed at both ends with an infinitely rigid lid. Hence, we restrict all degrees of freedom of the cylinder wall at the upper and lower end. And we can remove the lid itself from the analysis. Figure 4.3 shows both a 3-D and a 2-D representation of the problem.

Analytic Solution

Analytic solutions for pressurized cylinders of infinite length are straight forward since the stress and strain state of the problem are essentially 1-D. It involves only hoop stress and -strain. For pressurized cylinders with closed ends, the analytic solution becomes more complex. It is important to note that the following discussion supposes a perfectly axisymmetric geometry under a perfectly axisymmetric, static load. We assume the cylinder to be thin-walled. Referring to the definition given in [Vul14] where a cylinder is considered thin-walled if $s \leq r_i/10$ holds. Here, s is the wall thickness and r_i the cylinder's internal radius. We assume the material behavior to be linear elastic at all times.

To describe the deflection of the cylinder wall at equilibrium configuration, we rely on the fourth-order non-homogeneous differential equation given by Vullo [Vul14]:

$$\frac{d^4u}{d^4z} + 4\beta^4 u = -\frac{p_i}{D} \tag{4.5}$$

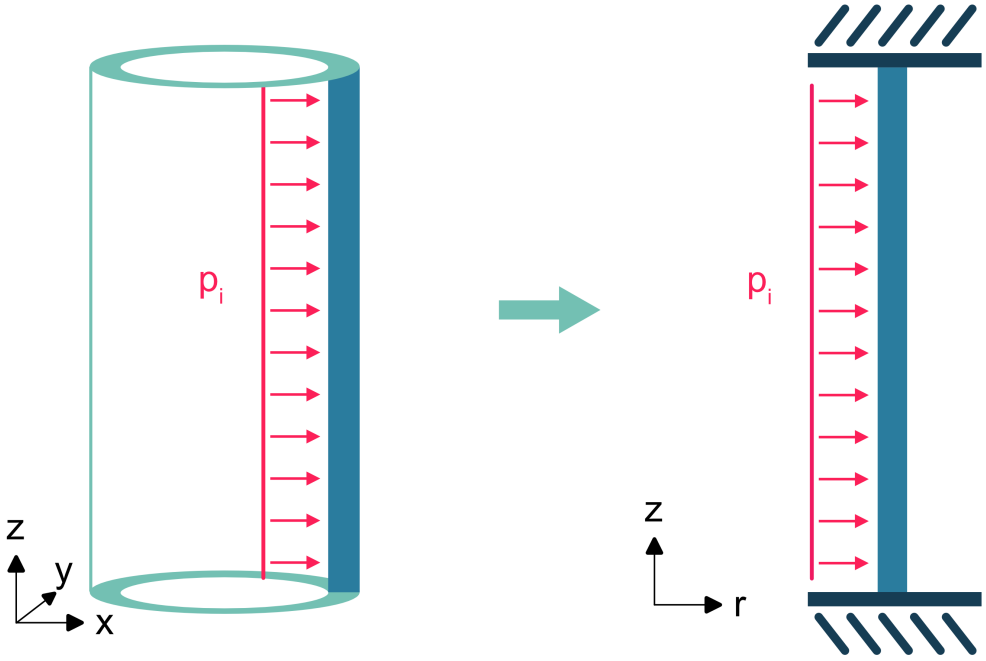

Figure 4.3: Setup for the structural verification case of a thin-walled cylinder with perfectly rigid ends under uniform internal pressure.

Where D is a the shell's flexural rigidity defined by $D = Es^3/(12(1-\nu^2))$. The solution for 4.5 consists of a homogeneous and a particular part give by[Vul14]:

$$u = u_h + u_p$$

where

$$u_h = e^{\beta z}(C_1 cos(\beta z) + C_2 sin(\beta z)) + e^{-\beta z}(C_3 cos(\beta z) + C_4 sin(\beta z)) \tag{4.6}$$

$$u_p = -\frac{p_i}{4\beta^4 D} = -\frac{p_i R^2}{Es} \tag{4.7}$$

Where $\beta^4 = \frac{3(1-\nu^2)}{R^2 s^2}$ with ν the Poisson ratio, s the wall thickness and R the mean radius. E is the Young's modulus and p_i the internal pressure. $C_{1..4}$ are integration constants. We obtain them by inserting the adequate boundary conditions and solving the resulting system of linear equations. In our case the boundary conditions are:

$$\begin{aligned} u(0) &= 0 \\ u(L) &= 0 \\ u'(0) &= 0 \\ u'(L) &= 0 \end{aligned}$$

Numerical Analysis

Now that we have the analytic solution set, the goal is to verify the relevant formulations of the FEM code. I analyze the problem both with a three-dimensional and a 2-D axisymmetric formulation. I conducted both analysis and compared the results with the analytic solution. The analysis setup varied slightly for the 3-D and the 2-D case and are summed up below.

2D Axisymmetric Setup The two-dimensional finite element model consists of a slab with a thickness of 100mm and a length of 5m. The internal face lies at a radial position of 1m from the center. Upper and lower face of the cylinder slab are fixed with both degrees of freedom restricted for the corresponding boundary vertices. The mesh, as shown in figure 4.4a, consists of 2122 triangular elements with quadratic shape functions. This corresponds to about 4 elements over the thickness of the slab. The pressure of 2 MPa acts on the internal face while no boundary conditions apply on the outer face.

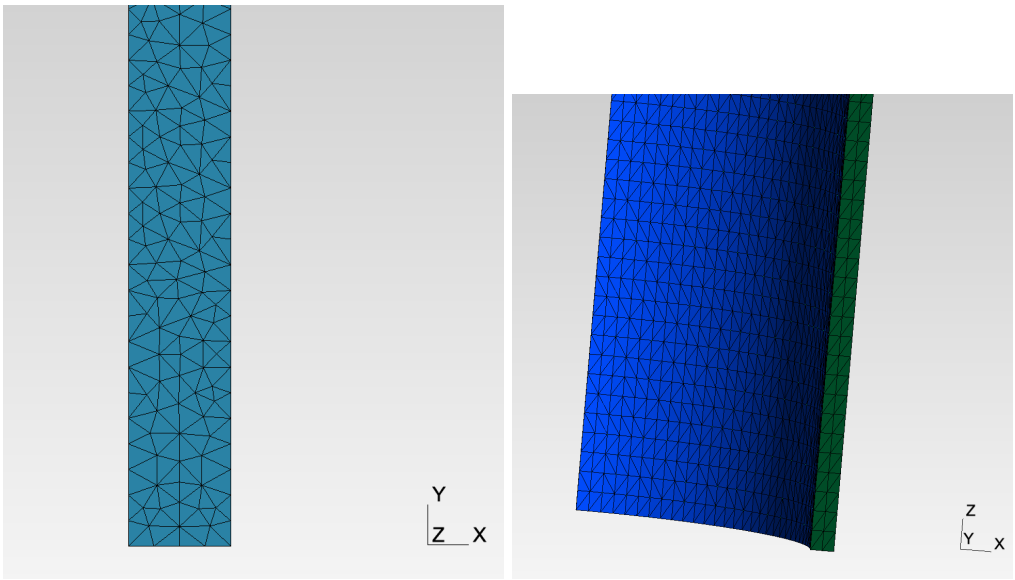

(a) 2-D mesh. (b) 3-D mesh.

Figure 4.4: Detail of the two- and three-dimensional meshes for the pressurized thin-walled cylinder showing the lower end of the computational grid.

3D Axisymmetric Setup The three-dimensional Finite Element (FE)-model consists of a 1/4 cylinder meshed with 21600 tetrahedral elements as shown in figure 4.4b. This results in a mesh with two second order elements over the wall thickness.

Like in the two-dimensional model, I restrict all movement at the upper and lower end of the cylinder. The pressure acts on the internal face while the outward face is subject to no boundary conditions. On the symmetry planes, I restrict movement in face normal direction (x- and y-direction respectively).

Results and Discussion

Table 4.1 displays the problem parameters as used in analytic and numerical analysis. For cases A and B, the inner radius of the pressurized cylinder varies. The material parameters are those of 316FR stainless steel.

Table 4.1: Problem parameters for the verification case of a thin-walled cylinder under uniform internal pressure.

Quantity	Unit	Value
Internal radius *Case A*	m	1
Internal radius *Case B*	m	2.3
Wall thicknes	m	0.1
Cylinder length	m	5
Internal pressure	MPa	2.0
Young's modulus	GPa	198.0
Shear modulus		0.27

Figures 4.5 and 4.6 show the results of the analysis for the cases A *and* B.

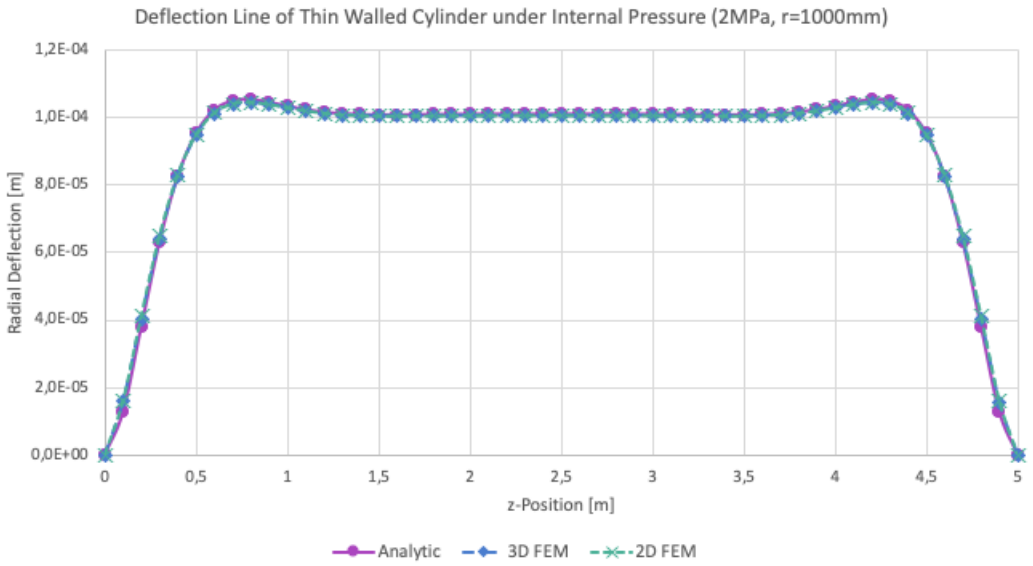

Figure 4.5: Deflection curve of a cylinder with inner radius of 1m and wall thickness of 0.1m under internal pressure of 2 MPa with infinitely rigid closed ends.

For case A with an inner radius of 1m we see excellent agreement of analytic and numerical solution. The deflection curve of both 2-D and 3D numerical analysis in figure 4.5 are virtually identical.

For case B as shown in figure 4.6, both numerical results once again perfectly overlap. The analytic model however predicts a significantly higher deformation. The resulting error between numerical and analytic solution is 4%

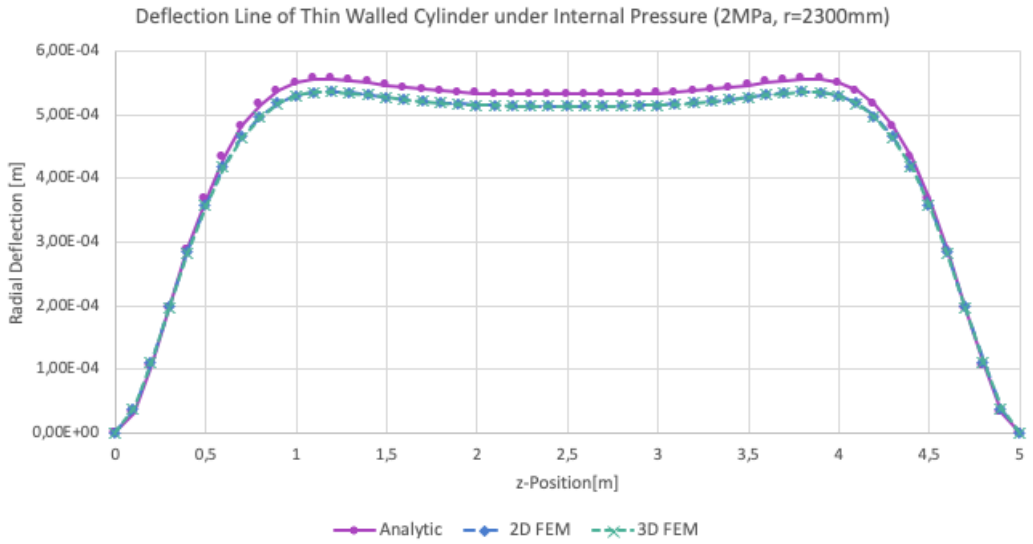

Figure 4.6: Deflection curve of a cylinder with inner radius of 2.3m and wall thickness of 0.1m under internal pressure of 2 MPa with infinitely rigid closed ends.

This might result from a rounding error in the calculation of the integration constants for the analytic solution. The integration constants for case B are: $\{C_1 = 1.07\ 10^{-9}, C_2 = 1.2010^{-10}, C_3 = 5.3410^{-4}, C_4 = 5.3410^{-4}\}$.

2-D and 3-D FEM analysis agree perfectly for all configurations of the pressurized thin-walled cylinder case. The 3-D FEM analysis predicts the deflection of a bending bar problem in accordance with the analytic solution, as discussed in section 4.1.1. We can hence conclude that the axisymmetric 2D FEM formulation predicts the deflection of a pressurized cylinder correctly.

4.1.3 Tensile Probe Test

Tensile tests are a standard method for determining material parameters. The setup is straightforward in that a tensile probe is elongated according to a predefined transient function. The resulting stress state is primarily uniaxial. We monitor the resulting stress in the numerical analysis and compare it to the stress-strain curve given by the one-dimensional stress-strain relation. The tensile test is useful as a validation case for 3-D and 2-D (axisymmetric) setups in the elasto-plastic formulation.

In the **linear elastic case**, the stress-strain relation is given by Hooke's law:

$$\sigma = E\epsilon$$

where σ and ϵ are cauchy stress and engineering strain respectively. And E is the Young's modulus of the material in question.

The stress-strain relation for the **elasto-plastic case**, or – to be precise – the elastic-plastic case with multi-linear isotropic hardening, is given by the following, incremental equation:

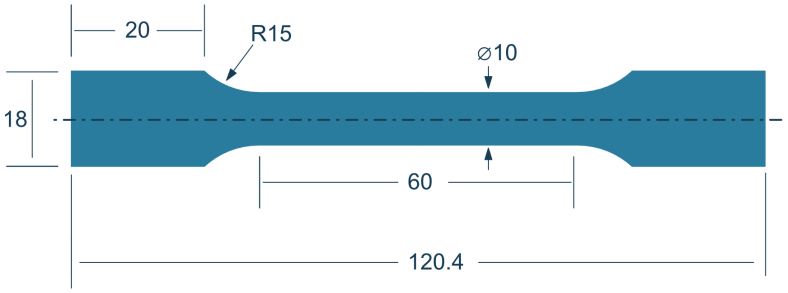

Figure 4.7: Dimensions of the probe used for uniaxial tensile tests in the verification of the elasto-plastic linear and multi-linear hardening models.

$$\Delta\sigma = \Delta\epsilon C_{ep} \tag{4.8}$$

Where C_{ep} is the tangential stiffness opeartor. C_{ep} is equal to E for $\sigma < \sigma_y$ or $C_{ep} = \frac{EK_{iso}}{E+K_{iso}}$ where K_{iso} is the isotropic hardening parameter dependent on the current stress state.

The tensile probe in this case is an axisymmetric specimen as shown in figure 4.7. In the three-dimensional case, I modeled a quarter of the entire geometry and applied zero-displacement boundary conditions in face normal direction on the symmetry faces.

Numerical Model for Tensile Test

The numerical model of the tensile test is a recreation of the original specimen use by Nakamura et al [NKI+04b] in their material tests. I also created a second, simplified version in 2-D. The simplified model is a 60 mm long cylinder with a diameter of 10 mm.

The mesh for the 2-D axisymmetric full geometry case consists of 6157 triangular elements.

Results of Tensile Verification Case

As figure 4.8 shows, the results from the numerical analysis align perfectly with multilinear material model. The FEM code is capable to accurately represent elasto-plastic material behavior with a multi-linear, isotropic strain hardening model.

4.1.4 One-Dimensional Waterhammer

The water hammer is an important problem of fluid-structure interaction and has been extensively studied. Among others by [aT96] [Tij07], [TL90] and [SAH90]. [BST06] gives a good overview on work relating the water hammer problem.

The phenomenon consists of a liquid slug impacting the closed end of a pipe where it is brought to an abrupt stop. Some scenarios involve a dampening gas cushion between liquid slug and pipe end, reducing the peak pressure and widening the pressure peak at the same time.

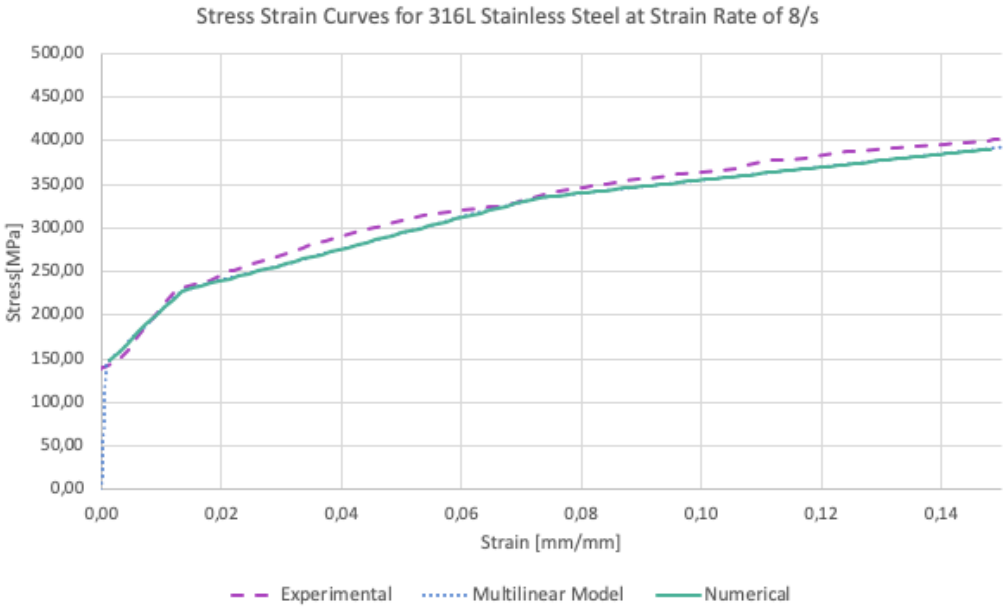

Figure 4.8: Stress-strain curves for the tensile verification case comparing experimental results from [AM80], multi-linear hardening and numerical results for 316L at 550°C with a strain rate of 8/s.

Analytical solutions are available both for the case of a rigid pipe (without fluid-structure interaction) and an elastic pipe (with fluid-structure interaction). The water hammer problem with rigid walls is furthermore a validation problem of the SIMMER III code assessment phase I ([KBT+96]).

Problem Parameters for the Sodium Hammer Verification Case

Table 4.2: Test parameters for the sodium hammer validation case.

Quantity	Symbol	Unit	Value
Inner pipe diameter	D_i	mm	50.0
Pipe wall thicknes	h_{wall}	mm	1.5
Length of sodium plug	L_{plug}	mm	550.0
Initial velocity of plug	v_0	m/s	20.0

For the analysis of the sodium hammer problem I used material data for sodium as given in the SIMMER Handbook evaluated at a temperature of 700K. I assumed a generic steel as structural material for the pipe.

Table 4.3: Material parameters for the sodium hammer validation case used in analytical and numerical model.

Quantity	Symbol	Unit	Value
Density of sodium	ρ_{Na}	kg/m^3	840.4
Speed of sound in sodium	c_{Na}	m/s	2357.7
Equivalent speed of sound	c_f	m/s	2672.0
Density of steel	ρ_S	kg/m^3	7850
Young's Modulus of steel	E	GPa	198.0

Analytic Solution

Multiple analytical solutions for water hammer problems with flexible pipes are available in a varying degree of complexity. The most commonly used is the two-equation model [aT96], which I employed here:

$$\frac{\partial V}{\partial t} + \frac{1}{\rho_f}\frac{\partial P}{\partial z} = 0 \tag{4.9}$$

$$\frac{\partial V}{\partial z} + \frac{1}{\rho_f c_f^2}\frac{\partial P}{\partial t} = 0 \tag{4.10}$$

Where c_f is the (modified) velocity of sound. In unconstrained fluids, $c_0 = \sqrt{K/\rho_f}$, where K is the fluids bulk modulus. And in the constrained fluid:

$$c_1 = \sqrt{\frac{Es}{\rho_f D}} \tag{4.11}$$

With E the Young's Modulus, s the wall thickness, and D the inner diameter of the pipe.

I solved the differential equation by implementing a basic finite difference time-stepping algorithm on a one-dimensional grid in MS Excel.

Numerical Analysis Setup

The numerical setup consists of a fluid dynamic mesh with 44 cells in axial direction and 1 cell in radial direction. Furthermore, we have a 3D structural domain consisting of 1/4th of a thin-walled cylinder geometry. I meshed the pipe section with 18'000 second order tetraherdon elements. The top end of the cylinder is fixed and no displacements in any direction is permitted. Displacement on the symmetry boundaries is restricted in face normal direction. At the lower end, I allow movement in radial direction but restrict axial movement. The upper pipe end (flange) is not part of the structural model and regarded as perfectly rigid.

Result of Water Hammer Validation Problem

Figure 4.9 shows the comparison of pressure curves obtained from analytical solution and numerical analysis. The curves show good agreement as expected for this simple case. Duration of the pressure head and maximum pressure differ only slightly.

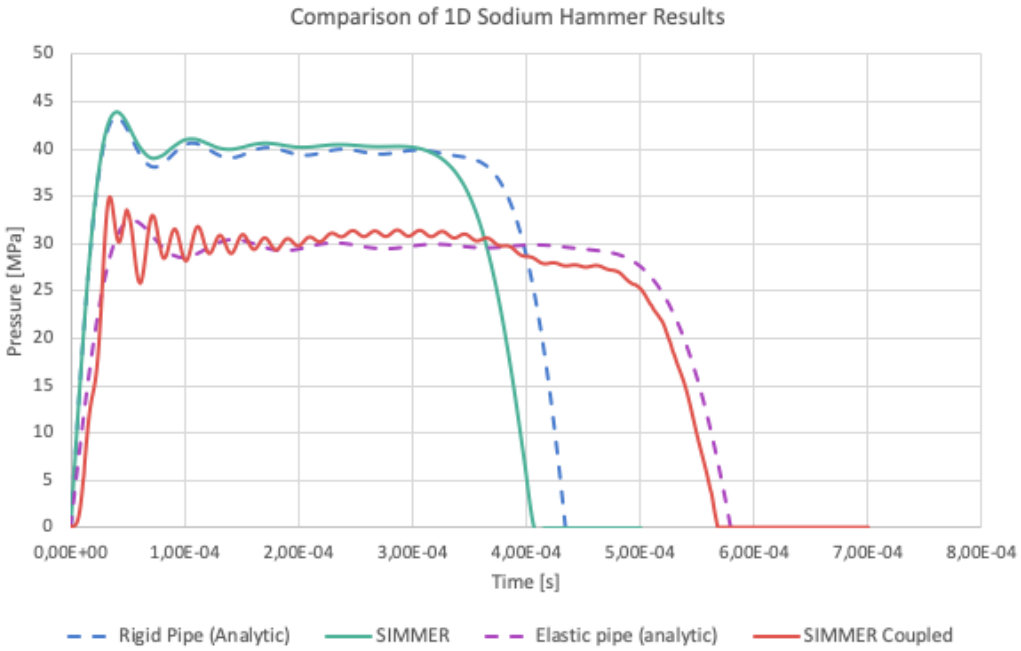

Figure 4.9: Comparison of analytic and numerical results for the verification case of a one-dimensional sodium hammer problem.

In both, rigid and elastic case, the numerical model predicts a slightly higher peak pressure and a slightly shorter duration. In the rigid case, the numerical analysis predicts the maximum pressure to be 8.7% higher compared to the analytic result. The predicted duration is shorter by 4.4%. In the elastic case the discrepancies are 15.3% for the pressure and 2.0% for the duration respectively.

This proves that the coupled code can consistently treat a simple, one-dimensional FSI problem in the form of a water hammer. For the two-dimensional case, analytic solutions are unavailable and only experimental results can be consulted. The treatment of two-dimensional waterhammer problems with elastic and elasto-plastic boundaries is subject of the next section.

4.2 Validation

I verified the functionality of the code by comparing its predictions to experimental results from Nakamura et al [NKI+04b]. They conducted several experiments modeling the expansion phase in a fast rector vessel. The results of those experiments are well documented. Their

work also includes the documentation of material properties for the stainless steel used in the experiments.

4.2.1 Experimental Setup

The experiment consists of a cylindrical container that is partially filled with water at room temperature and ambient pressure. A second pressurized air tank connects to the bottom of the container separated by a rupture disk. Once the rupture disk breaks, the compressed air forces its way into the water tank. Thereby, it accelerates the water upwards and creates a liquid slug that hits the upper vessel's lid before propagating outwards.

Nakamura et al. conducted experiments with a thin, easily deforming vessel and a thick-walled, nearly rigid vessel. This allows a to verify that the unmodified SIMMER code with no model for deforming vessel walls delivers the expected results. Since the test geometry is nearly axially symmetric, SIMMER's 2-D formulation should not be an issue.

Measurements from several pressure sensors are available which allows us to compare the pressure profile over time between experiments and simulation. The two most important measurements on the lid about halfway out and on the upper end of the vessel wall.

4.2.2 Numerical Setup

I conducted several numerical analysis of the CDA test experiments originally devised by Nakamura et al [NKI+04b]. The intention behind this was first to test the capabilities of several code versions and formulations (2-D vs 3-D, plastic vs linear elastic). And second to compare the case of the rigid test vessel to an uncoupled, purely fluid dynamical numerical analysis using SIMMER without the newly developed structural code.

Fluid Dynamic Setup

The model of the fluid dynamics side of the problem consists of:

- The cylindrically shaped, water-filled test vessel
- The pressurized gas tank below the vessel
- The gas-cushion at the top of the test vessel
- The radial vessel wall that is, depending the case:
  - Fixed at a cell boundary
  - Fixed inside the last radial cell
  - Moving inside the last radial cell

The SIMMER grid consists of 65 radial and 96 axial cells. The lowest 5 axial cells make up the pressure tank below the test vessel. Between cells 5 and 6, a virtual wall separates the lower, gas tank region from the water-filled test vessel region. The virtual wall has an opening towards the radial center of the grid (between radial cells 1 and 15). The wall reaches down into the gas tank to model the tube in the original experimental setup used by Nakamura et al [NKI+04b]. Towards the top of the test vessel, the axial grid size gets progressively smaller. We hereby obtain a better resolution in the area where the liquid slug impacts vessel lid which deflects it outwards to the vessel wall. In this area, we can expect the highest pressure peaks.

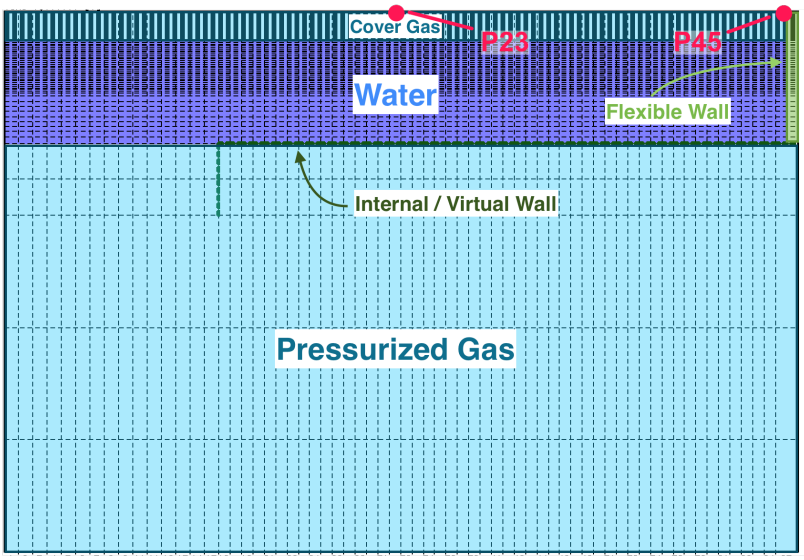

Figure 4.10: SIMMER grid for the validation case of the coupled FSI code including locations of pressure sensors. Mesh regions at t=0s.

Figure 4.10 gives an overview of the dimension of the SIMMER model.

All boundaries – with exception of the flexible wall (if present) – are non-slip, rigid boundaries restricting both fluid flow and heat transfer in face normal direction. Initially, the air in the lower pressure tank has a pressure of 2.0 MPa. Both fluids in the test vessel are at ambient pressure (1 bar) and 310K. The elevated liquid temperature with regards to the experimental setup guarantees the numerical stability of SIMMER's Equation Of State (EOS) model.

Rigid Structure Case

For the rigid vessel case I use two different numerical setups. First, the classic SIMMER approach where the fluid domain ends with the last cell in radial direction. Second, a setup where the boundary to the fluid lies inside a cell that is partially filled with right canwall no flow area volume. While I make use of the immersed boundary formulation, there is no fluid structure interaction in this case. The boundary remains static throughout the analysis.

The idea is to verify that both problem formulations are equivalent and deliver the same result as the experiments. In both cases, the SIMMER source code is the original one and was not modified.

Flexible Structure Case

The flexible case is where I rely on the structural analysis to determine the response of the vessel wall. Again, I use multiple setups to compare the reliability of different formulations. I varied:

- Material model

  - Linear elastic
  - Elastoplastic
- Structural mesh
  - coarse vs fine
  - tetrahedron vs hex elements
- Finite element order
  - first order
  - second order
- Problem dimension
  - 2D
  - 3D

Structural Mesh The structural domain consists of a thin-walled cylinder of height 780 mm, inner radius 520 mm with a wall thickness of 5 mm. I refrained from including vessel lid and bottom in the structural analysis and assumed them to be completely rigid. Internal structures, as included in some experimental runs by Nakamura et al. [NKI+04b] are also not part of the numeriacl structure model.

I used both simplex and tensor product type cells to test the capabilities of the code in both variants. Tensor product grids are all regular while simplex grids are primarily irregular. Figure gives a selection of structural grids used in the analysis.

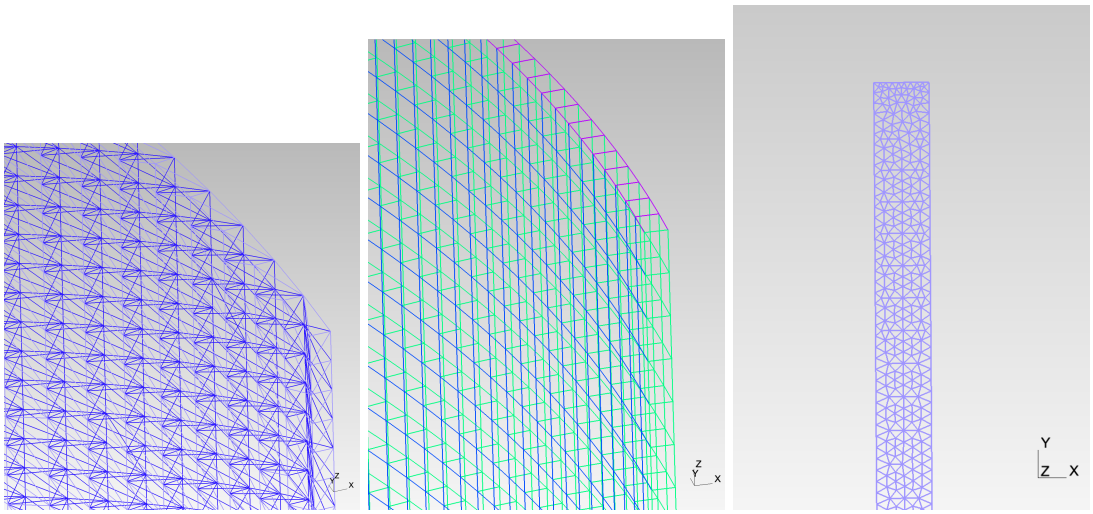

(a) 3D mesh with 30'000 tetrahedral elements. (b) 3D mesh with 8'000 hexahedral elements. (c) 2D mesh with 5'648 tri elements.

Figure 4.11: Examples of meshes used in the validation case for the structural code.

Table 4.4 gives an overview of the different grids used during the code assessment.

In the three-dimensional case, the computational grid consists of 1/4 of the cylindrical test vessel. In the two-dimensional analysis, I reduced the geometry to a simple rectangular slab representing the cross-section of a cylinder in axial direction.

Table 4.4: Overview of different meshes for the structural analysis in the validation case of the coupled code.

Dimension	Element Type	Coarse Grid	Fine Grid
2	simplex irregular	2'834	5'648
3	simplex irregular	20'766	73'348
3	simplex regular	30'000	126'000
3	tensor product	2'500	8'000

Boundary Conditions The structural model has three relevant boundaries in the two-dimensional case and five in the three-dimensional case.

In the two-dimensional case, the upper and lower boundaries are fixed and no movement is permitted in either axial or radial direction. On the *inner* boundary, the pressure obtained from the SIMMER analysis is imposed as a Neumann boundary condition.

In the three-dimensional case, upper and lower end of the cylinder are fixed in a similar manner to the 2-D case. The Dirichlet BC restricts movement in x,y and z - direction. On the symmetry faces, where the cylinder is sliced in axial direction, movement in face normal direction is prohibited. On the inner face of the cylinder, again, the pressure from the SIMMER analysis acts as a Neumann boundary condition.

4.2.3 Results of Validation Case

Rigid Case

Figures 4.12 and 4.13 present the pressure transients for the validation case with a rigid vessel. We can see a good agreement between experimental data and numerical results at the lid close to the wall (4.12). Further inward, SIMMER seems to underpredict the pressure peak by 16%.

We can also see that both problem formulations (domain boundary vs immersed boundary) deliver similar results. The higher pressure peak in the unmodified SIMMER case most likely results from a different transient resolution in the SIMMER post processing file. We can therefore conclude that using the obstructed volume approach for the immersed boundary is justifiable.

Linear Elastic Case

Figures 4.14 and 4.15 show the pressure histories of experimental results and the linear elastic coupled numerical analysis. As expected, the deflection of the vessel wall reduces the observed peak pressure. During the experiments, the test vessel underwent plastic deformation. The linear elastic model cannot account for the reduced stiffness in the plastic regime. The structural response in the numerical linear elastic model is hence stiffer than in reality. We would therefore expect to find the pressure history for the linear elastic coupled analysis to progress somewhere between the rigid and the elasto-plastic experiment. This is exactly what we observe in figures 4.14 and 4.15.

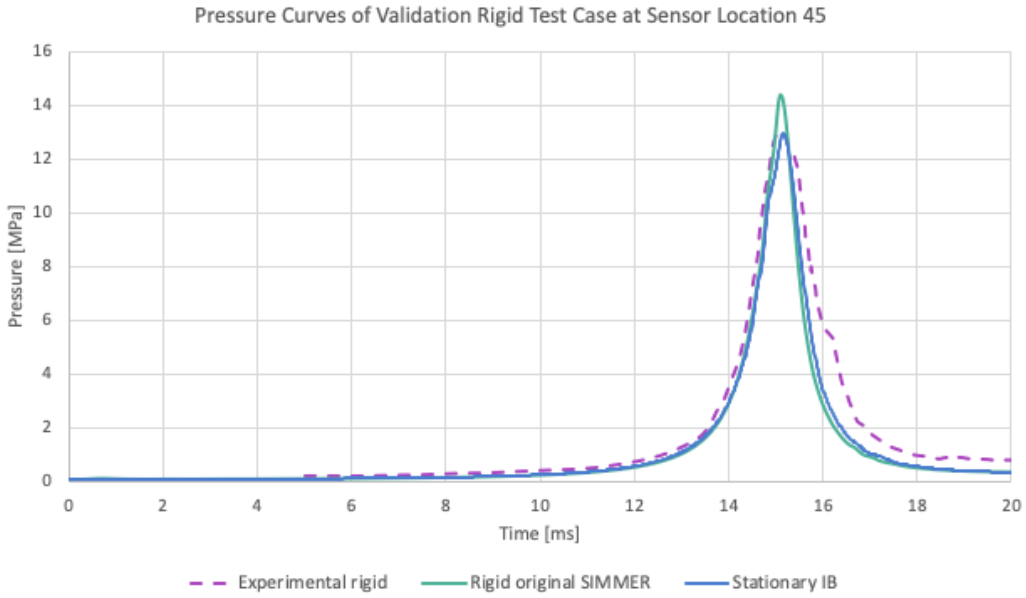

Figure 4.12: Comparison of pressure history for linear elastic validation case at pressure sensor location 45 between numerical and experimental [NKI+04a] results.

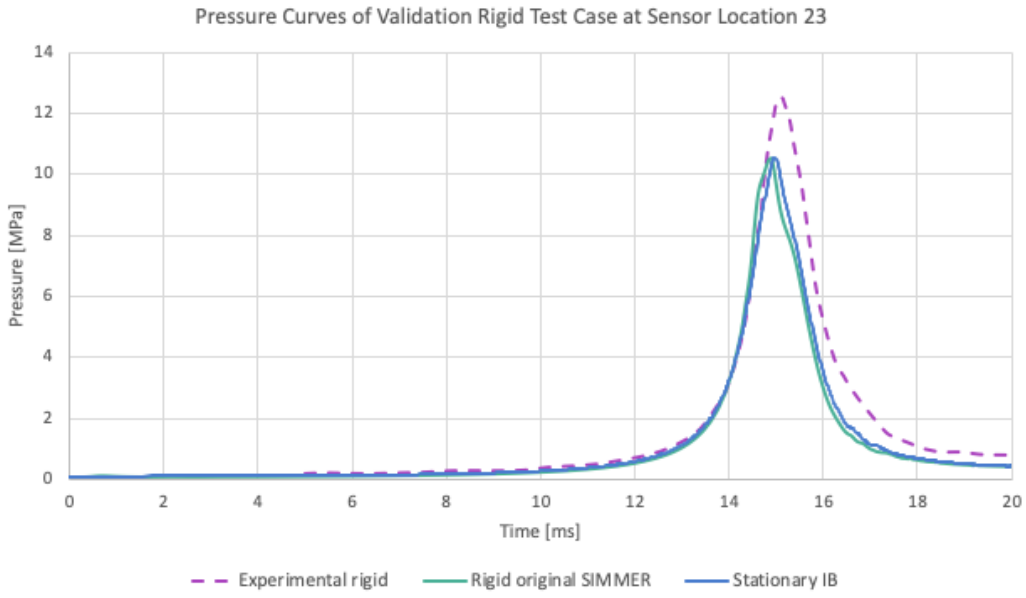

Figure 4.13: Comparison of pressure history for linear elastic validation case at pressure sensor location 23 between numerical and experimental [NKI+04a] results.

The pressure transient from the linear elastic analysis retraces the experimental results accurately until reaching the peak pressure. It then falls off quicker than for the experimental results and

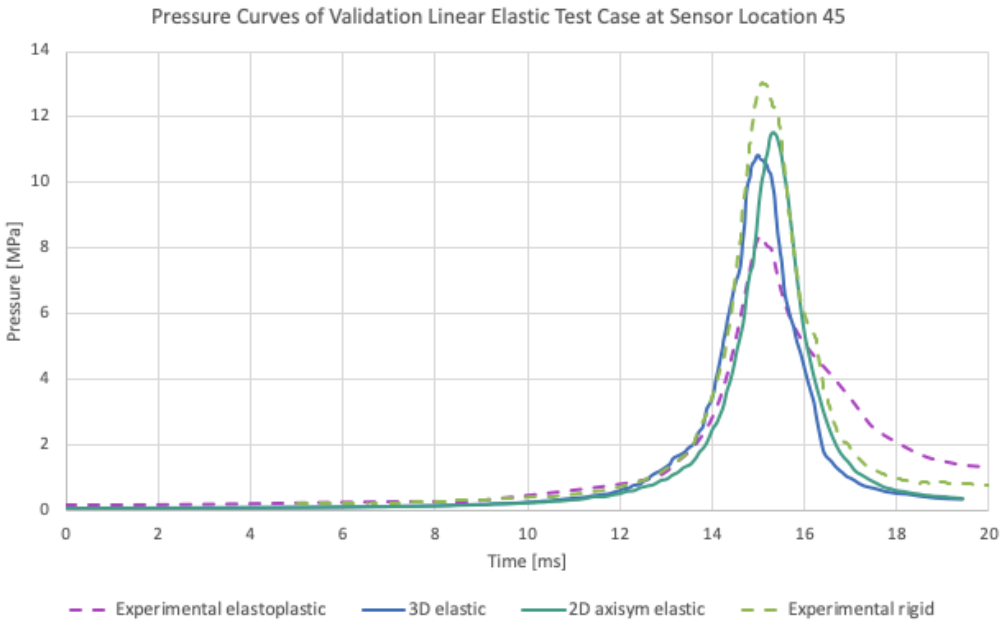

Figure 4.14: Comparison of pressure history for linear elastic validation case at pressure sensor location 45 between numerical and experimental [NKI+04a] results.

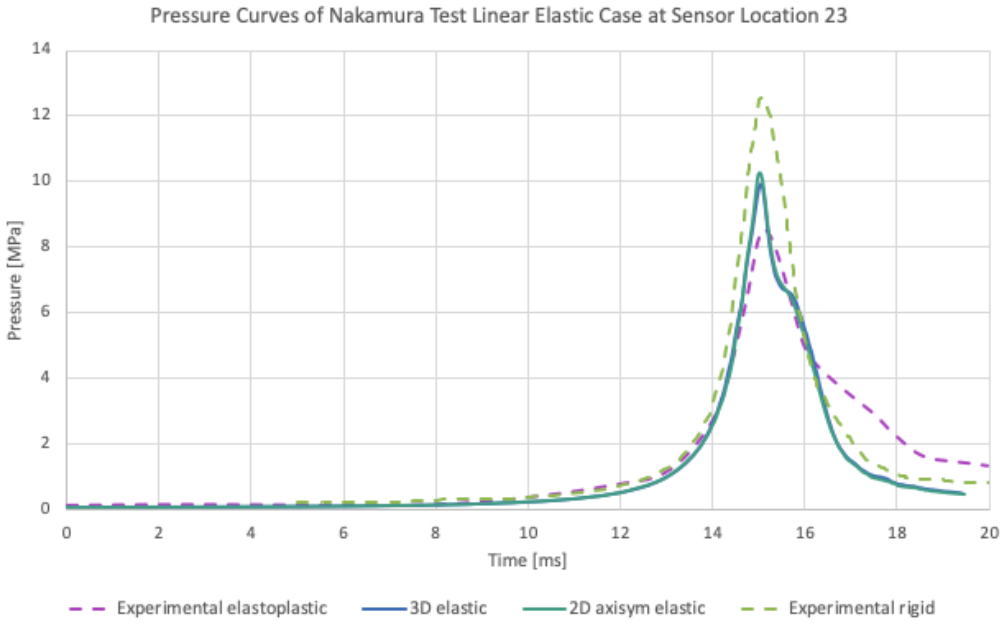

Figure 4.15: Comparison of pressure history for linear elastic validation case at pressure sensor location 23 between numerical and experimental [NKI+04a] results.

settles on a lower post-impact pressure. While the peak pressure is significantly reduced, the overall chronological sequence is closer to the rigid case than the elasto-plastic case.

The reason for the shorter overall duration with respect to the experiments could be the speed of sound of water obtained from SIMMER's EOS model. Apart from water being a challenging material to model , SIMMER's main application are metal-cooled fast reactors. While a model for water is implemented in the material library, it is only use for validation and verification cases. Outside the relevant temperature and pressure ranges for those cases, the model is known to show inaccuracies and may need manual adjustments.

The curves from 2D and 3D elastic analysis show good agreement. Especially at sensor location 23 on the vessel lid. At location 45 on the vessel wall, the pressure peak is higher and slightly delayed in the 2D case. A possible explanation for the lower peak pressure is that for the 3D elastic analysis I used a relaxation factor of 0.6. Later analysis of the use case with and without a relaxation factor applied and otherwise unchnged parameters confirmed that suspicion. Relaxation reduces the peak pressure as it softens the structural response.

Elastoplastic Case

Deformation of Vessel Wall For the linear elastic case, the deformation of the immersed boundary is difficult to visualize. For the elasto-plastic case, a significant deformation of the wall on the upper part of the vessel is clearly visible. Figure 4.16 shows the phase plot of the elasto-plastic coupled case at time of the slug impact. The phase plot shows the volume fractions of water and gas in blue and white respectively. The lower pressurized gas tank is not depicted. To illustrate the fluid / solid boundary, I retraced the deflecting vessel wall by hand in red.

We see the water slug impacting the vessel lid, leaving a small air pocket close to the vessel wall. Below the slug, pressurized air enters the cylindrical test vessel from the pressure tank. Beyond the immersed vessel wall, the inert filler material takes up all the space. SIMMER's phase plot functionality displays this filler material also as white. The vessel bulges out significantly near the lid, as expected from the experimental results.

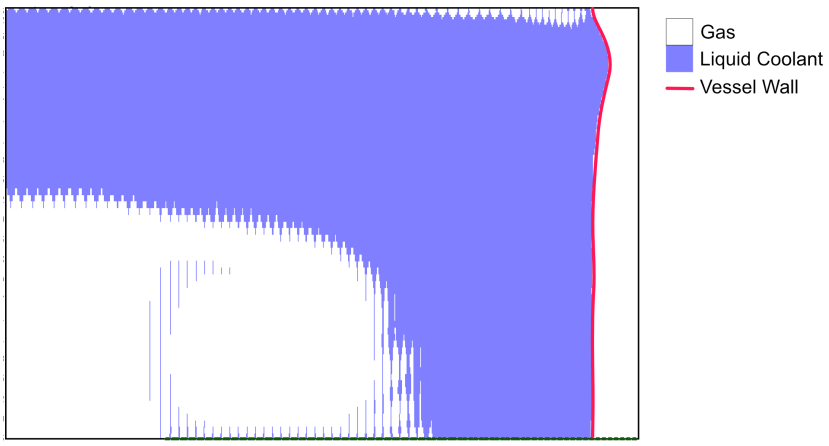

Figure 4.16: Deformation of the vessel wall in the validation example case with elastoplastic structural coupling at the moment of slug impact. Vessel wall visualization added by hand.

Figure 4.17 compares the radial deformation of the vessel along the axial length. While the overall shape conforms well, the numerical model tends to over-predict the deformation. Reason for this general over-prediction is likely the simplistic material model neglecting the unusual strain rate sensitivity of stainless steel [LS04]. As well as kinematic hardening effects.

The experimental vessel was depressurized prior to determining the residual deformation. In the numerical model, the vessel remained under internal pressure of 10 bar. The curve resulting from the numerical analysis hence includes an elastic deflection while the curve from the experimental results does not.

Between around 450 and 600 mm the numerical model under-predicts the deformation producing a more pronounced but less broad bulge.

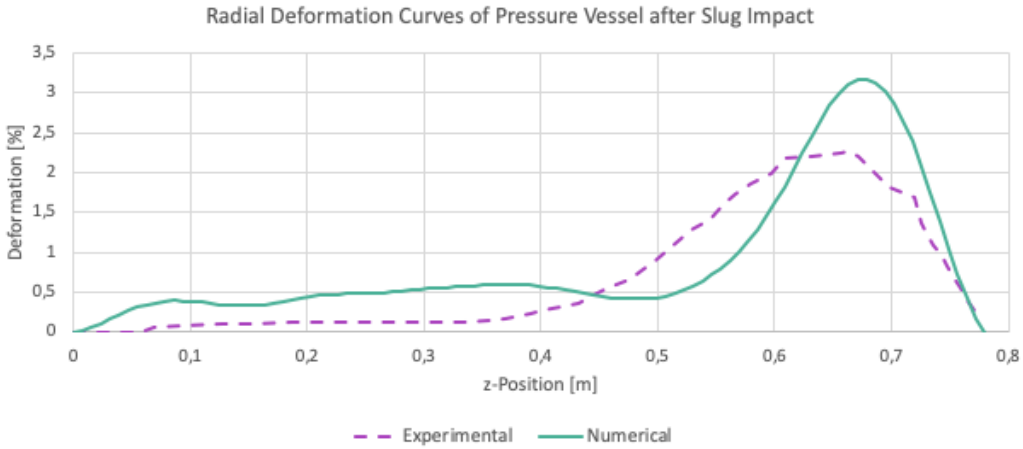

Figure 4.17: Comparison of residual deformation of test vessel after slug impact from experimental and numerical results.

Pressure Response Figures 4.18 and 4.19 show the pressure as function of time on sensor locations 23 and 45 respectively. The numerical results agree well with the experimental data especially during the pressure buildup. As in the elastic case, discussed in section 4.2.3, the pressure drops off quicker and settles on a lower level in the numerical analysis than in the experiments.

At the vessel wall (sensor location 45), we can observe some spurious pressure oscillations. Relaxation in the coupling might remedy this phenomenon, but I did not conduct the according tests with several relaxation factors.

4.3 Performance

The analysis of HCDAs typically requires very small time step sizes to adequately model phenomena like nuclear heat generation, fuel-coolant interactions. While the power excursion and resulting expansion phase generally show a duration of less than five seconds, the small time-step

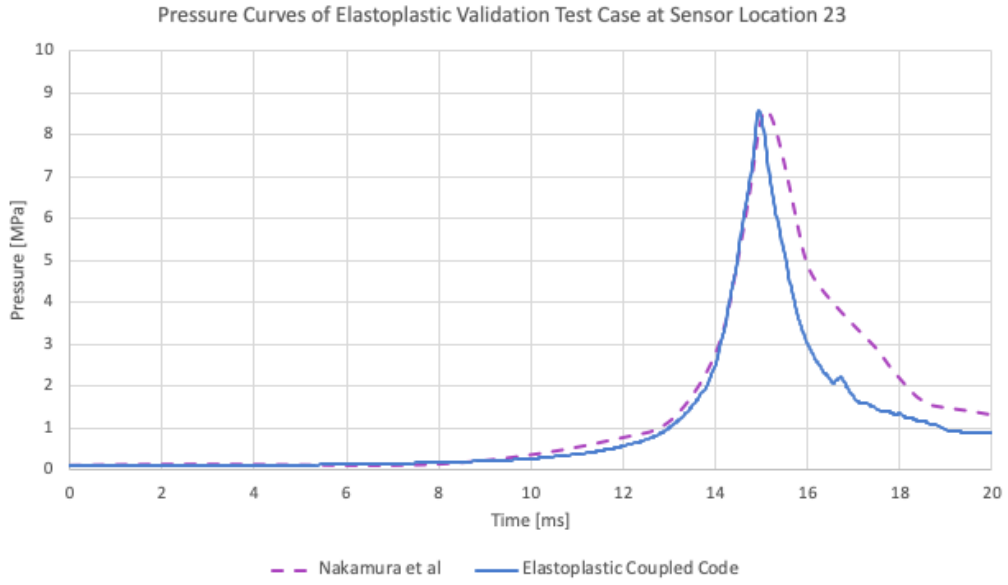

Figure 4.18: Comparison of pressure history for elastoplastic validation case at pressure sensor location 23 between numerical and experimental [NKI+04a] results.

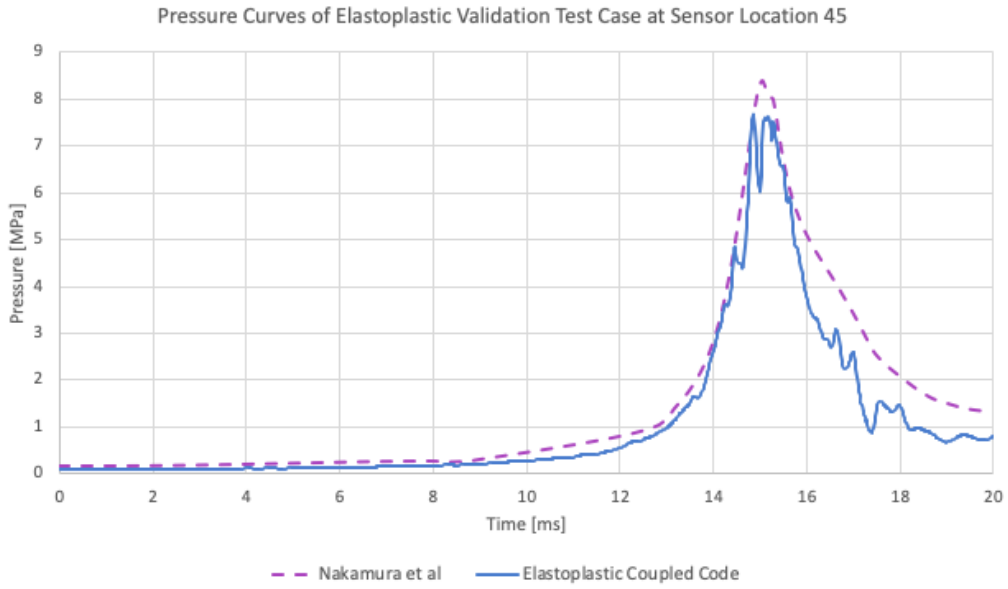

Figure 4.19: Comparison of pressure history for elastoplastic validation case at pressure sensor location 45 between numerical and experimental [NKI+04a] results.

size in the order of $10^{-5} - 10^{-4}$ leads to a significant amount of iteration steps for SIMMER. A typical analysis like the use case discussed in chapter 5 includes about 50'000 iteration steps.

The performance of the coupled code and in particular the structural part is an important factor to ensure the usefulness of the code. A slow structural solver will increase the run time of the problem up to a level where the use of the coupled code becomes impractical or economically unattractive. While other parts of the coupled code can also influence performance, the structural solver is clearly the bottleneck. Especially in the three-dimensional case, solving the structural problem is a resource-intense endeavor. To obtain results in a reasonable amount of time, the computation time per time-step should be below ten seconds. While we can reach those times easily on a single processor using the 2-D axisymmetric formulation, the 3-D formulation requires significantly more resources. The first version of the coupled code with 3-D FEM formulation took about 15 min solving time per time-step.

To improve the performance of the 3D coupled code, I considered the following options:

- Parallelization
- Skipping time-steps for the structural solve
- Reducing the grid size

4.3.1 Parallelization

Parallel codes have been state of the art for numerical analysis for years . As a legacy code, SIMMER III was originally developed as a serial program. Past contributors have implemented cyclic multithreading , but SIMMER remains fundamentally a serial program. The parallelization of a program that was conceived as a serial program usually requires rewriting the majority of the codebase. Since I developed the finite element structural code from scratch and tools and libraries for parallel code are readily available, I decided to design it fundamentally as a parallel code. Thanks to PETSc [BAA+16] , Message Passing Interface (MPI) and METIS , the structural code uses state of the art parallel computing techniques to run on multiple nodes.

Figure 4.20 shows the result of the parallelization efforts for a sample problem with 216'000 degrees of freedom running on the *forHLR1* cluster of KIT. The use of parallel computing reduces the required computation time per time step significantly. And doubling the number of cores cuts the computation time in half. But even with 50 cores, the each time step requires about 50 seconds to solve. For use in production runs, this is impractical.

Since SIMMER III is a two-dimensional code, coupling it with a 3D structural code is an unnecessary waste of resources. In the scope of this work, I decided against putting further effort in the optimization of the three-dimensional structural code. But with regards to a future coupling with SIMMER IV, the capability to conduct 3-D analysis is an important feature of the structural code.

The tests suggest that the potential of parallelization is not yet fully utilized. The use of more cores should reduce the computation time further before the time required for thread-communication overcompensated the saving in time through the parallel treatment of the problem.

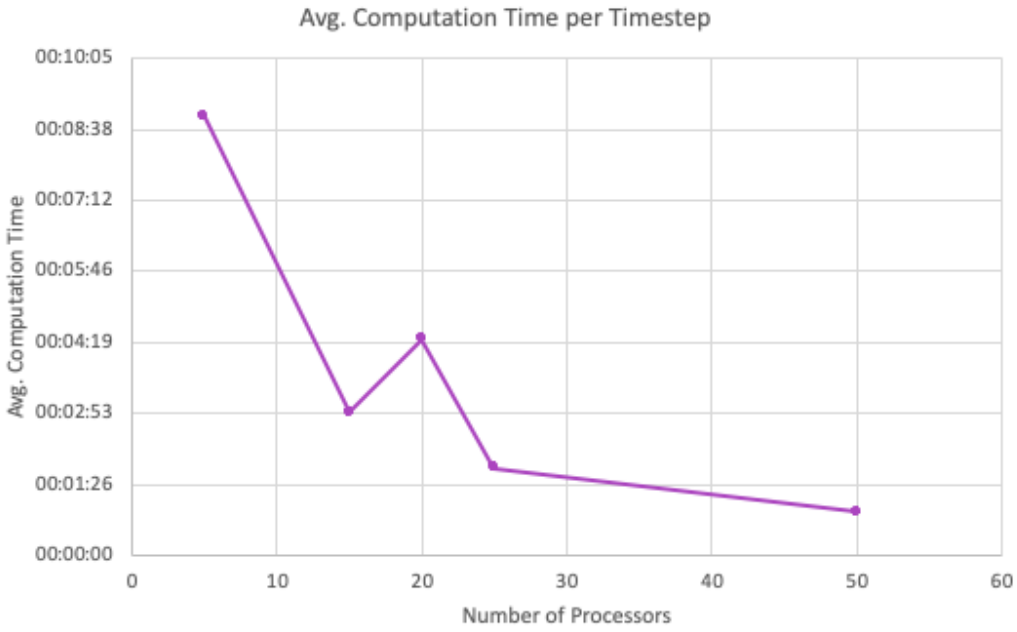

Figure 4.20: Average computation time per time-step for different numbers of processors of a sample problem with 12'000 hexahedral elements and 216'000 degrees of freedom.

5 Use Case for Coupled Code

The intent of developing a FSI-extended mechanistic severe accident code was to improve the reliability of analysis by accounting for the structural response during the expansion phase. In chapter 3, I presented the general approach and described in detail the implementation of structural analysis and coupling. In chapter 4, I applied structural and coupled code to a selection of reference problems. Doing so, I verified the correct implementation and proved the validity of the approach for fast transient FSI problems in cylindrical vessels.

But all considered cases until here are model problems and do not reflect the actual incident sequence of a post-CDA expansion phase. To prove the usefulness of the coupled code for actual HCDA analysis, and numerically investigate the impact of the structural response, I apply the code to more realistic cases. As reference, I chose a series of EP analysis conducted by KIT in the context of a parameter study for the expansion phase in a generic research SFR. Figure 5.1 shows a schematic representation of the reactor.

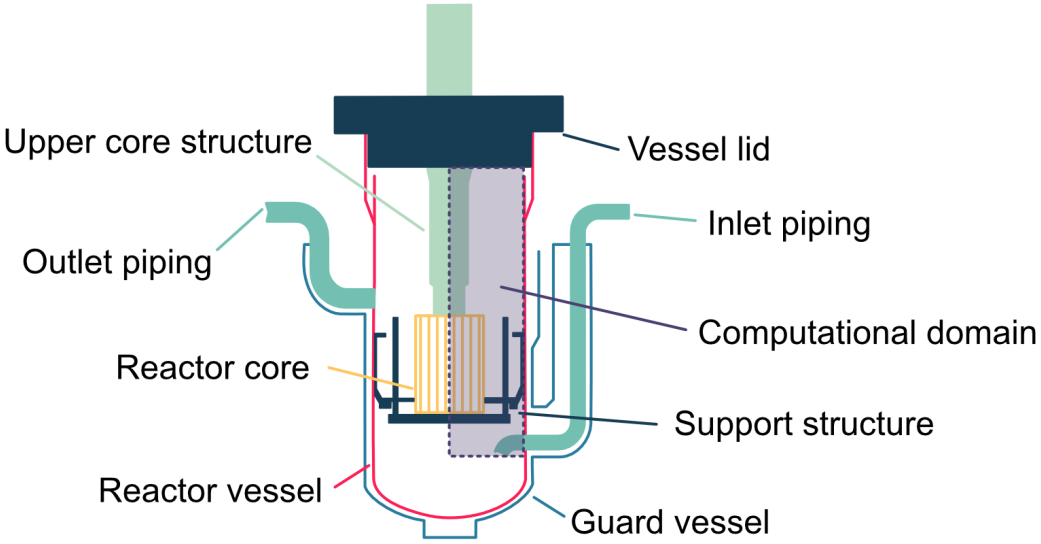

Figure 5.1: Schematic representation of a generic research SFR facility with computational domain.

This chapter discusses the context and setup of the use cases, and presents results illustrating the effect of structural coupling to the analysis result. I will first explain the motivation and context for the original study and the resulting assumptions leading to boundary and initial conditions. Then, I will detail the numerical model of the structural domain. A section presenting and discussing the results will conclude this chapter.

5.1 Assessment of ULOF-Induced Post Disassembly Expansion Phase in an Experimental SFR

In 2014, KIT conducted a parametric study on the expansion phase in a medium sized research SFR [FGG+15]. The intent was to develop a Phenomenological Relationship Diagram (PRD). The study included more than 100 SIMMER-III runs with varying initial configurations and represents one of the most comprehensive investigations to date. A selection of those runs serve as use cases for the newly developed coupled SIMMER code. In his section, I will give a quick overview of the study and present the relevant reference cases.

After a fatal initiative incident substantially damages a reactor core, the disruption can propagate further. As mentioned in section 1.1.4 this can lead to a disassembly of the entire core region during the so called transition phase of a hypothetical severe accident. The changed arrangement can lead to a prompt critical configuration resulting in a power excursion that expels molten fuel and steel into the coolant pool. The resulting expansion phase can challenge the integrity of the reactor vessel.

The reactor configuration at the onset of the expansion phase is generally the result of the preceding transition phase. The workflow for hypothetical severe accident analyses commonly follows this sequence. In this case, the initial conditions for the expansion phase analysis are idealized configurations. I chose three of those configurations as reference cases for the coupled SIMMER code with the intent to assess the capabilities of the new code and the importance of the structural response during an expansion phase.

The basic configuration for all cases is the same, but the initial temperature of the fuel varies between 4000K, 6000K and 8000K. To investigate the impact of structural behavior, I repeat the analysis of three reference cases with a flexible structure. Table 5.1 gives an overview of all cases.

Table 5.1: Overview of cases with related initial conditions and structural behavior model.

Case	T_{fuel} $[K]$	M_{fuel} $[kg]$	E_{fuel} $[MJ]$	Structure
A01-X1R	4000	5280	9576	rigid
A01-X1E	4000	5280	9576	elastic
B01-X1R	6000	5280	14'954	rigid
B01-X1E	6000	5280	14'954	elastic
B01-X1P	6000	5280	14'954	elasto-plastic
C01-X1R	8000	5280	19'311	rigid
C01-X1E	8000	5280	19'311	elastic
C01-X1P	8000	5280	19'311	elasto-plastic

The following section 5.1.1 discusses the three reference cases in detail, before sections 5.2 and 5.3 present setup and results of the coupled cases.

5.1.1 Rigid Reference Cases with Original SIMMER-III

The parametric study of the expansion phase in the generic medium sized SFR reactor [FGG+15] contains three exemplary cases. Below, I will detail the initial configurations, involved assump-

tions and results of those three cases to which I will later apply the coupled SIMMER code. Figure 5.2 shows the SIMMER model of the research SFR facility presented above in figure 5.1.

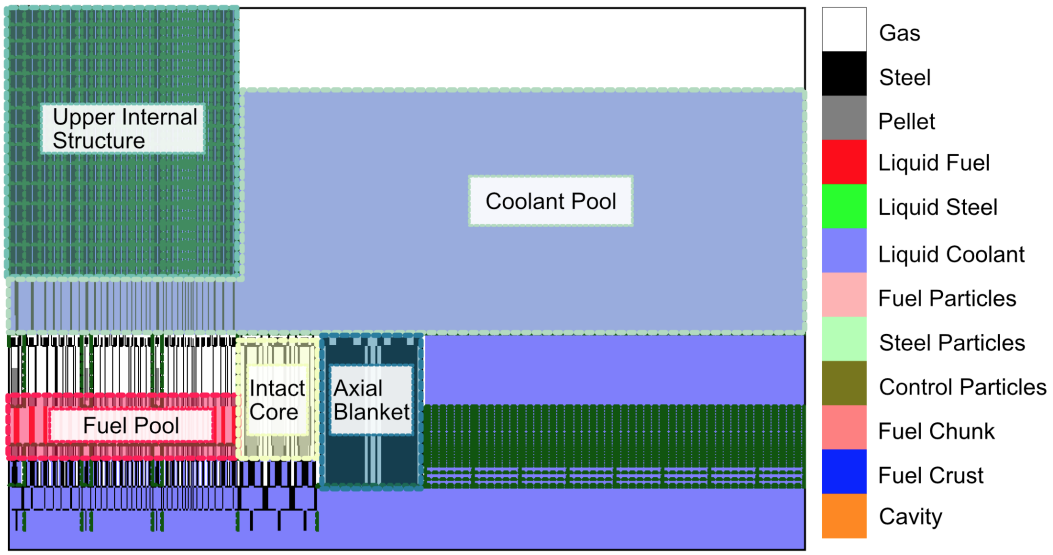

Figure 5.2: Depiction of the SIMMER model for the analysis of case B01-X1R in initial configuration.

Some general assumptions apply to all three reference cases. The following sections lists those common premises.

Common Assumptions for the Rigid Reference Cases

The parametric study of the expansion phase in the research SFR was not based on a preceding transition phase analysis. Instead, it relies on some key assumptions for the initial configurations of all runs. Those assumptions translate to specific boundary and initial conditions in the numerical model.

Crust Formation The formation of crust on the extremities of the core region is a common phenomenon during the transition phase. Molten corium slowly travels towards cooler regions where it solidifies and forms plugs. Those plugs isolate the molten fuel pool from the coolant and are more pronounced on the bottom of the core region.

The barrier on the lower core boundary prevents downward flow and promotes an upwards discharge of molten fuel and steel from the core region into the coolant pool. In the numerical model, virtual walls represent those fuel plugs and prevent movement of molten fuel towards the lower axial and radial blanket.

Axial Blankets Both upper and lower axial blanket appear with intact geometry in the SIMMER-III model, but contain no liquid sodium. The temperature of the upper axial blanket structure is 1250K.

Fissile Core Zone The model assumes a molten fuel pool of cylindrical shape with a uniform temperature in the fissile zone. Sodium is absent in the core region which contains mainly fission gas. Apart, of course, from the molten fuel. The fission gas pressure amounts to 3.85 MPa resulting from an assumed temperature equal to fuel solidus. Cladding material only appears at the core region boundaries in the form of solidified plugs.

Upper Internal Structures The Upper Internal Structures (UIS) consist mainly of instrumentation and control rod guides. The computed pressure loss for radial flow through the structures depends on orifice coefficients deducted from literature. Axial flow resistance in the UIS stems from SIMMER's standard models.

Together, those assumptions form the common basis for modeling the idealized initial conditions of the reference cases. The cases differ exclusively in the temperature of the molten fuel in the core region, leading to a diverging evolution of the expansion phase. The following section discusses the distinct features of each case in detail.

Distinct Features of the Reference Cases

The fundamental assumptions, discussed in section 5.1.1, are the same for all reference cases. The key difference between the three cases is the initial temperature of the molten fuel in the core region. In all instances, the fuel pool has a uniform temperature and a cylindrical shape at the beginning of the analysis.

Table 5.1 summarizes the relevant initial fuel temperature, total mass, and energy for cases A, B, and C as conceived and analyzed in [FGG$^+$15]. All reference cases assume a rigid structure, applying the uncoupled SIMMER-III code.

Case A, with 4000K initial fuel temperature and 0.2MPa resulting vapor pressure , represents the lowest temperature at which to expect a release of mechanical work. The 6000K of Case B imply a significant preceding power excursion. Case C's 8000K are the result of an academically high energy release and represent the most severe scenario considered.

Through the initial fuel temperature, the three reference cases differ in their respective severity. From case A as the mildest to case C as the most severe. The next section will expose, that the evolution of the resulting expansion phase differs considerably.

Results of the Uncoupled, Rigid Reference Cases

Three reference cases, borrowed from an extensive parameter study conducted by KIT in 2014 [FGG$^+$15], form the basis for assessing the effectiveness of the coupled code with the help of a real world problem. The cases encompass a representative spectrum of energy released by nuclear fission as the result of a re-criticality in the disrupted core. This section will concentrate on the results of their analysis with the unmodified, original SIMMER-III code. It illustrates the differences in the expansion phase evolution between case families A, B, and C.

The mechanical work release varies significantly among the cases. Figure 5.3 illustrates the effect on the fluid transient in the vessel. Comparing the maximum heights of the accelerated sodium slugs at the respective times. Figure 5.4 compares the amount of mechanical work between cases A01-X1R, B01-X1R and C01-X1R directly.

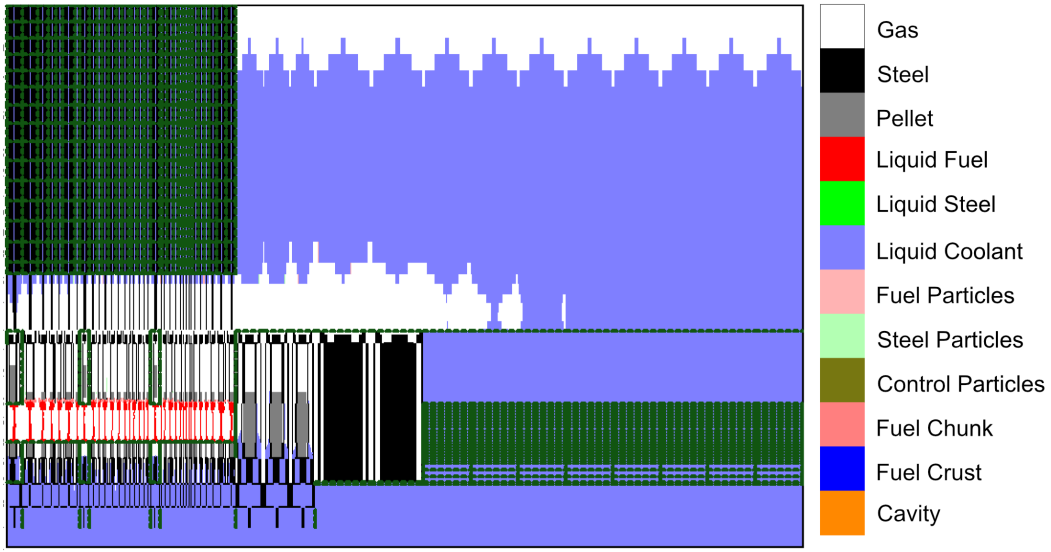

(a) A01-X1R at t=0.21s

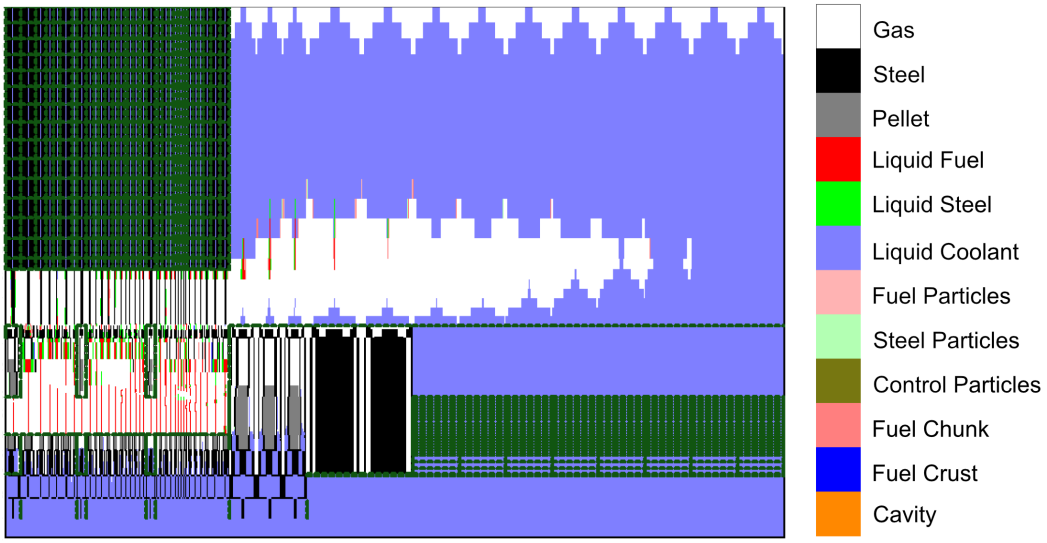

(b) B01-X1R at t=0.41s

Figure 5.3: Phase plots at time of highest point of sodium slug for reference cases with the unmodified SIMMER-III code.

Figure 5.3 shows the reactor configuration at time of the highest coolant level which coincides with the time of the pressure peak in the covergas. The phase plot shows the material distribution in an axisymmetric representation from the reactor's axis of revolution on the left side of the picture towards the vessel wall on the picture's righthand side. In all three pictures, the vapor bubble resulting from FCI extends into the coolant pool.

The pyramid-like shapes at interface between coolant pool and cover-gas are the result of SIM-

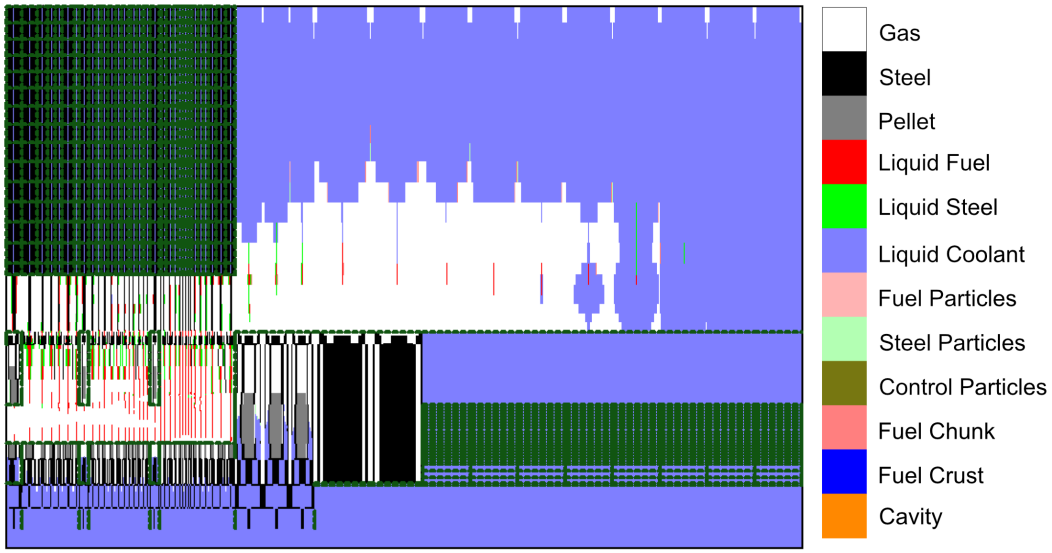

(c) C01-X1R at t=0.12s

Figure 5.3: Phase plots at time of highest point of sodium slug for reference cases with the unmodified SIMMER-III code (cont.).

MER's post-processing depiction. The volume fraction of coolant in each cell is depicted by a light blue area fraction in the plot. The phase plot depiction resembles a symetric bar-chart in each cell. The colored area contains no information on the interface orientation or the location of each phase inside the cell.

With an initial temperature of 4000K, the fuel discharge into the sodium pool for case A01-X1R is moderate. The phase plot in figure 5.3a displays no visible amount of fuel in the coolant pool region at the time of maximum covergas conpression. The moderate discharge provokes a comparatively soft expansion phase. The arising vapor bubble marginally lifts the sodium pool upwards before dispersing as shown in figure 5.3a. Figure 5.4 clarifies the marginal amount of mechanical work release compared to case families B and C.

Case B01-X1R produces a more violent vapor explosion as the result of more molten fuel at higher temperatures ejected into the coolant. Figure 5.3b shows liquid fuel and steel inside the coolant pool at the upper front of the rising vapor bubble as well as resolidified fuel particles.

The main expansion event follows a preceding, lighter one. The maximum height of the sodium slug and with it the peak pressure in the cover gas occurs later in relation to case families A and C. Figure 5.4 reflect this situation well.

Unsurprisingly, case C provokes by far the most violent reaction. Figure 5.3c shows more motlen fuel has left the core region and dispersed further into the coolant pool region. The resulting release of mechanical work potential during the FCI is significantly larger than for case families A and B.

The emerging vapor bubble accelerates the sodium slug rapidly, wich impacts the vessel lid after 0.12 seconds as shown in figure 5.3c. The mechanical energy release dwarfs those of case families A and B at around 120 MJ.

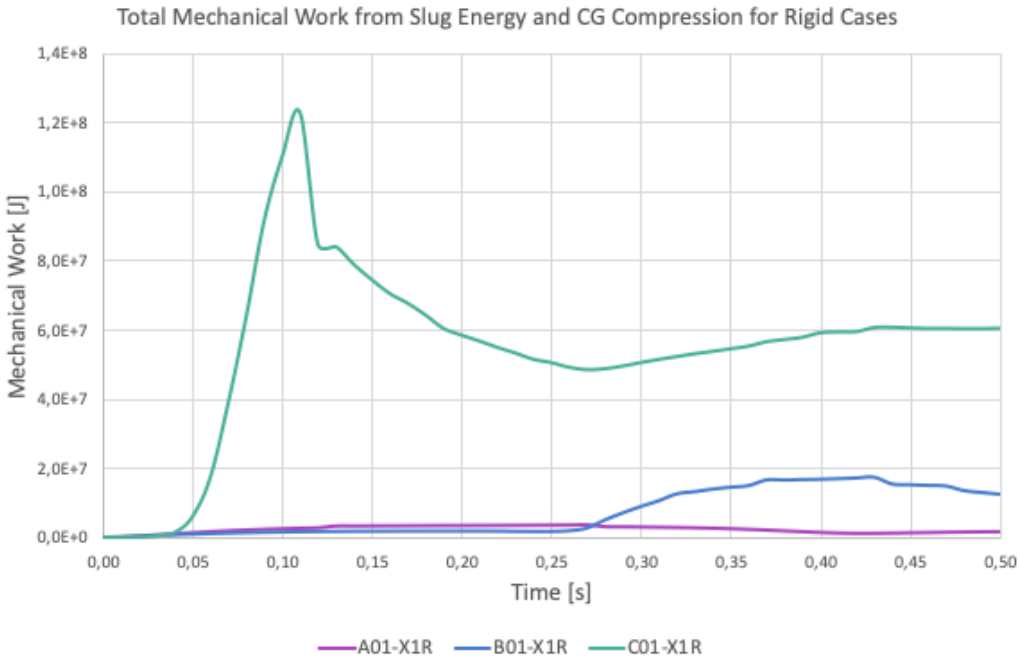

Figure 5.4: Mechanical work as sum of sodium slug kinetic energy and compression work in covergas for rigid reference cases of an expansion phase in a generic research SFR.

The comparison of reference cases A, B and C with rigid vessel wall illustrates the respective severity of the considered idealized initial conditions. The impact of initial fuel temperature on the resulting mechanical work release became clear. In the following, I will present the setup for the coupled cases including and discuss the impact of the structural response on the mechanical work release.

5.2 Coupled Use Cases Setup

To determine the impact of structural feedback on the evolution and outcome of an expansion phase, I revisited reference cases with the newly developed coupled code. The extended SIMMER includes a structural FEM code and a model to represent a moving boundary in the structured SIMMER grid. Conduction a coupled analysis requires two preparatory steps. First, modifications to SIMMER and its input file. And second, the setup of a structural analysis including boundary- and initial conditions.

I will first discuss the modifications to SIMMER below in section 5.2.1 before moving on to the structural setup.

5.2.1 SIMMER Setup for the Coupled Use-Case

The introduction and treatment of the immersed, moving boundaries requires modifications to SIMMER. Apart from extending the source code as described in chapter 3, model parameters and SIMMER mesh require adjustments as well.

The input files for the coupled and the standalone SIMMER analysis differ in some minor details. Those changes are necessary to introduce the moving boundary in the structured SIMMER grid and to ensure the stability of the pressure iteration procedure.

The number of necessary modifications is manageable and condensed in the following list:

- Additional cell column in radial direction
- Increased radial extent of boundary cells
- Increased minimum vapor volume fraction to 2E-2
- Set minimum coolant pressure to 100 Pa
- Prevent fluid motion for solid volume fraction >99.99%

Additional Cell Column in Radial Direction

Plastic deformation of the vessel wall might lead to a significant displacement of the immersed boundary. To accurately represent the entailed geometry changes while preserving the mesh resolution of the surrounding grid I introduced an additional columns of cells. The radial extent of those cells is 0.1 m.

In the beginning of the analysis, those cells are voided; respectively, they are occupied by an inert filler material that prevents fluid from entering [1], as explained in section 3.3.2. Once the vessel wall passes the cell boundary, they fill with fluid.

Increased Radial Extent of Boundary Cells

Representing the moving fluid/solid boundary inside a SIMMER cell works best when the interface during steady-state operation is inside the cell rather than at the border. This prevents frequent jumps of the immersed vessel wall over cell boundaries and the resulting very high / low inert material volume fractions. Since the vessel itself should have the same dimensions as in the standalone SIMMER case, I increased the extent of the boundary cell to position the immersed vessel wall in the cell center at the beginning of the analysis.

The cell now containing the immersed boundary has a new radial extent of 0.37 m.

[1] The right canwall no-flow area volume fraction (ALPNFK3) is equal to 1

Set Minimum Vapor Volume Fraction to 0.02

As mentioned in section 3.1.5 , increasing the minimum vapor volume fraction in each cell can improve the stability of the pressure iteration in SIMMER III. To prevent divergence of the code, I increased the variable *ALPHA0* [2] to 0.02 from its default value of 0.01. This is a preemptive step and may not be required for all cases. The moderate reaction of cases A and B suggest that they could be treated without modifying ALPHA0. But I kept the same value for all analysis to provide a more comparable setup between all cases.

Set Minimum Coolant Pressure to 100 Pa

The quick acceleration of the vessel wall can cause cavitation in the coolant region close to the immersed interface, as mentioned in section 2.2.4. This behavior becomes particularly problematic when the liquid is close to the saturation line. To prevent numerical instabilities in the EOS iterations, I restricted the minimum coolant vapor pressure. This proved to be the remedy for convergence failures in the validation case presented in section 4.1.

Prevent Fluid Motion for Solid Volume Fraction >99.99%

By default, SIMMER prevents fluid motion in all cells with a solid volume fraction larger than 90 %. When the immersed vessel wall passes from one mesh cell to another, such large solid (or inert material) volume fractions can occur in a coupled analysis. The coolant needs to enter the new immersed boundary cell immediately, filling the vacated volume. This cannot happen if the code prohibits fluid motion inside the cell. Setting a higher threshold resolves this issue.

This concludes the modifications to the SIMMER input file. I applied the learnings from the coupled analysis presented in section 4.2 to ensure the stability of the coupled code. Keeping in mind, that some of the instabilities in the validation case occurred as a result of the EOS model, not all those modification might strictly be necessary in this case. The sodium EOS model of SIMMER is more sophisticated than that of water. And at around 400 °C, the fluid state is sufficiently far from the triple point. I did not extensively study the impact of minimum temperature and vapor pressure of sodium on the stability and results of the coupled code. This might be and interesting subject for future studies. The idea was to ensure convergence for the coupled cases, prove the overall concept, and produce results comparable to the uncoupled cases.

5.2.2 Structural Analysis Setup for the Coupled Cases

The coupled code relies on a FEM model to determine the structural feedback at every time-step. To produce reliable results, the structural model needs to adequately reflect the real world conditions. The key ingredients to ensure this are a computational grid of suitable detail and resolution, and adequate boundary conditions. Section 4.1 proved the correct formulation of the FEM implementation itself. It also discussed the limitations inherent to the method applied. This section concentrates on the structural model for the coupled cases of an expansion phase analysis in the research SFR model.

[2] *ALPHA0* is the SIMMER variable name for the minimum vapor volume fraction.

The first part describes the general geometry and computational grid of the numerical model.

Geometry of the Structural Model

The reference cases consider a subsection of the entire reactor. To keep the results of the coupled cases comparable, I kept the SIMMER computational domain as close to the reference cases as possible. The structural model hence had to correspond to the SIMMER mesh. I developed a model that did not pass domain boundaries of the SIMMER grid in a significant manner and could be represented as a 2D axisymmetric geometry.

In the SIMMER analysis of the reference cases, the sodium slug impacts the upper domain boundary which brings it to a complete halt. Given this circumstance, it makes sense to chose the upper boundary of the SIMMER grid as the position of the vessel lid. The lids of research SFRs are typically heavily built and their thickness ranges up to 3700 mm [HTIY85]. This suggests a highly rigid structure. I hence refrained from modeling the lid in detail and assumed the upper boundary of the original SIMMER grid as the lid's infinitely rigid representation.

To ensure comparability between reference- and coupled cases, I placed the flexible vessel wall at the outermost cell of the SIMMER grid for the original (uncoupled) reference cases. The generic SFR's core rests on a solid steel plate. In the SIMMER models, solidified steel plugs clog the flow channels between the lower sodium plenum and the core region as mentioned in 5.1.1. The plate itself can be assumed rigid and the SIMMER model allows no fluid motion or pressure equalization between core region and lower part of the mesh. I hence also excluded the lower vessel part from the numerical model.

This results in a cylindrical shaped vessel with an inner diameter of 6'200mm. A wall thickness of 50 mm is typical for vessels of loop type medium sized SFRs operating und atmospheric pressure [HTIY85], which I adopted for the numerical model.

Structural Grid for the Coupled Cases

Choosing an adequate mesh for the FEM analysis is paramount to the accuracy and reliability of the results. For a simple geometry as in this case, the challenges are moderate. As a general rule of thumb, the structural grid should comprise at least two elements along the smallest dimension of the geometry. Elements should not be too distorted to rule out numerical instabilities, and the mesh resolution should increase in areas where strong gradients are likely to appear.

With those indicators in mind, I constructed a triangle mesh with a minimum of 5 elements across the wall thickness. Figure 5.5a shows the upper part of the grid which is representative for the entire height of the mesh. With such a simple geometry, the only real challenge is to ensure that the global and local mesh resolution is sufficient to ensure reliable results.

I conducted a mesh convergence study to ensure an acceptable mesh resolution for the structural domain.

Structural Mesh Convergence An inadequate resolution of the structural mesh for the FEM analysis can lead to inaccurate results. Mesh convergence studies are a common practice to rule out the possibility for this issue by progressively refining the mesh until results no longer differ between two refinement steps.

In this case, I compared two structural grids in varying resolution to dismiss grid-size as a possible origin for inaccuracies in the solution. The coarser of the two consists of 4'924 triangle elements and the finer of 13'892. Since the results of a test run did not differ between both refinement levels, I considered the mesh to be sufficiently fine. The code ran reasonably fast with the coarser of the two meshes, so I did not proceed to find an even coarser, still acceptable mesh.

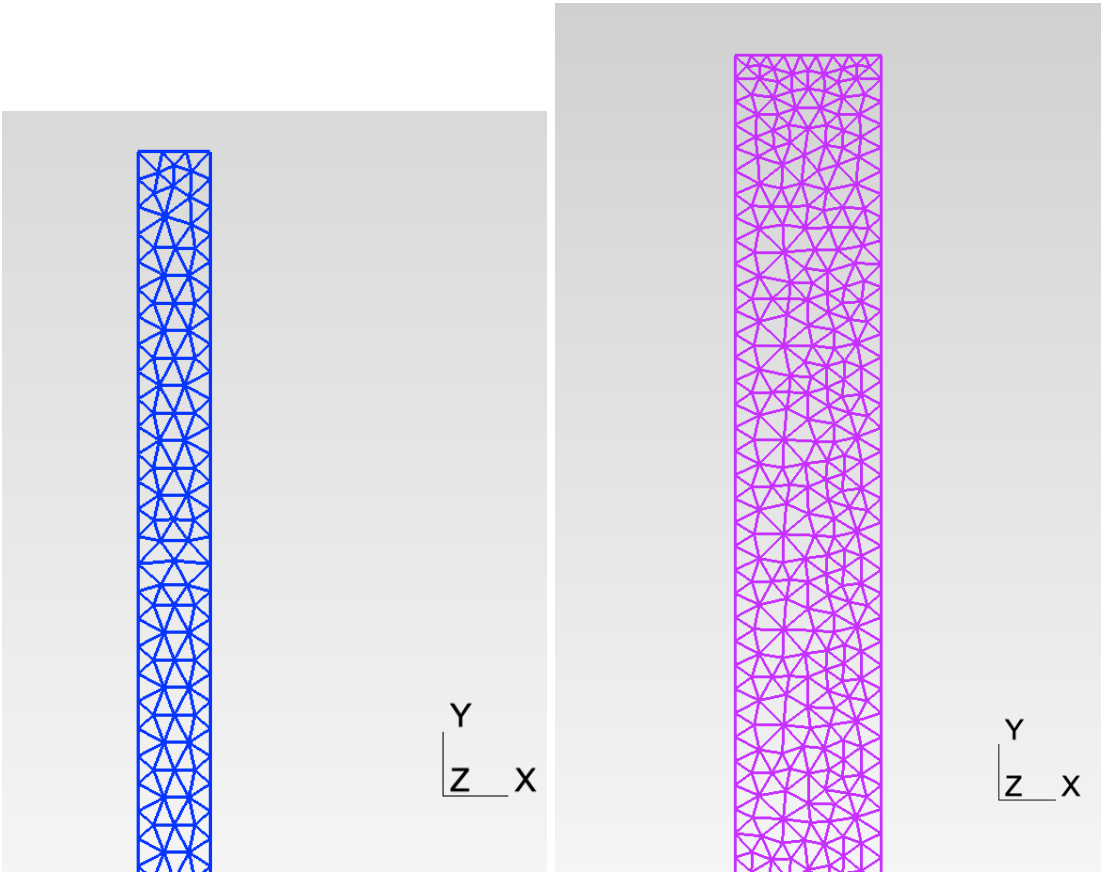

(a) 4'924 triangles (b) 13'892 triangles

Figure 5.5: View of the upper end of two structural grids for the generic mediumösozed SFR use case of the coupled code with varying refinement.

Material Parameters for the Coupled Cases

As material I chose 316L stainless steel at 550°C reference temperature. Material data such as hardening parameters at the relevant temperature and different strain rates are readily available [AM80]. And this grade of stainless steel is commonly used as structural material in nuclear

fast reactor applications. Section 3.2.8 details the material model and the multilinear hardening parameters.

Boundary Conditions in the Structural Domain for the Coupled Cases

I assumed that the vessel hangs down from the top flange, which bears the primary axial load of the entire reactor's weight. This is a typical design for sodium cooled reactor systems. At the top of the cylindrical vessel, I hence assumed that no movement relative to the support structure occurs. Therefore, with the aid of a Dirichlet boundary condition, I restricted movement both in axial and radial direction at the upper boundary of the discretized cylinder.

The structural model, just as the SIMMER model, ends right below the reactor core. The core structure rests on a thick support plate fixed to the vessel wall. The support plate in combination with the secondary support structure below the vessel are the reason why I do not expect notable deformation in radial direction. The weight of the core and pressure acting on the vessel bottom present a downwards force on the vessel wall. I assumed that the added inertia of sodium plus core will also prevent significant axial wall movement at the attachment point of core support plate and vessel. The Dirichlet Boundary Condition (BC) at the bottom end of the mesh hence also restrict movement in both radial and axial direction.

The one remaining relevant boundary is the inner surface of the cylinder – the fluid / solid interface of the coupled problem. Information on the current load at ech point on the inner boundary comes from the SIMMER analysis. Section 3.3 explains the procedure in detail.

This leaves us with three relevant boundaries for the two-dimensional axisymmetric structural model. The two fixed, upper and lower boundaries. And the inner, loaded surface.

This concludes the setup of the structural problem. Its geometry is a 2-D axisymmetric cylinder slab with an inner diameter of 6'200 mm and 50 mm wall thickness. The mesh consists of 4'924 triangles and was tested against a finer mesh to ensure adequate resolution. Dirichlet boundary conditions at the upper and lower end of the cylinder wall restrict movement in any direction. The current local pressure, obtained from the SIMMER analysis, acts as Neumann BC on the inner, wetted boundary of the wall. The used material is 316L stainless steel with a multi-linear hardening model for the elasto-plastic cases.

5.3 Results of the Use Cases

To investigate the impact of structural response on the evolution of an expansion phase, I analyzed three reference cases with rigid, linear elastic and elasto-plastic material behavior. The analysis doubled as crucial test for the newly developed coupled code to test capabilities and limitations.

To compare results between cases, I choose four relevant physical quantities presented below.

5.3.1 Relevant Physical Quantities

The climax of an expansion phase is the sodium slug's impact on the vessel lid, challenging the structural integrity of the entire vessel.

The pressure difference between the vapor bubble around the reactor core and the upper gas plenum accelerates a portion of the sodium upwards. The *kinetic energy* in the sodium slug at any moment is:

$$E_{kin} = \int_{\Omega} \rho_{Na} \frac{v_{Na}^2}{2} d\Omega \tag{5.1}$$

On its way up, the advancing front compresses the cover gas. The resulting opposing force reduces the momentum of the advancing slug. This equals a conversion of kinetic energy of the slug through compression work in the upper gas plenum. The *compression work* equals:

$$W_{compr} = -\int_{V_0}^{V_f} p_{cg} dV_{cg} \tag{5.2}$$

Where V_0 and V_f are initial and final volume of the cover gas respectively.

The combination of both quantities, compression / expansion work potential in the cover-gas and kinetic energy of the sodium slug, is what challenges the vessel integrity. The resulting sum is what I call the *mechanical work*, adopting the terminology used by [FGG+15]:

$$W_{mech} = W_{compr} + E_{kin} \tag{5.3}$$

Another important quantity is the mechanical work of the expanding vapor bubble. It allows a direct comparison of the total amount of energy converted to mechanical energy in all cases. Since work also goes into deforming the structure, the mechanical work from equation 5.3 should be lower for the cases with flexible structure versus the rigid cases. A differing *bubble work potential* would suggest that the flexible structure influenced the conversion from thermal to mechanical energy through the FCI mechanism. The bubble work potential is defined as:

$$W_{bubble} = -\int_{V_0}^{V_{fin}} p_{bubble} dV_{bubble} \tag{5.4}$$

To obtain all quantities, some post-processing steps are necessary. The first step is building a stencil to discriminate between vapor bubble, cover gas and sodium slug.

Bubble and Cover Gas Stencil The first step is to identify which cells of the SIMMER analysis to include in the computation of the relevant quantity. I formulated a definition for the vapor bubble and Cover Gas (CG) region, relying on relative position of each cell in the reactor, current time, and vapor / gas volume fraction. From that, I construct a stencil to conveniently select relevant cells by a simple operation.

To define the stencil, I create a binary field that takes the value 1 wherever the gas volume fraction is bigger than a threshold of 20%. Everywhere else, the field has the value zero. We can then include cells simply by multiplying any cell variable with the binary stencil field. Figure 5.6 shows representations of those binary fields.

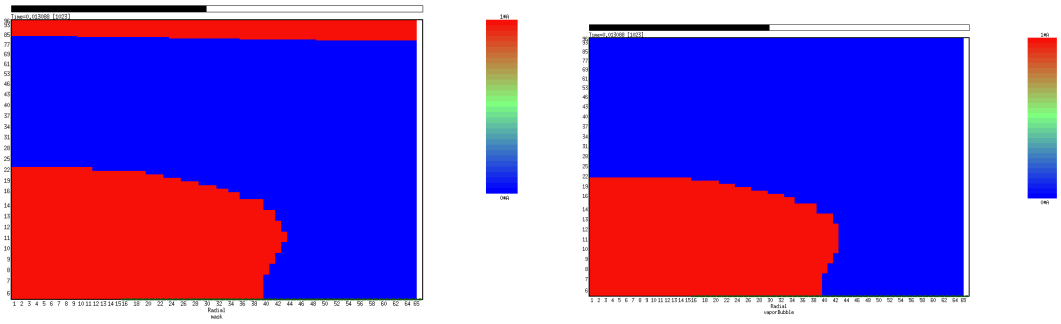

(a) Stencil including CG and bubble.

(b) Stencil with only bubble.

Figure 5.6: Visualization of stencils used to discriminate between bubble region, cover-gas and sodium slug.

The volume fraction criterion alone includes all gas-filled cells and does not differentiate between expanding vapor bubble and upper gas plenum. A second criterion helps to exclude the upper gas plenum from the calculations. Or the bubble region respectively. For simplicity's sake, I chose a simple axial upper limit above which all gas-containing cells are considered to be part of the upper gas plenum. The limit changes in time since, depending on the case, the expanding vapor bubble ventures into the region that contains the upper gas plenum in the beginning of the analysis.

Currently a simple binary step-function describes the movement of the upper limit. The method requires some manual action in defining two upper limits (at t_start and t_end) and a *switching time* at which the axial limit changes its value. The user needs to determine those three parameters with a quick visual analysis after the completion of the solver run. He then needs to adapt the parameters in the post-processing script file.

Calculating the Relevant Quantities The stencil allows to separate the relevant from the irrelevant regions for averaging operations. Calculating the necessary quantities now is straight forward. I will present the procedure for the mechanical bubble work as an example below.

The total bubble volume is the sum over the volume of all bubble cells, or:

$$V_{Bubb} = \sum_{i}^{N} V_{cell\ i} F_i \tag{5.5}$$

where V_i is the volume of cell i and F_i is the the discrete stencil function evaluated for cell i.

I determine the mean pressure inside the bubble with a volume weighted approach:

$$p_{Bubb} = \frac{1}{V_{Bubb}} \sum_{i}^{N} p_i V_{cell\ i} F_i \tag{5.6}$$

All that is left to do is to integrate bubble pressure over bubble volume to determine the mechanical work release. I chose a numerical integration scheme using the midpoint rule. The total mechanical energy released at time t is defined by:

$$W_{mech}^{t} = W_{mech}^{t-1} + \frac{p_{Bubb}^{t} - p_{Bubb}^{t-1}}{2} \left(V_{Bubb}^{t} - V_{Bubb}^{t-1} \right) \tag{5.7}$$

The post processing routine presented in this chapter allows to deduct comparable quantities. I applied it to all the cases presented to examine different behaviors of the rigid vs the linear elastic and elasto-plastic cases. The following sections show the results and illustrate the characteristics of each case.

5.3.2 Low Intensity Case – 4000K

The low intensity case, with an initial fuel temperature of 4000K, shows a moderate amount of mechanical work release. Section 5.1.1 presented the rigid case in comparison to cases with other initial fuel temperatures.

In the following I will present the results for the rigid versus the elastic case. The stress state in the structure never surpasses the yield stress and no plastic deformation occurs. There is hence no plastic case to present.

Figure 5.7 compares the mechanical work (kinetic energy and CG compression) and the bubble work potential for rigid and elastic structure. The respective curves resemble each other in shape and values. The bubble work potential is bigger than the total mechanical work in acceleration of the sodium and CG compression work. The discrepancy stems from dissipative effects during acceleration and the dispersion of the vapor bubble in the coolant pool. The pronounced step in the mechanical work curves for both cases are an artifact of the stencil function.

Overall, the curves for the elastic case are slightly less pronounced. The maximum of mechanical work in the elastic case is 3.4 % smaller compared to the rigid case. This might be due to the temporal resolution of the SIMMER post-processing file. But figure 5.8 suggests that the lower overall mechanical energy can be attributed to both a slightly lower kinetic energy as well as to a lower compression work in the cover gas region.

The overall effect of the structural response in this case is insignificant. Neither did it influence the work potential of the expanding bubble nor the conversion of bubble work potential to mechanical work in the sodium slug and the cover gas. But the case illustrates nicely that for low energetic reactions, the flexible structure acts as expected and slightly dampens the effect of the fuel-coolant interaction.

For the lowest intensity case, the mechanical work potential is comparatively low. As expected, the structural response has an insignificant effect on the overall evolution of the expansion phase,

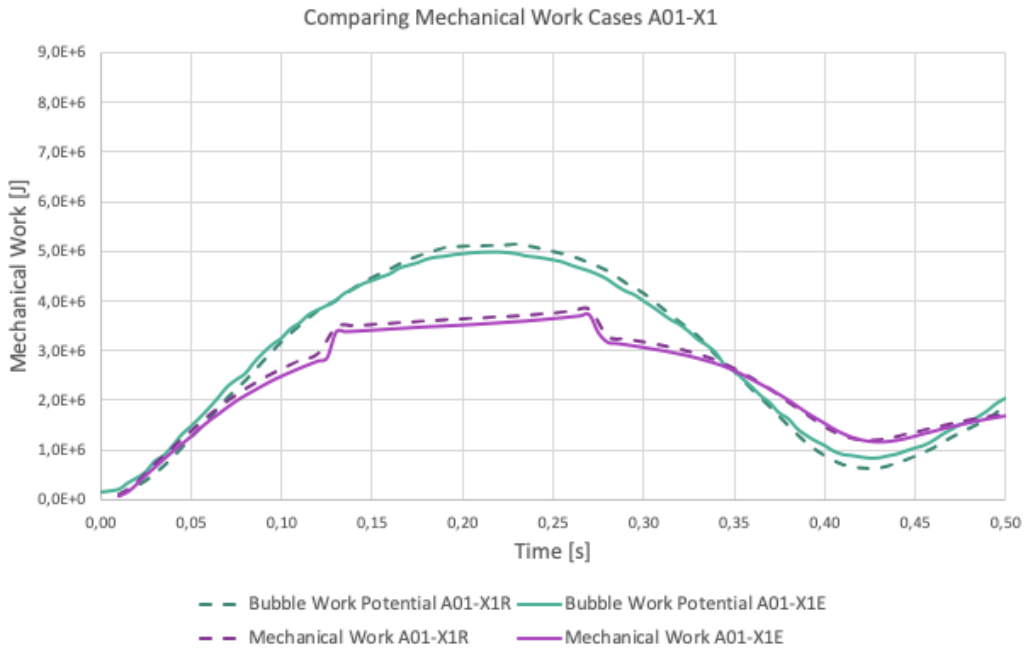

Figure 5.7: Comparison of the mechanical work and bubble work potential for rigid and elastic cases A01-X1R and A01-X1E respectively.

reducing the maximum mechanical work by 3.4%. This confirms, that the coupled code works as expected. In the following, I will present the results for the higher energetic cases where the structural response should play a more significant role.

5.3.3 Medium Intensity Case – 6000K

The 6000 K initial fuel temperature of the medium intensity case result in a more severe vapor explosion than the low intensity case. The larger amount of mechanical work release causes the sodium slug to rise higher, but it does not collide with the vessel lid. Instead, the cover gas cushions the impact.

In the rigid reference case, the peak of mechanical work release occurs with a slight delay. After a primary formation of a vapor bubble, the slug remains stationary until a second, more violent expansion sets in.

The following section presents the impact of structural response on the evolution of the expansion phase in the medium intensity case. The focus lies on the mechanical work as in section 5.3.2 for case family A01-X1X. For the medium intensity case, small amounts of plastic deformation occurred locally. The results therefore include the rigid, the linear elastic, and the elasto-plastic cases B01-X1R, B01-X1E, and B01-X1P respectively.

Figure 5.9 compares the vapor bubble work potential and the mechanical work from CG compression and kinetic slug energy among the cases. Surprisingly, both the bubble work potential and the mechanical work are higher for the flexible structure cases that for the rigid case.

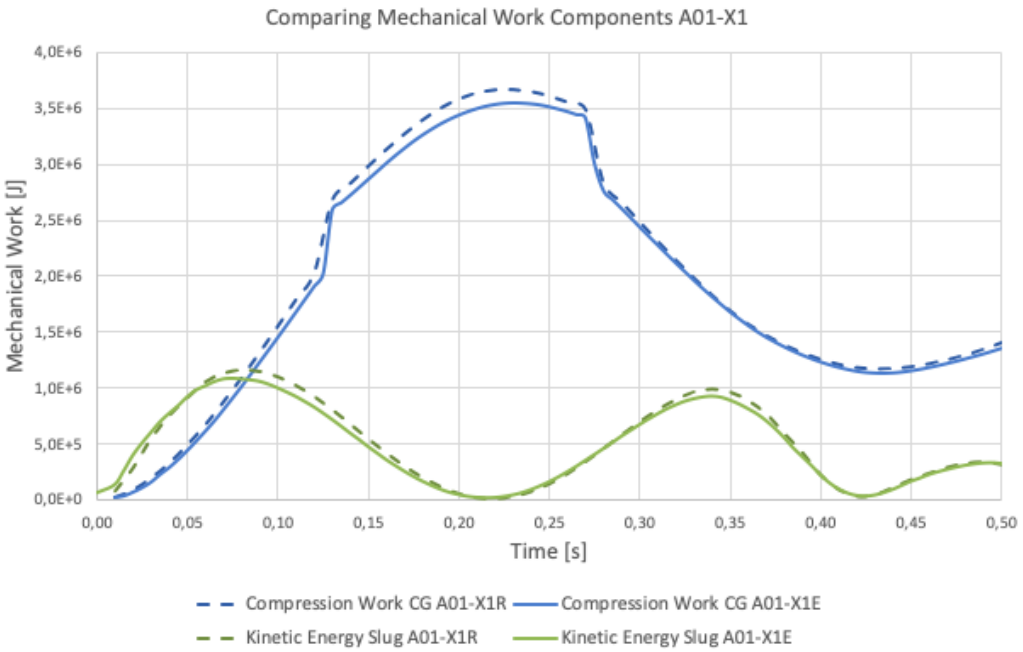

Figure 5.8: Kinetic energy and cover gas compression work over time for rigid and elastic cases A01-X1R and A01-X1E respectively.

For the plastic case, while the bubble work potential is more or less equivalent to that of the elastic case, the mechanical work is distinctly higher. Figure 5.10 suggests that already the kinetic energy of the slug is higher for the plastic case. This translates directly to a higher compression of the cover gas which decelerates the slug.

This is an intriguing circumstance. First of all, the significantly higher bubble work potential in the flexible structure cases hints at one of three sources. First more liquid fuel dispersed in the coolant region would. Second, a more higher fraction of liquid fuel in the core region interacting with the coolant. Or third, a more efficient conversion from thermal to mechanical energy.

Then, the plastic deformation of the vessel wall leading to a higher conversion from vapor bubble work potential to kinetic energy of the accelerated sodium slug.

The medium intensity case presented in this section shows that the coupled analysis works for more severe cases of expansion phases. But it also introduces new questions. Namely, the higher bubble work potential for the flexible cases compared to the rigid. And the higher kinetic energy of the sodium slug in the plastic versus the elastic structure case. The next section presents the results for the maximum intensity case.

5.3.4 High Intensity Case – 8000K

With 8000K initial fuel temperature, the case family C01-X1X represents the highest intensity scenario considered. For the less severe cases presented above in sections 5.3.2 and 5.3.3, the structural response had an observable effect on the mechanical energy release. But little to no

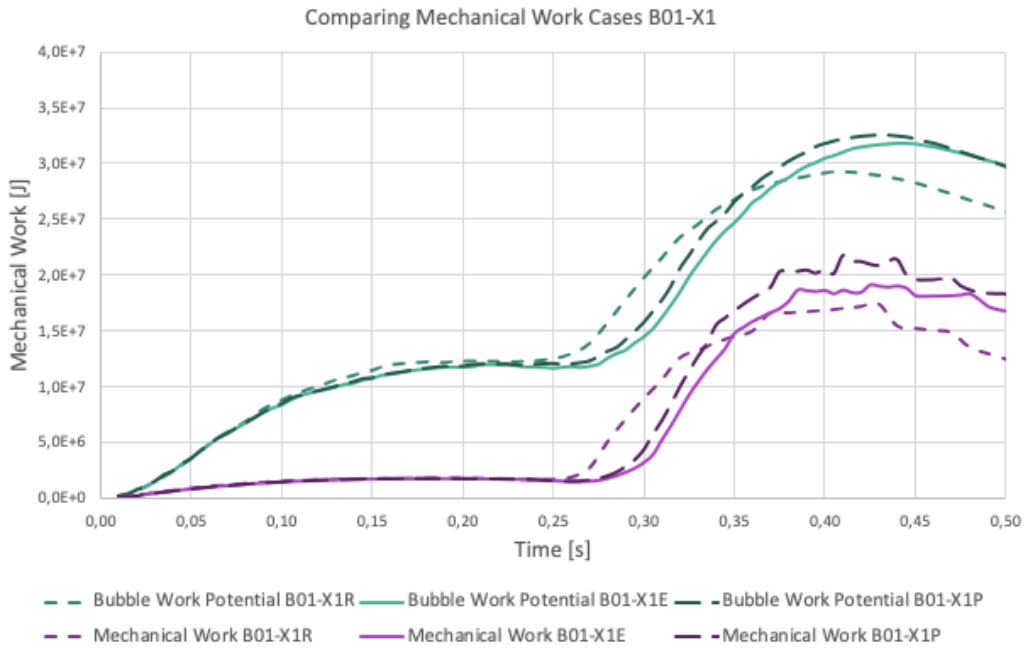

Figure 5.9: Comparison of the mechanical work and bubble work potential for rigid, elastic, and elastoplastic cases B01-X1R, B01-X1E, and B01-X1P respectively.

plastic deformation occurred. The intensity of the vapor explosion for the 8000K case on the other hand is so high, that it causes severe plastic deformation in the upper vessel region.

Severe Plastic Deformation in the High Intensity Case

Plastic deformation during the slug impact for case C01-X1P was so significant that the structural code failed to converge. Figure 5.11a shows the deformed state at the upper end of the cylinder just before abortion. Some steps later, the analysis failed as a result of self-intersecting elements. The equivalent plastic strain at this moment is already in the order of 1 – way beyond the limits of the applied infinitesimal strain model.

To prevent the solver failure, I constructed an alternative structural model. It features a progressively increasing wall thickness towards the upper end of the cylinder. The idea was to prevent stress peaks and resulting large localized plastic strains as seen in figure 5.11a. Unfortunately to no avail, as Figure 5.11b shows.

Even though the elasto-plastic coupled run stopped prematurely, the plastic deformation has an observable effect on the mechanical work release as presented below.

Mechanical Work Release in the High Intensity Case

The effect of the structural response on the mechanical work release are more pronounced than for the less severe cases. Figure 5.12 presents the chronological evolution of vapor bubble work

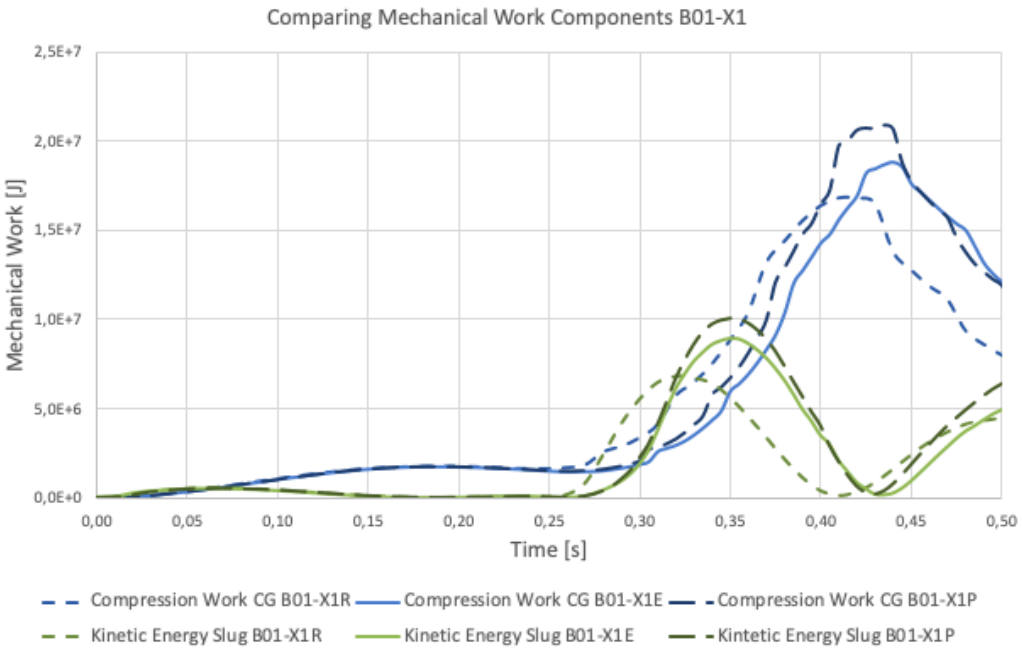

Figure 5.10: Kinetic energy and cover gas compression work over time for rigid and elastic cases B01-X1R, B01-X1E, and B01-X1P respectively.

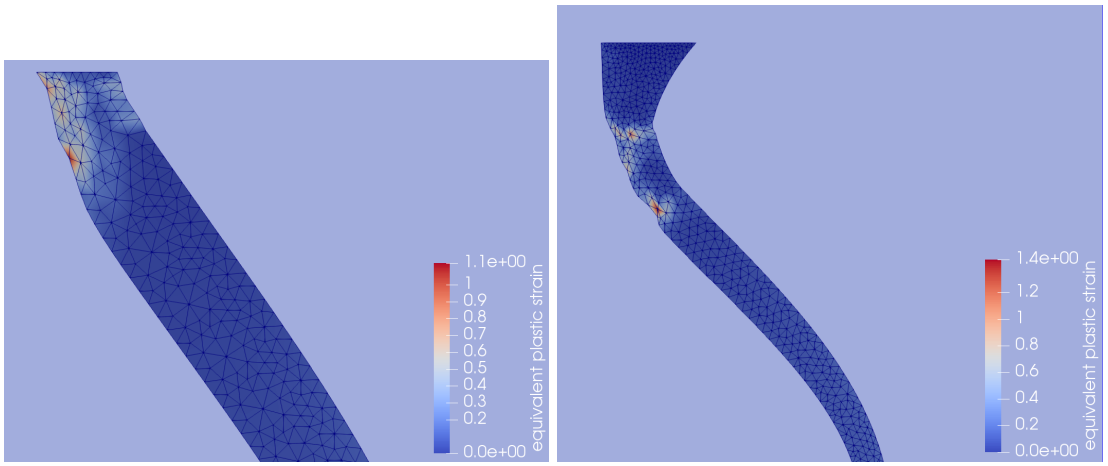

(a) Without flange. (b) With flange.

Figure 5.11: Distorted mesh with large equivalent plastic strain at the top of the SFR vessel at slug impact during elasto-plastic analysis of case C01-X1P.

potential and mechanical work from cover-gas compression and slug kinetic energy.

The maxima of vapor bubble work potential in the elastic and rigid case occur at the same time and are nearly identical in intensity. While in the plastic case the maximum occurs slightly

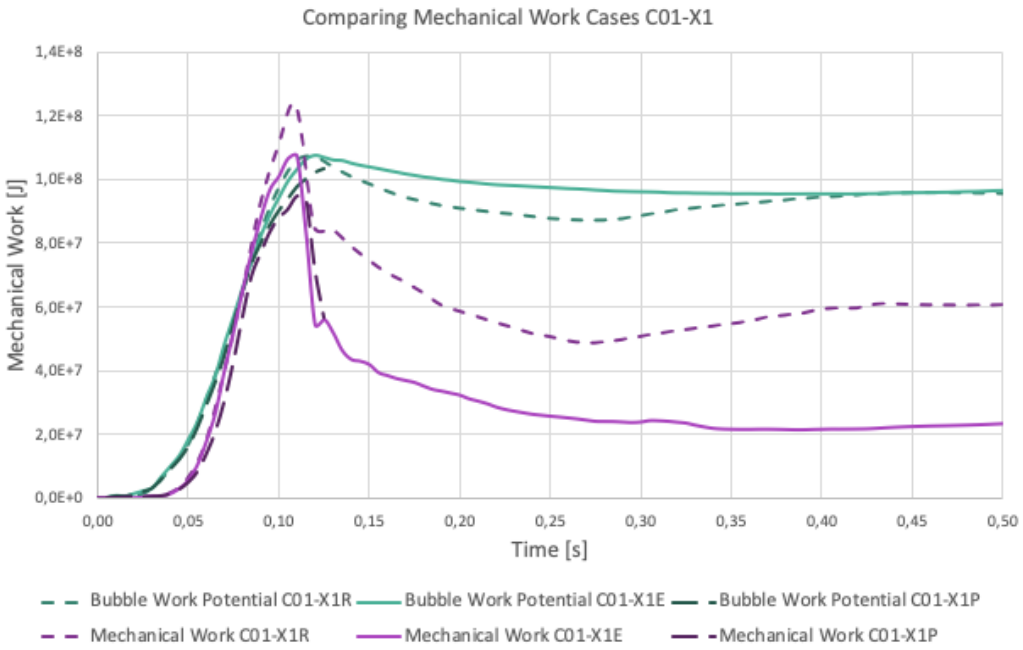

Figure 5.12: Comparison of the mechanical work and bubble work potential for rigid, elastic, and elastoplastic cases C01-X1R, C01-X1E, and C01-X1P respectively.

delayed and is by about 3% lower than in the rigid and the elastic case. This however, is not definite, since the elasto-plastic analysis stops right at the maximum. A later maximum, not captured by the aborted analysis, cannot be excluded.

The maximum combined mechanical work of cover-gas compression and kinetic energy of the slug reduces by 13% from rigid to elastic structure case. The elasto-plastic structural response reduces it again by 11% with respect to the linear elastic case. Or 22% with respect to the rigid case.

In the rigid case, around the time of slug impact, the mechanical work is bigger than the work potential of the vapor bubble. This is a consequence of the inner workings of the vapor bubble stencil in combination with a coarse transient resolution of the SIMMER post-processing file.

The maximum bubble work potential does not vary significantly between the cases. This indicates that the influence of the structural response on the FCI process for case family C is moderate. On the other hand, the total mechanical work of slug and cover-gas compression varies by about 10% from case to case. While the conversion from thermal to mechanical energy seems nearly unaffected by the structural response, it seems to have a considerable effect on the conversion from bubble work potential to the maximum amount of mechanical energy challenging the vessel integrity at the time of impact.

As figure 5.13 shows, the reduction of combined mechanical work in the flexible structure cases manifests itself in a visible reduction of the slug's kinetic energy. The deformation of the vessel wall under load absorbs part of the mechanical work potential of the expanding vapor bubble. Prior to slug acceleration, the vessel already shows a significant plastic deformation just above

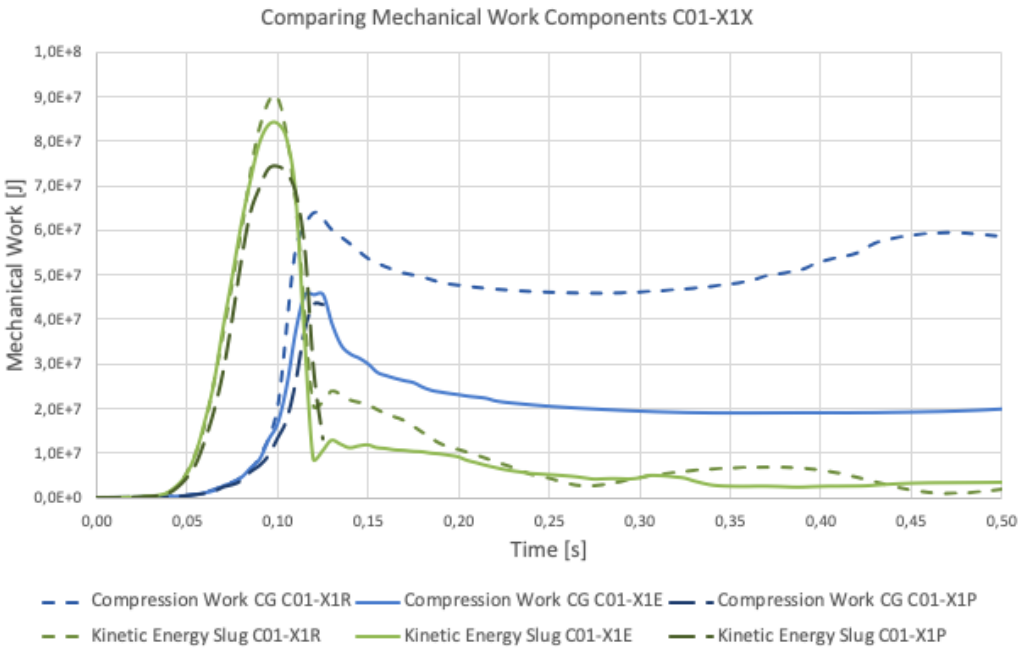

Figure 5.13: Kinetic energy and cover gas compression work over time for rigid and elastic cases C01-X1R, C01-X1E, and C01-X1P respectively.

the core region as figure 5.14 shows. It is the result of the initial shockwave after the vapor bubble formation through FCI. This explains the difference in kinetic slug energy between the linear elastic and the elasto-plastic case. Part of the mechanical work potential of the bubble goes in the deformation of the vessel wall.

The compression work on the cover gas is reduced for both cases with flexible structure. But among the linear elastic and the elasto-plastic case, the compression work remains constant. In all three cases, the slug impacts the vessel lid and reduces the cover gas volume to zero. Assuming the same cover-gas, and hence the same polytropic coefficient, one would expect to find the same amount of maximum compression work on the cover gas for all three cases. The reason we do not see this is the limited time resolution of the SIMMER post-processing file. Figure 5.15 illustrates the issue. The sudden pressure drop to zero is a consequence of the cover-gas region not being defined at the time of slug impact.

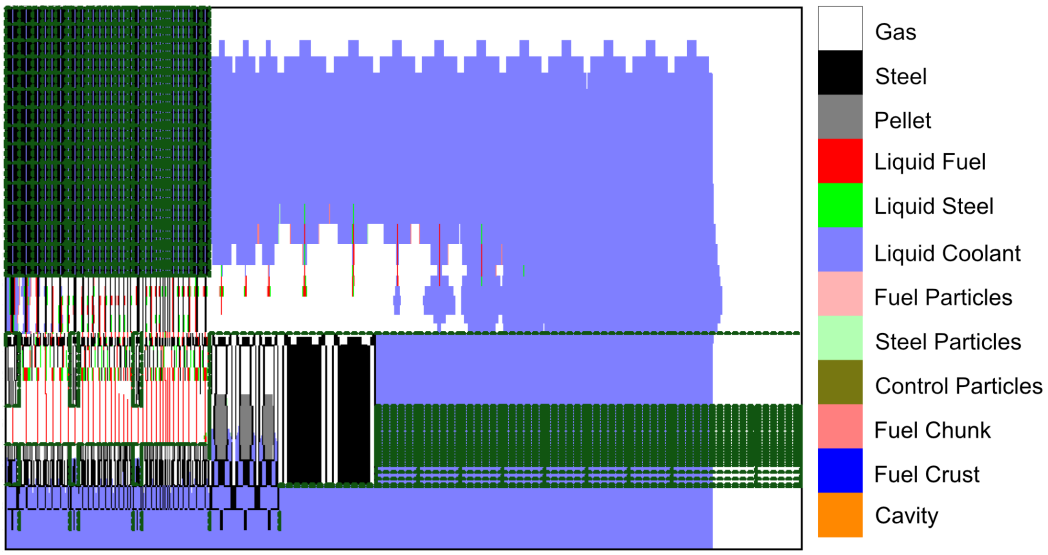

Figure 5.14: Plastic deformation of the vessel wall above the core region at t=0.085s during expansion phase of case C01-X1P as represented in SIMMER.

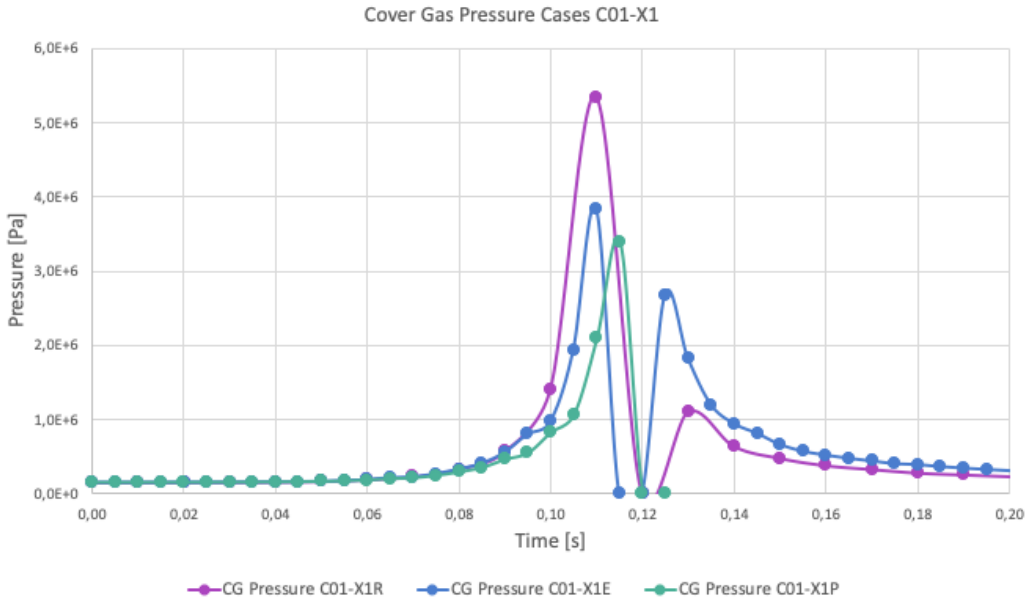

Figure 5.15: Cover gas pressure for the rigid, linear elastic and elasto-plastic cases C01-X1R, C01-X1E, and C01-X1P respectively. Pressure drop to zero where CG region undefined.

The goal of this chapter was to demonstrate the applicability of the new, coupled SIMMER code to expansion phase problems as they occur in a production environment. With the exception of case C01-X1P, all use cases completed within 12 to 24 hours on a desktop machine.

Case C01-X1P aborted, as large plastic deformation caused a failure of the structural code. The last recorded equivalent plastic strains were in the order of 1. Such a severe deformation would challenge the integrity of the vessel in general. Arguably, a real vessel would rupture prior to this point.

Overall, the coupled code performs as expected. The structural response of the vessel wall reduces the amount of combined mechanical work from slug kinetic energy and cover-gas compression that challenges the vessel integrity at impact. The medium intensity case with 6000K initial temperature of the molten fuel pool is an exception. Here, the mechanical work release increased with the flexible structure.

6 Conclusion

The goal of this work was to investigate the feasibility of introducing fluid-structure interaction to the existing severe accident code SIMMER III. During hypothetical severe accidents in nuclear reactors, the rate of energy production, fluid transients, and the structural response are all linked. A possibility to consider all three effects simultaneously in an adequate manner was unavailable until now.

I devised and implemented a method to represent continuous radial wall movement in the existing SIMMER III code base. The implementation does not compromise the fundamental equations of SIMMER and relies on utilizing the existing Volume Of Fluid formulation. We now have the possibility to represent radially moving boundaries in SIMMER's fluid dynamics formulation that do not conform to the structured mesh. Adequate representation of moving boundaries is a fundamental part of a FSI model. The method can be extended to represent axial boundary movement. At high speeds, the movement of the immersed boundary can cause spurious pressure oscillations in the boundary cell.

A newly developed, in-house FEM code now can calculate the structural response at every time-step. The code can also be used for standalone structural analysis and runs in parallel. It offers a great selection of numerical solvers and preconditionners through use of the PETSc[BAA+16] library. The user can change solver options through runtime options.

The code offers the possibility to conduct linear elastic, large displacement elastic and small strain elasto-plastic analysis. For the elastoplastic material model, it relies on multi-linear isotropic hardening. Three-dimensional as well as two-dimensional formulations are available. The available 2D-models are plane stress, plane strain, and axisymmetric formulations. The user can conduct static, quasi-static and dynamic analysis.

Since the entire code-base is accessible, future development is easily possible. Contributors can extend the structural code to improve models and performance or extend its functionality. The accessibility to the source code also allows to retrace numerical instabilities and implement remedies. I verified the FEM code by comparing the results of numerical analysis to analytical solutions in section 4.1.

The coupling between SIMMER's fluid dynamics model on one side and the structural code on the other side works by exchanging information of the pressure field in one direction and the current location of the wetted boundary in the other direction. For each timestep, the coupled code computes the solution in each domain exactly once which results in a sequential, or loose coupling of the codes. Tight coupling, while more stable, would increase computation time significantly and I deemed it impractical.

Application of the coupled code to a validation case as presented in section 4.2 not only proved the feasibility of introducing FSI to SIMMER. It also proved the adequacy of the chosen models. The extended code predicted pressure transients and vessel deformations in a satisfactory manner compared to the experimental data.

In section 5, I applied the newly developed extended SIMMER code to a relevant example of a severe accident scenario in the prototype fast neutron reactor Monju.

The new code applies sophisticated models for rate of energy release, fluid transients and structural response simultaneously. It accounts for interaction between all three important aspects of a HCDA a during run-time. I considered three cases with differing severity of a CDA. The code handles all three cases well. In addition to that, the results suggest that the structural response does indeed have an impact on the peak mechanical work exerted on the vessel wall during slug impact.

In conclusion, I demonstrate the feasibility of extending SIMMER by a FSI model. The newly developed coupled code is capable of considering all three important aspects of a HCDA (energy-, fluid- and structural dynamics) simultaneously. Chapter 5 illustrates the importance of a coupled analysis and underlines the usefulness of the new code.

While this presents a promising step, future improvements and further applications of the coupled code are thinkable. The following section 6.1 gives a quick overview of potential future work.

6.1 Outlook

The extended SIMMER code allows to account for fluid-structure interaction during the evolution of a HCDA. This is an important step towards more precise predictions of hypothetical severe accident evolution in fast neutron metal cooled reactors. While first results are promising, I recommend further investigations to better understand the capabilities and limits of the new code. The following section will mention some topics that seem worthy of a subsequent study. I will also propose a list of conclusive improvements and subjects for further development efforts. The section ends with a short list of possible further applications for the extended SIMMER code.

6.1.1 Conducting Benchmark Analysis

To analyze the structural response during a HCDA, the workflow until now was to determine the energy release rate with SIMMER. And to then conduct a FSI analysis with dedicated codes like EUROPLEXUS [CHVD79] [BCHL89] [LSB85] , modeling the energy source term through a polytropic gas expansion. Dedicated FSI codes are very capable in their specialty, generally providing multiple sophisticated material models and precise boundary representations of the wetted surfaces in the fluid domain. But they do lack advanced models for energy release and neglect the interaction between release rate and fluid state.

I propose a benchmark study, comparing results from EUROPLEXUS and the extended SIMMER code for an array of sample problems. This will help to identify the limitations and capabilities of both codes. The benchmark will show how much of a difference the interaction between energy release rate and fluid transient makes. It will also help future decisions on what code to rely on for a given problem. Or to identify future development efforts.

A benchmark study will help to classify the newly developed code among alternative approaches and serve as additional validation.

6.1.2 Recommended Improvements

The newly extended, coupled SIMMER code performed well regarding a selection of sample problems. On the other hand, some restriction and limits are evident. This section gives a short overview for recommended improvements to make the code even more useful. They mainly concern the refinement of the structural model, better representation of the immersed boundary in the fluid domain and performance increases.

Implementation of Axial Wall Movement

Despite good results in the verification and validation cases, one of the most evident shortcomings of the coupled code is, that the current immersed boundary model neglects axial wall displacement. There is a straight forward approach that seems easily feasible and provided reasonably good results in first tests.

I conducted a preliminary test displacing the bottom of a cylinder in axial direction following a sine movement. The liquid in the cylinder behaved as expected, filling the voided space in a downward movement and rising upwards with the leading edge of the bottom as well.

Implementing axial wall movement appears to be a manageable task when using the same approach as for radial wall movement, swapping the no flow area material of the right can wall for that of the pin. Information on axial displacement is also readily available. A representation of axial wall movement would allow to represent the reactor vessel as a whole and improve the accuracy of the coupled analysis without increasing analysis time on the structural side.

Improved Material Model

The current, multi-linear, isotropic and rate-independent hardening model allows a quick analysis of the reactor vessel's elasto-plastic behavior during a vapor explosion of coolant slug impact. The model is comparably stable and avoids additional Gauss point iterations to determine the current material state.

But it also requires that the user chose adequate hardening parameters prior to the analysis. They must reflect the expected range of strain rate and temperature. Also, the framework implies that a multi-linear hardening model can represent the actual material behavior reasonably well.

Sophisticated material models are readily available through open source libraries like DAMASK [RDS+19] . While those models increase the numerical effort required, they improve the quality of the structural results. Especially if the range of strain rate and material temperature are unknown prior to the analysis. The required development effort is manageable.

Including a refined material model could improve the accuracy of the structural analysis at the cost of additional Gauss-point iterations.

6.1.3 Further Applications

Application to Sloshing Phenomenon

After the initial thermal decomposition of the core region in a nuclear reactor, a molten pool region forms containing liquid fuel and cladding material. Depending on composition and movement of this corium pool, re-criticalities can occur [TB84]. An inward movement of the liquid corium concentrates fissile material in the center and leads to the release of nuclear energy through fission. This energy release locally evaporates the corium, creating a high pressure vapor cushion that disperses the corium outwards until it eventually hits the vessel wall. The wall stops the outward movement and reverses the flow which again moves inward to create a critical configuration. This phenomenon, depicted in figure 6.1 is known as *sloshing* [FF09] [DGH82].

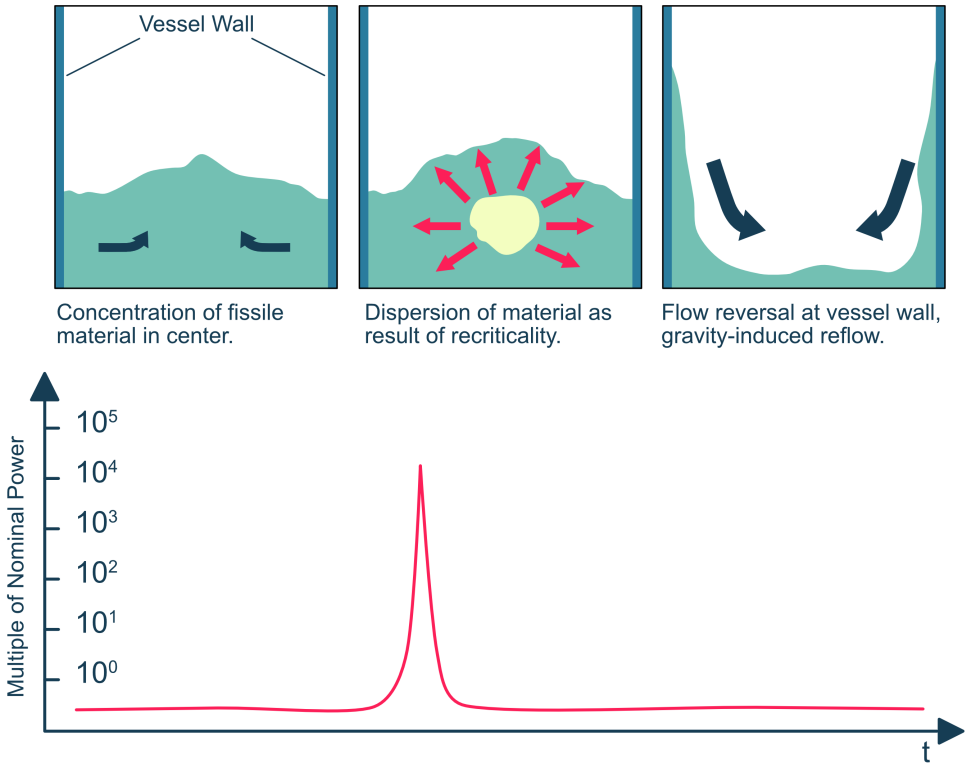

Figure 6.1: Movement of liquid fissile material can lead to a critical configuration that produces a highly energetic gas bubble, dispersing the corium. Flow reversal at the vessel walls can lead to a recurring and self-amplifying phenomenon known as sloshing.

The flow reversal of the high density liquid corium at the vessel wall implies an interaction between fluid and structure. Especially when the vessel wall is thin, the impact of the high density liquid will cause a deflection. Just as during the expansion phase, fluid transient, rate of energy production and structural response all interact during the sloshing phenomenon. The coupled code could help to more accurately model the sloshing phenomenon. First, by accounting

for wall deflection and changes in vessel geometry. Second, by introducing an external excitation to the system through the vessel structure.

Investigation of Seismic Excitation

Seismic activities in the vicinity of a nuclear reactor are a potential danger to the safety of the plant. Especially in pool type reactors, the oscillations can induce a sloshing motion in the liquid. The resulting change in coolant flow can potentially lead to local overheating or a change in reactivity and initiate a CDA. Again, we have an interaction between fluid transients, rate of energy release, and structural response.

Bibliography

[ABMO84] Ray E. Alcouffe, Forrest W. Brinkley, Duane R. Marr, and R. Douglas O'Dell. User's Guide for TWODANT:A Code Package for Two-Dimensional,Diffusion-Accelerated, Neutral-ParticleTransport. Technical Report LA-10049-M, Los Alamos National Laboratory, Los Alamos, 1984.

[ADH+14] Kazumi Aoto, Philippe Dufour, Yang Hongyi, Jean Paul Glatz, Yeong-il Kim, Yury Ashurko, Robert Hill, and Nariaki Uto. A summary of sodium-cooled fast reactor development. *Progress in Nuclear Energy*, 77:247–265, nov 2014.

[Alc95] Ray E. Alcouffe. THREEDANT: A code to perform three-dimensional, neutral particle transport calculations. In *International Conference on Mathematics and Computations, Reactor Physics, and Environmental Analyses*, Los Alamos, 1995.

[AM80] C. Albertini and M. Montagnani. Dynamic uniaxial and biaxial stress-strain relationships for austenitic stainless steels. *Nuclear Engineering and Design*, 57(1):107–123, 1980.

[ANH02] Yutaka Abe, Hideki Nariai, and Yukihiro Hamada. The trigger mechanism of vapor explosion. *Journal of Nuclear Science and Technology*, 39(8):845–853, 2002.

[AS69] J. H. Argyris and D. W. Scharpf. Finite Elements in Time and Space. *The Aeronautical Journal*, 73(708):1041–1044, dec 1969.

[aT96] a.S. Tijsseling. Fluid-Structure Interaction in Liquid-Filled Pipe Systems: a Review. *Journal of Fluids and Structures*, 10(2):109–146, 1996.

[AWvJ08] Emmanuel B. Agamloh, Alan K. Wallace, and Annette von Jouanne. Application of fluid–structure interaction simulation of an ocean wave energy extraction device. *Renewable Energy*, 33(4):748–757, apr 2008.

[BAA+16] Satish Balay, Shrirang Abhyankar, Mark F. Adams, Jed Brown, Peter Brune, Kris Buschelman, Lisandro Dalcin, Victor Eijkhout, William D. Gropp, Dinesh Kaushik, Matthew G. Knepley, Lois Curfman McInnes, Karl Rupp, Barry F. Smith, Stefano Zampini, Hong Zhang, and Hong Zhang. PETSc Users Manual. Technical Report ANL-95/11 Rev 3.7, Argonne National Laboratory, 2016.

[Bat06] Klaus-Jürgen Bathe. *Finite element procedures. Second edition.* Watertown, MA, United States of America, 2006.

[BC96] F. Balard and B. Carluec. Evaluation of the LMFBR cover gas source term and synthesis of the associated R and D. In *TECHNICAL COMMITTEE MEETING ON EVALUATION OF RADIOACTIVE MATERIALS AND SODIUM FIRES IN FAST REACTORS*, O-ARAI ENGINEERING CENTER, 1996.

[BCHL89] H. Bung, F. Casadei, J. P. Halleux, and M. Lepareux. PLEXIS-3C: A Computer Code for Fast Dynamic Problems in Structures and Fluids. In *SMiRT 10 - Anaheim*, pages 85–90, Anaheim, California, USA, 1989. International Association for Structural Mechanics in Reactor Technology (IASMIRT).

[BF17] A J Brunett and T H Fanning. U . S . Sodium Fast Reactor Codes and Methods : Current Capabilities and Path Forward. In *2017 International Conference on Fast Reactors and Related Fuel Cycles: Next Generation Nuclear Systems for Sustainable Development FR17*, pages 1–12, Yekaterinburg, 2017.

[BHK+99] G. Buckel, E. Hesselschwerdt, Edgar Kiefhaber, S. Kleinheins, and W. Maschek. A new SIMMER-III Version with improved Neutronics Solution Aigorithms. Technical Report FZKA 6290, Forschungszentrum Karlsruhe GmbH, Karlsruhe, 1999.

[BHK+10] Y. Bazilevs, M.-C. Hsu, J. Kiendl, R. Wüchner, and K.-U. Bletzinger. 3D simulation of wind turbine rotors at full scale. Part II: Fluid–structure interaction modeling with composite blades. *International Journal For Numerical Methods In Fluids*, 2011(65):236–253, 2010.

[BHRB76] J E Boudreau, F H Harlow, W H Reed, and J F Barnes. A PROPOSAL FOR COMPUTER INVESTIGATION OF LMFBR CORE MELTDOWN ACCIDENTS. Technical Report 336, Los Alamos Scientific Laboratory, Los Alamos, 1976.

[BK76] T.B. Belytschko and J.M. Kennedy. A fluid-structure finite element method for the analysis of reactor safety problems. *Nuclear Engineering and Design*, 38(1):71–81, jul 1976.

[BKRG98] Manoj K. Bhardwaj, Rakesh K. Kapania, Eric Reichenbach, and Guru P. Guruswamy. Computational fluid dynamics/computational structural dynamics interaction methodology for aircraft wings. *AIAA Journal*, 36(12):2179–2186, 1998.

[BL90] W R Bohl and L B Luck. SIMMER-II: A Computer Program for LMFBR Disrupted Core Analysis. Technical report, Los Alamos National Laboratory, Los Alamos, 1990.

[BLP+79] J.P. Breton, A. Lapicore, A. Porrachia, M. Natta, M. Amblard, and G. Berthoud. Expansion of a vapor bubble and aerosols transfer. In *International Meeting on Fast Reactor Safety Technology*, Seatle, USA, 1979.

[Bre82] J. P. (DSN / Cadarace) Breton. SOME CEA STUDIES RELATED TO CORE EXPANSION. THE CARAVELLE EXPERIMENTS AND THE IRIS CODE. Technical report, CEA, Ispra (Italy), 1982.

[Bri01] Charles R. Brinkman. Elevated-Temperature Mechanical Properties of an Advanced-Type 316 Stainless Steel. *Journal of Pressure Vessel Technology*, 123(January 2000):75, 2001.

[BRW75] Klaus-Jürgen Bathe, Ekkehard Ramm, and Edward L. Wilson. Finite Element Formulations For Large Deformation Dynamic Analysis. *International Journal for Numerical Methods in Engineering*, 9:353–386, 1975.

[BST06] A. Bergant, A.R. Simpson, and A.S. Tijsseling. Water hammer with column separation: A historical review. *Journal of Fluids and Structures*, 22(2):135–171, feb 2006.

[Buc74] D J Buchanan. A model for fuel-coolant interactions. *Journal of Physics D: Applied Physics*, 7:1441–1457, 1974.

[CCR10] P. (Indira Gandhi Centre for Atomic Research) Chellapandi, S. C. (Indira Gandhi Centre for Atomic Research) Chetal, and Baldev (Indira Gandhi Centre for Atomic Research) Raj. STRUCTURAL INTEGRITY ASSESSMENT OF REACTOR ASSEMBLY COMPONENTS OF A POOL-TYPE SODIUM FAST REACTOR IN A CORE DISRUPTIVE ACCIDENT — I : DEVELOPMENT OF COMPUTER CODE AND VALIDATIONS. *Nuclear Technology*, 172:1–15, 2010.

[CDM07] Fehmi Cirak, Ralf Deiterding, and Sean P. Mauch. Large-scale fluid-structure interaction simulation of viscoplastic and fracturing thin-shells subjected to shocks and detonations. *Computers and Structures*, 85(2007):1049–1065, 2007.

[CHS86] D. K. Clarke, H. A. Hassan, and M. D. Salas. Euler calculations for multielement airfoils using Cartesian grids. *AIAA Journal*, 24(3):353–358, 1986.

[CHVD79] C. Chavant, A. Hoffmann, P. Verpeaux, and J. Dubois. Plexus: A General Computer Code For Explicit Lagrangian Computation. In *SMiRT 5 Vols. B - Thermal and Fluid/Structure Dynamics Analysis, B2 - Computational Methods II*, Berlin, Germany, 1979.

[Clo90] Ray W. Clough. Original formulation of the finite element method. *Finite Elements in Analysis and Design*, 7(2):89–101, nov 1990.

[CMR02] T. Cadiou, Werner Maschek, and Andrei Rineiski. SIMMER-III : Applications to reactor accident analysis. In *Proc. Joint IAEA/NEA Technical Meeting*, number November, 2002.

[CRD+11] Paolo Crosetto, Philippe Reymond, Simone Deparis, Dimitrios Kontaxakis, Nikolaos Stergiopulos, and Alfio Quarteroni. Fluid–structure interaction simulation of aortic blood flow. *Computers & Fluids*, 43(1):46–57, apr 2011.

[CSZ+01] G Chambers, H Sandusky, F Zerilli, K Rye, R Tussing, and Jerry Forbes. Pressure measurements on a deforming surface in response to an underwater explosion in a water-filled aluminum tube. *Shock and Vibration*, 8(1):1–7, 2001.

[DB06] M. R. Daymond and P. J. Bouchard. Elastoplastic deformation of 316 stainless steel under tensile loading at elevated temperatures. *Metallurgical and Materials Transactions A*, 37(6):1863–1873, 2006.

[DFSG76] J. Donea, P. Fasoli-Stella, and S. Giuliani. Finite element solution of transient fluid-structure problems in Lagrangian coordinates. In *International meeting on fast reactor safety and related physics*, pages 1427–1435, Chicago, Illinois, USA, 1976.

[DGH82] J. Donea, S. Giuliani, and J.P. Halleux. An arbitrary lagrangian-eulerian finite element method for transient dynamic fluid-structure interactions. *Computer Methods in Applied Mechanics and Engineering*, 33(1-3):689–723, 1982.

[DS96] John E. Dennis Jr and Robert B. Schnabel. *Numerical methods for unconstrained optimization and nonlinear equations.* Society for Industrial and Applied Mathematics, Philadelphia, USA, 1996.

[EBB+02] Silvano Erlicher, Luca Bonaventura, Oreste Bursi, Silvano Erlicher, Luca Bonaventura, Oreste Bursi, Università Trento, Via Mesiano, and Ingegneria Civile. The analysis of the Generalized-a method for non-linear dynamic problems. *Computational Mechanics*, 28(2):83–104, 2002.

[FBLD82] M. Falgayrettes, Y. Blanchet, J. Louvet, and C. Delli. Observation and analysis of expansion of an explosive bubble in a confined environment: the CARAVELLE 6 experiment. In *International topical meeting on LMFBR safety*, Lyon, France, 1982.

[FF09] Rosa Lo Frano and Giuseppe Forasassi. A Preliminary Evaluation of a Generation IV Liquid Metal Fast Reactor due to Sloshing and Thermal Stress. In *Proceedings of the ASME 2009 Pressure Vessels and Piping Division Conference*, pages 1–10, Prague, Czech Republic, 2009.

[FGG+15] Michael Flad, Fabrizio Gabrielli, Simone Gianfelici, Rui Li, Vladimir Kriventsev, Werner Maschek, Claudia Matzerath Boccaccini, Barbara Vezzoni, and Andrei Rineiski. Quantitative Evaluation of the thermal-to- mechanical energy conversion ratio during the ULOF post disassembly expansion phase (EP) of MONJU – SIMMER-III Calculations for PRD Evaluations. Technical Report JNES/ Del.PRD-EP-02, KIT-IKET, Karlsruhe, 2015.

[FH73] R. L. Fish and J. J. Holmes. Tensile properties of annealed type 316 stainless steel after EBR-II irradiation. *Journal of Nuclear Materials*, 46(2):113–120, 1973.

[FLSZ85] C. Fiche, J. Louvet, B. L. Smith, and A. Zucchini. Theoretical experimental study of flexible roof effects in an HCDA's simulation. In *Proc. 8th Int. Conf. on Structural Integrity In Reactor Technology*, pages 139–144, Brussels, Belgium, 1985.

[FP08] J.H. Ferziger and M. Peric. *Numerische Strömungsmechanik*. Springer-Verlag Berlin Heidelberg, Berlin, Heidelberg, 2008.

[Fri19] Hans-Jürgen Frieske. *Technische Mechanik – Statik*. Springer Vieweg, Wiesbaden, 2019.

[FRS+76] R. (Gesellschaft für Kernforschung m.b.H. Karlsruhe) Fröhlich, P. (Gesellschaft für Kernforschung m.b.H. Karlsruhe) Royl, P. (Gesellschaft für Kernforschung m.b.H. Karlsruhe) Schmuck, Bensberg/Köln) Düsing, R. (Interatom G.m.b.H., and Bensberg/Köln) Senglau, M. (Interatom G.m.b.H. Analyse Schwerer Hypothetischer Störfälle für den SNR-300 Mark 1A Reaktorkern. Technical Report KFK 2310, Kernforschungszentrum Karlsruhe, 1976.

[FV11] G.L. Fiorini and A. Vasile. European Commission – 7th Framework Programme. *Nuclear Engineering and Design*, 241(9):3461–3469, sep 2011.

[GFCK02] Frederic Gibou, Ronald P. Fedkiw, Li-Tien Cheng, and Myungjoo Kang. A Second-Order-Accurate Symmetric Discretization of the Poisson Equation on Irregular Domains. *Journal of Computational Physics*, 176(1):205–227, feb 2002.

[GHS93] D. Goldstein, R. Handler, and L. Sirovich. Modeling a No-Slip Flow Boundary with an External Force Field. *Journal of Computational Physics*, 105(2):354–366, apr 1993.

[GPD+03] Jean Paul Grouiller, Sylvie Pillon, Cyrille De Saint Jean, Frederic Varaine, Lydie Leyval, Guy Vambenepe, and Bertrand Carlier. Minor actinides transmutation scenario studies with PWRs, FRs and moderated targets. *Journal of Nuclear Materials*, 320:163–169, 2003.

[GPHJ99] R. Glowinski, T.-W. Pan, T.I. Hesla, and D.D. Joseph. A distributed Lagrange multiplier/fictitious domain method for particulate flows. *International Journal of Multiphase Flow*, 25(5):755–794, aug 1999.

[GPP94] R. Glowinski, T.-W. Pan, and J. Periaux. A fictitious domain method for Dirichlet problem and applications. *Computer Methods in Applied Mechanics and Engineering*, 111:283–303, 1994.

[GR09] Christophe Geuzaine and Jean François Remacle. Gmsh: A 3-D finite element mesh generator with built-in pre- and post-processing facilities. *International Journal for Numerical Methods in Engineering*, 79(11):1309–1331, 2009.

[GU06] Daniel Green and William G. Unruh. The failure of the Tacoma Bridge: A physical model. *American Journal of Physics*, 74(8):706, 2006.

[HaAC74] C.W. Hirt, a.a. Amsden, and J. L. Cook. An Arbitrary Lagrangian-Eulerian Computing Method for All Flow Speeds. *Journal of Compuational Physics*, 14:227–253, 1974.

[HHB08] Matthias Heil, Andrew L. Hazel, and Jonathan Boyle. Solvers for large-displacement fluid-structure interaction problems: Segregated versus monolithic approaches. *Computational Mechanics*, 43(1):91–101, 2008.

[HN81] C.W. Hirt and B.D. Nichols. Volume of Fluid (VOF) Method for the Dynamics of Free Boundaries*. *Journal of Computational Physics*, 39:201–225, 1981.

[HTIY85] Akio Hayashi, Tadao Takahashi, Akira Izumi, and Tsutomu Yanagisawa. Impact of Safety and Licensing Considerations on MONJU. In *Proceedings of the International Topical Meeting on Fast Reactor Safety*, pages 7–12, Knoxville, 1985.

[HWD04] Björn Hübner, Elmar Walhorn, and Dieter Dinkler. A monolithic approach to fluid–structure interaction using space–time finite elements. *Computer Methods in Applied Mechanics and Engineering*, 193(23-26):2087–2104, jun 2004.

[Iak07] S. Iakovlev. Submerged fluid-filled cylindrical shell subjected to a shock wave: Fluid–structure interaction effects. *Journal of Fluids and Structures*, 23(1):117–142, jan 2007.

[IATT92] Akira Inoue, Masanori Aritomi, Minoru Takahashi, and Yoshiharu Tomita. An Analytical Model on Vapor Explosion of a High Temperature Molten Metal Drop in Water Induced By a Pressure Pulse. *Chemical Engineering Communications*, 118(1):189–206, 1992.

[Int07] International Atomic Energy Agency. Fast Reactor Database 2006 Update. Technical Report IAEA-TECDOC-1531, IAEA, Vienna, 2007.

[KBT+96] Sa. Kondo, David J. Brear, Yoshiharu Tobita, K. Morita, Kenji Kamiyama, E. A. Fischer, Werner Maschek, C.-D. Munz, Michael Flad, S. Kleinheins, G. Arnecke, E. Hesselschwerdt, M. Göz, H. Jacobs, B. Stehle, T. Jeanne, P. Coste, D. Wilhelm, F. Boulanger, and S. Vandroux-Koenig. Phase 1 Code Assessmemt of Simmer III,

A Computer Program for LMFR Core Disruptive Accident Analysis. Technical Report PNC ZD0176 96-001, Power Reactor and Nuclear Fuel Development Corporation, Japan; Forschungszentrum Karlsruhe, Germany; Commissariat à l'Energie Atomique, France, 1996.

[Kim15] Nam-Ho Kim. *Introduction to Nonlinear Finite Element Analysis*. Springer New York Heidelberg Dodrecht London, New York, NY, 2015.

[KK04] Kenji Kamiyama and Satoru Kondo. SIMMER-III Structure Model. Technical Report JNC TN9400 2004–043, O-arai Engineering Center Japan Nuclear Cycle Development Institute, 2004.

[KKC01] Jungwoo Kim, Dongjoo Kim, and Haecheon Choi. An Immersed-Boundary Finite-Volume Method for Simulations of Flow in Complex Geometries. *Journal of Computational Physics*, 171(1):132–150, jul 2001.

[KTMS92] S. Kondo, Y. Tobita, K. Morita, and N. Shirakawa. SIMMER-III: an advanced computer program for LMFBR severe accident analysis. In *ANP'92: international conference on design and safety of advanced nuclear power plants*, Tokyo, Japan, 1992.

[LAB+14] A. Lázaro, L. Ammirabile, G. Bandini, G. Darmet, S. Massara, Ph. Dufour, A. Tosello, E. Gallego, G. Jimenez, K. Mikityuk, M. Schikorr, E. Bubelis, A. Ponomarev, R. Kruessmann, and M. Stempniewicz. Code assessment and modelling for Design Basis Accident Analysis of the European sodium fast reactor design. Part I: System description, modelling and benchmarking. *Nuclear Engineering and Design*, 266:1–16, jan 2014.

[LS04] G S Langdon and G K Schleyer. Unusual strain rate sensitive behaviour of AISI 316L austenitic stainless steel. *Journal of Strain Analysis for Engineering Design*, 39(1):71–86, 2004.

[LSB85] M. Lepareux, B. Schwab, and H. Bung. PLEXUS - a general computer program for the fast dynamic analysis - the case of pipe-circuits. In *Transactions of the 8. international conference on structural mechanics in reactor technology. Vol. F1 and F2*, pages 39–46, Brussels, 1985.

[LZL05] Chuang Liu, Xiong Zhang, and Ming-Wan Lu. Fluid-structure interaction analysis of a hypothetical core disruptive accident in LMFBRs. *Nuclear Engineering and Design*, 235(6):701–712, mar 2005.

[MF98] K. Morita and E.A. Fischer. Thermodynamic properties and equations of state for fast reactor safety analysis: Part I: Analytic equation-of-state model. *Nuclear Engineering and Design*, 183(3):177–191, jul 1998.

[MHvBdB04] C. Michler, S.J. Hulshoff, E.H. van Brummelen, and R. de Borst. A monolithic approach to fluid–structure interaction. *Computers & Fluids*, 33(5-6):839–848, jun 2004.

[MI05] Rajat Mittal and Gianluca Iaccarino. Immersed Boundary Methods. *Annual Review of Fluid Mechanics*, 37(1):239–261, jan 2005.

[MKTB99] K. Morita, Sa Kondo, Y. Tobita, and D. J. Brear. SIMMER-III applications to fuel-coolant interactions. *Nuclear Engineering and Design*, 189(1):337–357, 1999.

[MMLM03] Magnus Mori, Werner Maschek, Eckart Laurien, and Koji Morita. Monte-Carlo/Simmer-III Reactivity Coefficients Calculations for the SuperCritical Water Fast Reactor. In *Proc. of the ANS/ENS Topical Meeting GLOBAL*, New Orleans, 2003.

[MÖ18] Marin Marin and Andreas Öchsner. *Essentials of Partial Differential Equations*. Springer International Publishing, Cham, 2018.

[MRK+01] K Morita, A Rineiski, E Kiefhaber, W Maschek, G Rimpault, P Coste, S Pigny, Y Tobita, and S Fujita. Mechanistic SIMMER-III Analyses of Severe Transients in Accelerator Driven Systems (ADS). In *Proceedings of the Ninth International Conference on Nuclear Engineering (ICONE-9)*, Nice, France, 2001. Forschungszentrum Karlsruhe.

[MRS+03] Werner Maschek, Andrei Rineiski, Tohru Suzuki, X. Chen, Mg. Mori, S. Wang, Y Tobita, Sa. Kondo, H. Yamano, S. Fujita, T. Cadiou, and P. Coste. The SIMMER-III and SIMMER-IV Code Family: 2-D and 3-D Mechanistic Simulation Tools for Reactor Transients and Accidents. In *Technical meeting on use and development of coupled computer codes for the analysis of accidents at nuclear power plants*, Vienna, Austria, 2003. Forschungszentrum Karlsruhe.

[MRSW05] W Maschek, A Rineiski, T Suzuki, and S Wang. SIMMER-III and SIMMER-IV safety code development for reactors with transmutation capability. In *International topical meeting on mathematics and computation, supercomputing, reactor physics and nuclear and biological applications*, pages 1–14, Avignon, France, 2005.

[MS02] Hermann G. Matthies and Jan Steindorf. Partitioned but strongly coupled iteration schemes for nonlinear fluid–structure interaction. *Computers & Structures*, 80(27-30):1991–1999, nov 2002.

[MTKF99] K Morita, Y. Tobita, Sa. Kondo, and E.A. Fischer. SIMMER-III analytic thermophysical property model. Technical Report JNC TN9400 2000-004, Japan Nuclear Cycle Development Institute, 1999.

[NI18] Nuclear Energy Agency and International Atomic Energy Agency. Uranium 2018: Resources , Production and Demand. Technical Report 7413, Organisation for Economic Co-operation and Development (OECD), 2018.

[NKI+04a] Toshio Nakamura, Hitoshi Kaguchi, Iwao Ikarimoto, Yoshio Kamishima, Kazuya Koyama, Shigenobu Kubo, and Shoji Kotake. Evaluation method for structural integrity assessment in core disruptive accident of fast reactor. *Nuclear Engineering and Design*, 227(1):97–123, 2004.

[NKI+04b] Toshio Nakamura, Hitoshi Kaguchi, Iwao Ikarimoto, Yoshio Kamishima, Kazuya Koyama, Shigenobu Kubo, and Shoji Kotake. Evaluation method for structural integrity assessment in core disruptive accident of fast reactor. *Nuclear Engineering and Design*, 227(1):97–123, jan 2004.

[OAKKI98] N Ohno, M Abdel-Karim, M Kobayashi, and T Igari. Ratchetting characteristics of 316FR steel at high temperature, part I: Strain-controlled ratchetting experiments and simulations. *International Journal of Plasticity*, 14(4–5):355–372, 1998.

[OTH04] William L Oberkampf, Timothy G Trucano, and Charles Hirsch. Verification, validation, and predictive capability in computational engineering and physics. *Applied Mechanics Reviews*, 57(5):345, 2004.

[Paï83] M.P. Païdoussis. A review of flow-induced vibrations in reactors and reactor components. *Nuclear Engineering and Design*, 74(1):31–60, jan 1983.

[Pes72] Charles S Peskin. Flow patterns around heart valves: A numerical method. *Journal of Computational Physics*, 10(2):252–271, oct 1972.

[Pes77] Charles S Peskin. Numerical analysis of blood flow in the heart. *Journal of Computational Physics*, 25(3):220–252, nov 1977.

[Pes03] Charles S. Peskin. The immersed boundary method. *Acta Numerica*, 11(January 2002):479–517, jul 2003.

[PFO01] K.C. Park, Carlos A. Felippa, and Roger Ohayon. Partitioned formulation of internal fluid–structure interaction problems by localized Lagrange multipliers. *Computer Methods in Applied Mechanics and Engineering*, 190(24-25):2989–3007, mar 2001.

[RDS+19] F. Roters, M. Diehl, P. Shanthraj, P. Eisenlohr, C. Reuber, S.L. Wong, T. Maiti, A. Ebrahimi, T. Hochrainer, H.-O. Fabritius, S. Nikolov, M. Friák, N. Fujita, N. Grilli, K.G.F. Janssens, N. Jia, P.J.J. Kok, D. Ma, F. Meier, E. Werner, M. Stricker, D. Weygand, and D. Raabe. DAMASK – The Düsseldorf Advanced Material Simulation Kit for modeling multi-physics crystal plasticity, thermal, and damage phenomena from the single crystal up to the component scale. *Computational Materials Science*, 158:420–478, feb 2019.

[RLC03] M. F. Robbe, M. Lepareux, and Y. Cariou. Numerical interpretation of the MARA 8 experiment simulating a hypothetical core disruptive accident. *Nuclear Engineering and Design*, 220(2):119–158, 2003.

[SAH90] Hetnmat H. Safwat, Asif H. Arastu, and Syed M. Husaini. Systematic methodology for diagnosis of water hammer in LWR power plants. *Nuclear Engineering and Design*, 122(1-3):365–376, sep 1990.

[Sal05] M. Salvatores. Nuclear fuel cycle strategies including Partitioning and Transmutation. *Nuclear Engineering and Design*, 235(7):805–816, mar 2005.

[SB96] E.M. Saiki and S. Biringen. Numerical Simulation of a Cylinder in Uniform Flow: Application of a Virtual Boundary Method. *Journal of Computational Physics*, 123(2):450–465, feb 1996.

[SC08] Linwei Shen and Eng-Soon Chan. Numerical simulation of fluid–structure interaction using a combined volume of fluid and immersed boundary method. *Ocean Engineering*, 35(8-9):939–952, jun 2008.

[SGM14] I M Smith, D V Griffiths, and Lee Margetts. *Programming the Finite Element Method*. Wiley, Chichester, West Sussex, United Kingdom, 5 edition, 2014.

[SKK02] Kirk Schloegel, George Karypis, and Vipin Kumar. Parallel static and dynamic multi-constraint graph partitioning. *Concurrency Computation Practice and Experience*, 14(3):219–240, 2002.

[SRR+13] Manuel Saez, Jean-Charles Robin, Bernard Riou, Alexandre Villedieu, Dominique Deprest, and Gérard Prele. Status of ASTRID nuclear island pre-conceptual design. *IAEA Conference FR13*, (March):4–7, 2013.

[SS86] Youcef Saad and Martin H. Schultz. GMRES: A Generalized Minimal Residual Algorithm for Solving Nonsymmetric Linear Systems. *SIAM Journal on Scientific and Statistical Computing*, 7(3):856–869, 1986.

[ST85] J. C. Simo and R. L. Taylor. Consistent Tangent Operators for Rate-Independent Elastoplasticity. *Computer methods in applied mechanics and engineering*, 48:101–118, 1985.

[SYI85] Maski Saito, Shinji Yoshie, and Makoto Ishikawa. Structural Response of 1/33-, 1/20- and 1/15-Scale Models of the MONJU Reactor Vessel to a Simulated HCDA. In *Proceedings of the International Topical Meeting on Fast Reactor Safety*, pages 509–519, Knoxville, 1985.

[TB84] T. G. Theofanous and C.R. Bell. An Assessment of CRBR Core Disruptive Accident Energetics. Technical Report NUREG/CR-3 224, LA-9716-MS, Los Alamos National Laboratory, Los Alamos, New Mexico, 1984.

[Tij07] A.S. Tijsseling. Water hammer with fluid–structure interaction in thick-walled pipes. *Computers & Structures*, 85(11-14):844–851, jun 2007.

[TKY+05] Y. Tobita, Sa. Kondo, H. Yamano, K. Morita, W. Maschek, P. Coste, and T. Cadiou. The Development of SIMMER-III, An Advanced Computer Program for LMFR Safety Analysis, and Its Application to Sodium Experiments. *Nuclear Technology*, 153(3):245–255, 2005.

[TL90] A.S. Tijsseling and C.S.W. Lavooij. Waterhammer with fluid-structure interaction. *Applied Scientific Research*, (1):273–285, 1990.

[Tob04] Yoshiharu Tobita. Momentum Exchange Function Model in SIMMER-III. Technical Report JNC TN9410 2004, O-arai Engineering Center, Japan Nuclear Cycle Development Institute, 2004.

[TPWW10] Am Tentner, E Parma, T Wei, and R Wigeland. Severe accident approach-final report. Evaluation of design measures for severe accident prevention and consequence mitigation. Technical Report ANL-GENIV-128, Argonne National Laboratory, 2010.

[UMRK01] H.S. Udaykumar, R. Mittal, P. Rampunggoon, and A. Khanna. A Sharp Interface Cartesian Grid Method for Simulating Flows with Complex Moving Boundaries. *Journal of Computational Physics*, 174(1):345–380, nov 2001.

[UMS99] H.S Udaykumar, R Mittal, and Wei Shyy. Computation of Solid–Liquid Phase Fronts in the Sharp Interface Limit on Fixed Grids. *Journal of Computational Physics*, 153(2):535–574, aug 1999.

[UOK+07] Sadao Uchikawa, Tsutomu Okubo, Teruhiko Kugo, Hiroshi Akie, Yoshihiro Nakano, Akira Ohunki, and Takamichi Iwamura. Conceptual Design of Innovative Water Reactor for Flexible Fuel Cycle (FLWR) and its Recycle Characteristics Conceptual Design of Innovative Water Reactor. *Journal of Nuclear Science and Technology*, 44(3):277–285, 2007.

[Vul14] Vincenzo Vullo. *Circular Cylinders and Pressure Vessels*, volume 3. Springer Cham Heidelberg New York Dordrecht London, 2014.

[WKHD05] E. Walhorn, A. Kölke, B. Hübner, and D. Dinkler. Fluid–structure coupling within a monolithic model involving free surface flows. *Computers & Structures*, 83(25-26):2100–2111, sep 2005.

[WL00] Andrew B Wardlaw and J Alan Luton. Fluid-structure interaction mechanisms for close-in explosions. *Shock and Vibrations*, pages 265–275, 2000.

[Wol82] L. Wolf. Experimental results of coupled fluid-structure interactions during blow-down of the HDR-vessel and comparisons with pre- and post-test predictions. *Nuclear Engineering and Design*, 70:269–308, 1982.

[WP02] W. Wagner and A. Pruß. The IAPWS formulation 1995 for the thermodynamic properties of ordinary water substance for general and scientific use. *Journal of Physical and Chemical Reference Data*, 31(2):387–535, 2002.

[WRM06] Shisheng Wang, Andrei Rineiski, and Werner Maschek. Molten salt related extensions of the SIMMER-III code and its application for a burner reactor. *Nuclear Engineering and Design*, 236(14-16):1580–1588, aug 2006.

[YFT+03] H. Yamano, S. Fujita, Yoshiharu Tobita, Kenji Kamiyama, Satoru Kondo, Koji Morita, E. A. Fischer, David J. Brear, N. Shirakawa, X. Cao, M. Sugaya, M. Mizuno, S. Hosono, T. Kondo, Werner Maschek, Edgar Kiefhaber, G. Buckel, Andrei Rineiski, Michael Flad, Tohru Suzuki, P. Coste, S. Pigny, J. Louvet, and T. Cadiou. SIMMER-III : A Computer Program for LMFR Core Disruptive Accident Analysis - Version 3.A Model Summary and Program Description -. Technical Report JNC TN9400 2003-071, O-arai Engineering Center Japan Nuclear Cycle Development Institute, 2003.

[YT11] Hidemasa YAMANO and Yoshiharu TOBITA. Experimental Analyses by SIMMER-III on Debris-Bed Coolability and Metallic Fuel Freezing Behavior. *Journal of Power and Energy Systems*, 5(1):2–18, 2011.

[YTF09] Hidemasa Yamano, Yoshiharu Tobita, and Satoshi Fujita. A three-dimensional neutronics-thermohydraulics simulation of core disruptive accident in sodium-cooled fast reactor. *Nuclear Engineering and Design*, 239(9):1673–1681, sep 2009.

[ZW85] W. R. Zeuch and C. Y. Wang. A Quantitative Analysis of the Effect of Complex Internals on LMFBR Containment During Energetic Accidents. In *Proceedings of the International Topical Meeting on Fast Reactor Safety*, pages 499–506, 1985.

[ZZLG09] Feng Zhu, Longmao Zhao, Guoxing Lu, and Emad Gad. A numerical simulation of the blast impact of square metallic sandwich panels. *International Journal of Impact Engineering*, 36(5):687–699, may 2009.